PACIFIC EARTHQUAKE ENGINEERING RESEARCH CENTER

The Integration of Experimental and Simulation Data in the Study of Reinforced Concrete Bridge Systems Including Soil-Foundation-Structure Interaction

Matthew Dryden

and

Gregory L. Fenves

University of California, Berkeley

PEER 2009/03

NOVEMBER 2009

The Integration of Experimental and Simulation Data in the Study of Reinforced Concrete Bridge Systems Including Soil-Foundation-Structure Interaction

Matthew Dryden
Department of Civil and Environmental Engineering
University of California, Berkeley

Gregory L. Fenves
Department of Civil and Environmental Engineering
University of California, Berkeley

PEER Report 2009/03
Pacific Earthquake Engineering Research Center
College of Engineering
University of California, Berkeley
November 2009

ABSTRACT

The seismic response of reinforced concrete bridges must include consideration of the whole system including soil-foundation-structure interaction (SFSI). Simulation models validated against the results of experimental tests are required to provide an accurate prediction of the bridge system response. Performance-based engineering necessitates large-scale parameter studies of these simulation models to quantify the demand for varying levels of seismic hazard. The goal of this research is to characterize the SFSI effects for a range of hazard levels by using calibrated models from the experimental tests.

Two projects administered by the Network for Earthquake Engineering Simulation (NEES) have facilitated the study of this system effect through the collaboration of researchers within the earthquake engineering community. Shaking table tests of both a two-span and a four-span bridge at 1/4-scale were conducted at the University of Nevada, Reno. Nonlinear dynamic analyses of three-dimensional finite element models performed using OpenSees were evaluated based on the experimental test results. For the two-span bridge, the simulation model matches well both the global and local response until the onset of failure. The highly nonlinear pounding at the abutments and complicated test protocol of the four-span bridge produces less agreement in the simulation results.

A simulation model for the prototype bridge system incorporates the influence of the abutments, drilled shaft foundations, and site response effects. The cyclic response of the soil at the abutments is calibrated using results from full-scale tests. P-y, t-z, and q-z springs model the inertial interaction between the soil and pile foundations. A total of 1280 site response analyses are computed at four locations along the bridge for two soil profiles using SHAKE to obtain the free-field motions at the location of each soil spring.

Large-scale parameter studies of four prototype bridge models with and without the SFSI effect were conducted in parallel on a supercomputer using the multiple-interpreter capability of OpenSees. The response is determined for a suite of 80 ground motions of varying magnitude and distance from the fault. Linear regressions of the simulation results produce demand models that elucidate the effect of SFSI for both the global and local response. The demand models demonstrate that the SFSI effect is significant for the prototype bridge system and should be considered.

ACKNOWLEDGMENTS

The research described herein was supported by the National Science Foundation through Grant Nos. CMMI-0324343 and CMMI-0420347 and through a National Science Foundation Graduate Research Fellowship. The support of these funds is gratefully acknowledged. This work was supported in part by the Earthquake Engineering Research Centers Program of the National Science Foundation under award number EEC-9701568 through the Pacific Earthquake Engineering Research Center (PEER). Any opinions, findings, and conclusions or recommendations expressed in this material are those of the authors and do not necessarily reflect those of the National Science Foundation.

This research would not have been possible without Dr. Frank McKenna, the primary architect of OpenSees. Prof. Michael Scott implemented the algorithms for the beam-column elements used in the simulation of reinforced concrete columns. Dr. Silvia Mazzoni provided thorough documentation of the many objects within OpenSees. Many thanks are due to them and all the additional contributors to OpenSees.

The authors thank Dr. Nathan Johnson at the University of Nevada, Reno, and Dr. Tyler Ranf at the University of Washington for their work on the shake table tests of the two-span bridge. Robby Nelson at the University of Nevada, Reno, provided information about the experimental tests of the four-span bridge. Patrick Wilson at the University of California, San Diego, performed the full-scale experimental tests of bridge abutments. Prof. Sharon Wood at the University of Texas, Austin, served as the principal investigator for the NEES Demo Project, and Prof. Saiid Saiidi at the University of Nevada, Reno, served as the principal investigator for the subsequent NEESR project.

CONTENTS

LIST OF FIGURES

LIST OF TABLES

1 Introduction

To determine accurately the deformations and forces in reinforced concrete bridges during earthquakes, it is necessary to account for the whole system response, including the structure, foundation, and soil. Such an accurate determination of the bridge response is necessary to make design decisions within the performance-based engineering framework. Although numerous studies (Fenves and Ellery, 1998; Gazetas and Mylonakis, 1998; Goel and Chopra, 1997; Hutchinson et al., 2004; Jeremic et al., 2004; McCallen and Romstad, 1994; Zhang and Makris, 2001) have utilized computational simulations to study this system response, experimental research (Hachem et al., 2003; Lehman and Moehle, 1998; Mazzoni et al., 2004) has focused on component tests. Such simplification has been necessary due to the limitations of testing facilities but neglects the fact that the bridge behaves as a system. Among the system effects that influence the seismic response of bridges are soil-foundation-structure interaction (SFSI) at the column foundations and abutments and dynamic effects associated with bridge bents of differing column heights.

The performance-based engineering framework requires seismic demands for reinforced concrete bridges to be computed through the use of nonlinear dynamic analyses of finite element models. Robust simulation models that are calibrated against the results of experimental tests must be developed to give accurate predictions of the bridge response within this framework. The varied aspects of the bridge system are too complex to be assessed using one experimental test and are better studied through collaborative research. To address this need, two recent projects supported through the Network for Earthquake Engineering Simulation (NEES) have increased knowledge about the performance of bridges in earthquakes. The focus of these studies has been to improve understanding about soil-structure interaction on bridge system response. Shaking table tests of both a two-span and a four-span bridge at 1/4 scale were conducted at the University of Nevada, Reno. Nonlinear dynamic analyses of three-dimensional finite element models performed using OpenSees were evaluated based on the experimental test results. Parallel with the experimental studies, a prototype bridge model incorporates the influence of the abutments, drilled shaft foundations, and site response effects. Large-scale parameter studies of four prototype bridge models with and without the SFSI effect were executed on a supercomputer to quantify the SFSI effect within a performance-based engineering framework.

1.1 OBJECTIVES OF THIS RESEARCH

The research described in this report seeks to address the lack of understanding of the system effects in the seismic response of reinforced concrete bridges by harnessing new knowledge gained from experimental studies and start-of-the-art computational models and resources. To this end the following objectives are realized.

1. The first is to develop and evaluate simulation models of shaking table tests of both a two-span and a four-span reinforced concrete bridge built at 1/4 scale. The computed response from the simulation models is compared to the experimental results at both the global and local levels.
2. The second objective is to describe the modeling of a prototype bridge system that incorporates the abutments, drilled shaft foundations, and site response effects. The cyclic response of the soil at the abutments is calibrated using the results from full-scale tests. Modeling assumptions regarding the SFSI effect at the foundations are established using the results from previous research. Site response analyses compute the free-field response for each horizontal component of 80 ground motions when considering two different site conditions and four different soil profiles.
3. The final objective is to elucidate the extent to which SFSI influences the predicted demands of the prototype bridge system within a performance-based engineering framework. Large-scale parameter studies of four prototype bridge models with and without the SFSI effect calculate the response at both the global and local levels. The simulations employ the parallel capability of OpenSees and the access to a state-of-the-art supercomputer.

1.2 ORGANIZATION OF THE REPORT

Following this introduction, Chapter 2 outlines previous research regarding the seismic response of reinforced concrete bridges. Chapter 3 details the response of the shaking table tests of the aforementioned reinforced concrete bridges at the University of Nevada, Reno. Simulation models are evaluated against the results from these experiments. Chapter 4 describes the development of a prototype bridge model and the associated input excitation including the SFSI effect. In Chapter 5, the effect of SFSI on predicted demands from simulations of the prototype bridge system is presented. Chapter 6 summarizes the conclusions of the report and lists topics for future research.

2 Summary of Research on Modeling of Bridge Systems

2.1 INTRODUCTION

In preparation for developing models of bridges within a performance-based framework, the literature review in this chapter addresses previous research pertinent to the study of the seismic behavior of reinforced concrete bridges and the validation of simulations based on data recorded during experimental tests of the seismic response of instrumented bridges. Several studies on the seismic response of reinforced concrete bridge columns are discussed. Various approaches taken in validating simulations of reinforced concrete bridge components or systems are presented. Research regarding the representation of soil-foundation-structure interaction in simulation models with varying levels of complexity is discussed. The chapter concludes with a review of previous studies of the seismic fragility of bridges.

2.2 SEISMIC RESPONSE OF REINFORCED CONCRETE BRIDGE COLUMNS

Experimental tests of reinforced concrete columns under seismic loading are vital for understanding the system response of reinforced concrete bridges, since these bridges are designed to concentrate the nonlinear deformation in the columns. Previous tests of the seismic performance of bridge columns and bridge bents employ various procedures including static-cyclic tests and shaking table tests.

Lehman and Moehle (1998) performed static-cyclic tests of five 1/3-scale reinforced concrete columns to study the influence of the aspect ratio and longitudinal reinforcement ratio on the seismic response of these members. Each column was subjected to varying levels of lateral displacement to determine the behavior of the column under various damage states. Deformations were categorized according to their source: shearing, bending, or slip of the reinforcement that was anchored in the footing. The columns were designed with sufficient transverse reinforcement to guarantee failure in flexure. Based on data from strain gauges located near the base of the columns, a model was proposed to represent the bond stress distribution along the anchored reinforcement in the footing.

Mazzoni et al. (2004) assessed the performance of simulation models based on tests of the beam-column connections for a double-deck bridge as well as on data from the tests by Lehman mentioned above. Simulations were performed using a range of values and models to represent the bond stress distribution along the anchored reinforcement. The results from the simulations were compared to those from the static-cyclic experimental tests. A simplified hinge model was proposed to represent the additional flexibility due to the elongation of anchored reinforcement during dynamic loading.

Hachem et al. (2003) conducted shaking table tests of well-confined 1/4.5-scale reinforced concrete columns subjected to either unidirectional or bidirectional ground motion. A series of simulations was investigated using various assumptions regarding the modeling of reinforced concrete columns subjected to earthquake excitation. The simulation models were ranked on the basis of their relative errors for peak values of response quantities, such as displacement, curvature, shear force, and bending moment, that were observed during the experimental tests. Recommendations were developed regarding the modeling of reinforced concrete columns for dynamic loadings.

2.3 VALIDATION OF SIMULATION MODELS USING EXPERIMENTAL DATA

To incorporate knowledge gained from experimental tests into computational simulations, comparisons have been made between various aspects of the experimental response and those of the simulations. Typically, a metric is proposed that quantifies some particular aspect of the difference between the experimental and simulation responses. Response quantities that vary with time, such as displacement time histories, are often compared qualitatively through visual inspection. This section describes several procedures that have been employed by researchers in this comparison process.

In comparing the recorded embankment motions of several instrumented bridges to those computed by an analytical procedure, Zhang and Makris (2002a) considered a measure of the relative difference between the maximum responses. This comparison of discrete quantities formed the basis for evaluating the efficacy of the analytical procedure in tracking the recorded motion.

While studying the seismic performance of circular reinforced concrete bridge columns, Hachem et al. (2003) compared the ratio of various peak response quantities in the simulations to those recorded during the experiments. The simulation models were ranked by summing the absolute value of relative error amounts in the ratios of the response quantities under consideration. Comparisons were also made between damage indices calculated from the experimental tests and those determined from the simulation models.

As an alternative to comparing one discrete quantity, such as a maximum response, other metrics have been employed that include the complete response history. Grant et al. (2004) proposed a metric that considered the complete force-displacement history for the bidirectional response of isolation bearings. For each test included in the evaluation, the relative difference between the forces from the experiment and those of the simulation were integrated over the displacement response. This quantity was then normalized, and the final metric was computed as a weighted sum of individual metrics for the tests included in the evaluation process. McVerry (1980) used an error criterion in the frequency domain when performing system identification of the Millikan Library using recordings from several earthquakes. Discrete Fourier transforms of the acceleration responses were taken for both the recorded and simulated responses. The error criterion was then calculated as the mean square error divided by the mean square response for a selected frequency range.

2.4 REPRESENTATION OF SFSI IN SIMULATION MODELS

Soil-foundation-structure interaction (SFSI) consists of the modification of structural response due to the presence of a compliant foundation. For linear analyses in which SFSI is considered, the analysis typically proceeds in two stages. The first stage recognizes the modification of the free-field motion due to the presence of a massless foundation that has a different stiffness from that of the soil. This phenomenon is known as kinematic interaction and may introduce rocking and torsional modes that are not seen in a fixed-base analysis. Radiation damping occurs as the waves scattered from the foundation dissipate energy while being transmitted through the soil. The second stage is known as inertial interaction and accounts for the modification of the soil motion due to the inertial loading imposed on the soil by the structure (Kramer, 1996). Additional damping is present in the system due to the structural response as well as the hysteretic behavior of the soil, which is known as material damping.

Seminal work on SFSI effects was performed by Veletsos (1977). Veletsos considered a single-story structure supported by a rigid, circular mat on a viscoelastic half space. An equivalent linear system was formulated taking into account the additional flexibility and damping in the system due to the soil. Veletsos developed a bound on a dimensionless parameter to provide a guideline for when soil-structure interaction effects should be considered in an analysis. Among the important findings in the study were the observations that the rocking component is significant for tall, slender structures and that foundation damping may contribute greatly to the damping of the system (Veletsos, 1977).

Numerous studies have been conducted that investigate the response of reinforced concrete bridge systems under seismic loading. An extensive discussion of soil-structure interaction, including its role in the failure of the Hanshin Expressway during the 1995 Kobe earthquake (M 6.9), is presented by Gazetas and Mylonakis (1998). The following material discusses various approaches that have been taken when modeling soil-foundation-structure interaction for simulations of different levels of complexity.

McCallen and Romstad (1994) performed finite element analyses of the Painter Street overpass located in Rio Dell, California, and compared the simulation results to recorded displacements during the 1992 Cape Mendocino/Petrolia earthquake (M=7.0). Two models were studied including a simplified linear elastic stick model with soil springs based on Caltrans procedures and a detailed three-dimensional model with solid elements for the embankments, shell elements for the deck, and beam elements for the columns and pile foundations. A Ramberg-Osgood elasto-plastic model was used to match the modulus reduction and damping ratio curves for the embankment soil. McCallen and Romstad found that the simplified stick model was able to match well the recorded transverse displacement time history of the center bent only when variable modal damping was utilized. Damping ratios of 20% to 30% were required in the modes that indicated a large amount of energy dissipation in the embankments. The detailed three-dimensional finite element model provided excellent agreement with the recorded displacements for both the transverse displacement of the center bent and the longitudinal displacement of the end of the bridge. McCallen and

Romstad highlighted the need for accurate modeling of the nonlinear behavior of the embankments to capture amplitude-dependent response.

An investigation of the variation of the abutment stiffness with time at the Painter Street overpass was made by Goel and Chopra (1997). The equations of motion were formulated by assuming a rigid bridge deck, elastic springs to represent the lateral stiffnesses of the columns, and springs and dashpots to represent the stiffness and damping at the abutments. Accelerations and displacements recorded during the 1992 earthquake were used to determine the force-displacement response of the abutments at different intervals of the excitation. Goel and Chopra observed that the abutment stiffness varies with the amplitude of shaking with decreasing stiffness during strong motion and partial recovery of stiffness following strong motion. Comparisons of the calculated abutment stiffness in both the transverse and normal directions were made to those determined by the Caltrans procedure (Caltrans, 1989). In the Caltrans procedure, contributions to the abutment capacity include the resistance provided by the foundation and the passive resistance of the soil, which is assumed to have an ultimate capacity of 7.7 ksf. Abutment stiffnesses are calculated at deformations of 1 in. when the ultimate passive resistance of the soil is assumed to have been achieved, and at 2.4 in. when the onset of damage to the abutment is assumed to occur. Goel and Chopra concluded that the Caltrans procedure gives a reasonable estimate of the abutment stiffness and capacity in the transverse direction, but may overestimate the abutment capacity in the normal direction by a factor of two or more (Goel and Chopra, 1997).

Additional studies of the influence of SFSI including embankment effects for short highway overcrossings were conducted by Zhang and Makris (2002a,b). Through the use of a shear beam approximation, kinematic response functions and dynamic stiffnesses for the embankment were developed (Zhang and Makris, 2002a). The kinematic response functions relate the motion at the crest of the embankment to the motion at its base, while the dynamic stiffnesses provide constants for frequency-independent springs and dashpots to represent the flexibility and energy dissipated at the abutment. Comparisons of the 1D shear beam approximation were made to recorded crest motions at the Painter Street overpass as well as the Meloland Road overcrossing. Additional comparisons were made to 2D and 3D finite element analyses of the embankment response. In a companion paper, Zhang and Makris (2002b) evaluated the ability of a stick model, which utilized frequency-independent springs and dashpots to represent the embankments and foundation, to capture recorded motions at the aforementioned instrumented bridges. The results of these analyses indicated that the simplified stick model produces good agreement with the recorded response when calculated crest motions are used at the embankments and the additional flexibility due to the soil at the center bent is included. Comparisons were made between the simplified stick model and a detailed 3D finite element model that showed good agreement.

Another method to model SFSI utilizes the beam-on-nonlinear Winkler foundation approach as described by Hutchinson et al. (2004). In this study, the structural system under consideration was a long viaduct supported on reinforced-concrete, extended cast-in-drilled-hole pile shafts (Hutchinson et al., 2004). The soil response was modeled using p-y elements that included springs and dashpots to account for gapping, radiation damping, and the nonlinear, hysteretic behavior of the soil. The ground motions at the location of each p-y element were determined by performing 1D, equivalent-linear site response analyses assuming a baseline soil profile that included a mix of dense sands and stiff clays. Variations in the soil response were investigated by applying multipliers to the strength and stiffness parameters in the p-y elements. Based on the results of the nonlinear dynamic analyses, Hutchinson, et al. reported the relationship between maximum and residual drift ratios, the influence of P-Δ effects, and the relationship between curvature and displacement ductility for this bridge system.

Fenves and Ellery (1998) also adopted the beam-on-nonlinear Winkler foundation approach when modeling SFSI in order to investigate the failure of the Route 14/Interstate 5 separation and overhead bridge during the 1994 Northridge earthquake. The nonlinear force-deformation response of the soil was represented through the use of bilinear p-y springs based on relationships given by the American Petroleum Institute (1993). Radiation damping was not considered, since its effects were noted to be primarily in the high-frequency range. The bridge abutments were modeled to have elastic-perfectly plastic response in the longitudinal direction with a yield force determined by assuming a particular passive earth pressure acting over the backwall height. The abutment model also included consideration of the gap, radial restraint, vertical uplift, and bearing pad.

An alternative to the beam-on-nonlinear Winkler foundation approach is to determine foundation spring constants based on finite element analyses of pile groups embedded in soil. This method was employed by Jeremic et al. (2004) in studying the seismic response of the I-880 viaduct. The site under consideration included 3.0 m of dense fill at the top, 9.0 m of soft Bay Mud in the middle, and lower layers having alluvial sand. A 3D finite element analysis of the foundation was performed using linear elastic properties for both the pile group and the soil. Pushover analyses were utilized to determine the spring constants for translational and rotational springs at the base of the bridge bent. The 3D finite element analyses only considered linear elastic analysis of the soil because the deformations in the soil were small. In order to quantify the effects of SFSI on the response of the I-880 viaduct, nonlinear dynamic analyses for both a fixed base model and a model including foundation springs were conducted. Radiation damping was neglected during these analyses, since the frequency-independent foundation springs were considered to deamplify the response generally. The selected ground motions were scaled to match the uniform hazard spectrum at the elastic, cracked, and yield periods for both models under consideration. The results from the nonlinear dynamic analyses indicated that SFSI may be both beneficial and detrimental to the structural response, and recommendations were made to evaluate such effects on a case-by-case basis.

2.5 FRAGILITY ANALYSIS OF BRIDGE SYSTEMS

Recent studies have assessed the seismic performance of reinforced concrete bridges within a probabilistic framework. Mackie and Stojadinovic (2003) conducted extensive studies to quantify the relationship between ground motion intensity measures and engineering demand parameters for a range of prototype bridges designed for sites in California. The input excitation was defined by four bins of 20 recorded ground motions that were partitioned by magnitude and distance from the fault. Site response effects were not taken into account, but the ground motions were scaled by a factor of two to introduce additional nonlinearity into the structural response. The simulation model in OpenSees represented the nonlinear response of the columns, abutments, piles, and lateral resistance of soil along the length of the piles. At the abutments, the hysteretic response of the bearing pads, piles, and passive soil resistance at the backwall and wing walls were modeled. The embankment effect was considered through the incorporation of a participating mass and additional stiffness. Along the drilled shaft foundations, elastic-perfectly-plastic springs modeled the p-y response of the sandy soil. Both linear and bilinear regressions were fit to the data to develop demand models for response at both the global and local levels.

Subsequent studies by Padgett and DesRoches (2009) evaluated bridge system vulnerability and identified retrofit strategies for bridges in the Central and Southeastern United States (CSUS). Both steel and reinforced concrete multi-span bridges without seismic detailing were studied. The potential retrofit measures included steel column jackets, elastomeric bearings, steel restrainer cables, seat extenders, and shear keys. Three-dimensional nonlinear dynamic analyses in OpenSees computed the bridge system response for a suite of 48 ground motions developed for the CSUS. The simulation model represented the columns, deck pounding, foundations, and abutments. Linear translational and rotational springs modeled the response of the pile foundations at the bases of the columns. Nonlinear elements included the passive, active, and transverse response at the abutments. Fragility curves were developed to establish the probability of realizing a damage state for a given level of ground motion intensity. When considering the worst-case damage scenario, seat extenders provided the most effective retrofit measure both from a cost and from a structural performance standpoint.

3 Modeling and Simulation of Bridges Using Data from Large-Scale Shaking Table Tests

3.1 INTRODUCTION

This chapter describes shaking table tests of a two-span and a four-span bridge conducted at the University of Nevada, Reno (UNR), as well as accompanying simulations performed using the Open System for Earthquake Engineering Simulation (OpenSees) software platform (McKenna et al., 2000). The bridge design, test protocol, and selected results from the tests of each bridge are presented. The subsequent portion discusses the simulation models used in validation studies comparing the simulation results to the measured response.

3.2 DESCRIPTION OF LARGE-SCALE SHAKING TABLE TESTS

3.2.1 Two-Span Bridge

Shaking table tests of a 1/4-scale reinforced concrete bridge with two spans supported by two-column bents were performed at UNR. These tests give insight into the system behavior of the superstructure and substructure of the bridge system during earthquake excitation. An extensive description of the design of the bridge and the results of the shaking table tests is presented by Johnson et al. (2006). For the purpose of completeness of this report, the following details a summary of the specimen design, selection of support motions, and response data from the shaking table tests using information given by Johnson et al. (2006).

Specimen Design

The two-span bridge was designed based on a prototype that is a continuous post-tensioned bridge with varying column heights supported on continuous drilled shafts. A span length of 120 ft for the prototype bridge accommodates the 30 ft spacing of the shaking tables at model scale. The prototype bridge has distances from the top of the column to the point of fixity of 20 ft, 32 ft, and 24 ft for the three bents, respectively. The design assumes that the point of fixity occurs at the point of maximum moment for each column when considering a linearly varying moment distribution. A depth of two column diameters below the ground surface locates the point of maximum moment. Column heights are 6 ft, 8 ft, and 5 ft for bents 1, 2, and 3, respectively, as shown in Figure A.1.

Detailing requirements for the reinforced concrete columns and joints comply with guidelines developed through the National Cooperative Highway Research Program Project 12-49 (ATC, 2003). The main design constraint includes a longitudinal reinforcement ratio of 1.56% with 16-#3 Grade 60 bars. Since the demand in the NCHRP 12-49 guidelines is determined by the site of the bridge, the selected site ensures that the longitudinal reinforcement ratio provides sufficient capacity to meet the requirements. The site is located in the Los Angeles area at a distance of at least 10 km from a fault to avoid any consideration of near-fault effects. The site is situated on soil with a shear wave velocity of 3300 ft/sec. The design spectra include both the expected (50% in 75 yrs) and rare (3% in 75 yrs) events and use the spectral acceleration values at 0.2 sec and 1.0 sec for a site with soil type B. The life-safety performance objective considered R values of 1.3 and 6.0 for the expected and rare events, respectively. From design checks computed in accordance with NCHRP 12-49, the expected event governs the design. The site considered represents low to moderate seismic demand for a location in the Los Angeles area.

A column diameter of 4 ft for the prototype bridge results in an axial load ratio of 0.08, which is within a typical range for reinforced concrete bridge columns. Transverse reinforcement designed at model scale in accordance with NCHRP 12-49 meets both the confinement requirements and provides proper shear capacity. The transverse reinforcement is W2.9 spiral reinforcement at 1.25 in. with Grade 60 steel. While the columns have different span-to-depth ratios, each column has the same transverse reinforcement ratio to satisfy the global buckling requirements given in the commentary of NCHRP 12-49. A concrete cover of 0.75 in. at model scale meets similitude requirements for other tests within the NEES project.

The design requires the bent caps to remain elastic during the shaking table tests. The dimensions for these members allow for sufficient length to transfer moment from the column to the bent cap and to support the slab members that constitute the superstructure. Longitudinal and transverse reinforcement follow AASHTO (American Association of State Highway and Transportation Officials, 2002) and Caltrans (2000) requirements. The bent caps at bents 1 and 3 include cantilevers to support the masses that are placed at the bridge ends.

The design philosophy for the beam-column joints stipulates that the failure mode should be in flexure rather than from joint shear or slippage of column reinforcement out of the cap beam. Detailing requirements for the joints follow the guidelines from Caltrans SDC (Caltrans, 2004) and NCHRP 12-49. Special mechanical anchorage for the column longitudinal reinforcement prevents it from slipping out of the joint due to bond failure.

The superstructure of the prototype bridge is a continuous, post-tensioned box girder designed using the AASHTO Standard Specifications (American Association of State Highway and Transportation Officials, 2002). Since the test specimen is post-tensioned, the cross section at model scale has the same flexural stiffness but does not have the same geometry of the box girder cross section. A rectangular cross section 90 in. wide and 14 in. deep satisfies the bending stiffness requirements. Different segments with cross sections 30 in. wide and 14 in. deep form the superstructure. Post-tensioning in both the longitudinal and transverse directions preserves continuity and restricts the superstructure to remain uncracked.

External masses, including concrete and lead blocks located along the length of the bridge, comprise the additional dead load of the bridge resulting in an axial load ratio of nearly 0.08 at each bridge column.

Specified Support Motions

Researchers at the University of Washington and the University of California, Davis performed a study to select ground motions for the shaking table tests. The outcrop motion was the 090 component of the Century City North ground motion (measured at a location 25.7 km from the fault rupture) that occurred during the 1994 Northridge earthquake (M 6.7). Site response analysis at prototype scale assumed that the soil profile consisted of Nevada sand ($D_r = 80\%$). Using ProShake (EduPro Civil Systems, Inc., 1999), the analysis deconvolved the outcrop motion to obtain the bedrock motion by assuming a particular depth to bedrock for the test under consideration. Site response analyses performed using OpenSees then determined the ground motion at two column diameters (8 ft) below the ground surface.

The testing protocol included a series of low-level tests for which the structure would not yield, followed by a series of tests with increasing amplitude until failure of the bridge structure occurred. During the first 12 tests, the input bedrock ground motion had a peak bedrock acceleration of 0.06 g. To model the free-field site response due to this bedrock motion, the selected soil profiles assumed various depths from the bedrock to the point of fixity, up to 58.1 ft. These first 12 tests considered both coherent and incoherent motions, which were generated with different depths to bedrock under the three bridge bents. The next two tests applied ground motions measured during the centrifuge tests with a peak bedrock acceleration of 0.10 g. The remaining nine tests assumed a peak bedrock acceleration of 0.40 g with the bedrock lying 87.2 ft below the point of fixity. The target motions correspond to the free-field motions at the point of fixity rather than the pile motions, since the motions at these locations were not significantly different (Shin, 2007).

Selected Bridge Response Data

The testing protocol included the maximum measured table and bent accelerations as shown in Table A.1. Table A.2 lists measured maximum and residual drift ratios throughout the tests. As reported by Johnson et al. (2006), no damage occurred until Test 13, where minor flexural cracks appeared in bent 1. Based on the strain gauge data, yielding of the columns initiated during Test 13 at bents 1 and 3 and during Test 15 at bent 2. Flexural cracks developed in bents 1 and 3 during Test 15 with up to 4 in. of spalling occurring in bent 3. Spalling continued to develop in bents 1 and 3 during Tests 16 and 17 resulting in exposure of the transverse reinforcement. During Test 18, transverse reinforcement in bent 2 began to become exposed, the maximum drift ratio in bent 3 was 5.5%, and the longitudinal reinforcement in bent 3 was exposed and at the onset of buckling. During Test 19, bent 3 failed with several spiral hoops fracturing and a significant number of longitudinal bars buckling. Following Test 20, longitudinal reinforcement in bent 3 fractured, while the additional damage accumulated in bents 1 and 2 was insignificant.

3.2.2 Four-Span Bridge

A subsequent NEES project considered the seismic performance of a reinforced concrete bridge including abutments at the bridge ends. Shaking table tests of a 1/4-scale reinforced concrete bridge with four spans supported by two-column bents and abutments were performed at UNR.

These tests give additional insight into the seismic behavior of the bridge system with abutments. An extensive description of the design of the bridge and the results of the shaking table tests is presented by Nelson et al. (2007). The following summarizes selected information pertinent to the design, testing, and response of the four-span bridge.

Specimen Design

Column heights for the four-span bridge are 5 ft, 7 ft, and 6 ft for bents 1, 2, and 3, respectively, as shown in Figure A.1. The interior and end spans are 348 in. and 294.25 in. long, respectively, to meet the space restrictions within the structures facility at UNR. At the ends of the bridge, reaction blocks support the abutments that seat the bridge deck. The abutments have an embedded steel wide flange section that slides within a teflon-coated guide restricting movement in the longitudinal direction only. Each column uses the same longitudinal and transverse reinforcement as in the two-span bridge with 0.5 in. of cover concrete. Additional mass loads the bridge to an axial load ratio of 7% in bent 2 and 7.3% in bents 1 and 3. One major difference between the design of the four-span bridge with that of the two-span bridge is the cap beam detail. The cap beam consists of two separate members, a bent cap beam of square cross section that is integral with the columns, and an inverted T-beam to which the prestressed concrete girders are connected. The inverted T-beam rests on steel bearing plates and hydrostone and two post-tensioned rods fasten it to the bent cap beam. Due to this detail, there is much greater flexibility at the top of the columns for rotation about the transverse axis than in the two-span bridge.

Specified Support Motions

The ground motion assumed for the high-level tests of the two-span bridge is the target table motion used in the tests of the four-span bridge. Site response analysis determined the target motions at the point of fixity for both horizontal components of the Century City North ground motion. The input at the base of the soil has a peak bedrock acceleration of 0.40 g in the transverse direction. The bedrock lies 87.2 ft below the point of fixity for a soil profile consisting of Nevada sand (D_r = 80%). Simulations in OpenSees prior to the tests calculated the displacement time histories at the bridge ends due to the response of an assumed abutment model (Zadeh and Saiidi, 2007). The target displacement input for the actuators at the abutments follows the pre-test simulation results.

Selected Bridge Response Data

Over the course of 12 tests, the bridge withstood table accelerations as high as 1.5 g and bent accelerations as high as 1.2 g as shown in Tables A.3 and A.4. Tables A.5 and A.6 list the peak and residual drift ratios, respectively, at each bent in both horizontal directions. During Tests 1B, 4A, and 4B, restrainers made of either steel or a shape memory alloy (SMA) modified the response at the abutments as part of a NEES payload project. The shaking table hydraulic system shut down during Test 5 due to safety issues resulting in a shorter duration for this test. During Test 6, the columns in bents 1 and 3 had significant spalling and the longitudinal reinforcement in bent 1 was at the onset of buckling. Substantial damage occurred in bent 1 during Test 7 with buckling and fracture of the longitudinal reinforcement. Residual drift ratios exceeded 2.7% for bent 1 and 1.4% for bent 3 following Test 7. The bridge abutments sustained heavy pounding during the high-level tests without failure of the backwall.

System Identification Studies

System identification studies using measured data during Tests 1D and 2 allow the vibration frequencies and mode shapes of the four-span bridge to be determined. The system is idealized with a multiple-input/multiple-output (MIMO) ARX model. The ARX model is given by:

$$y(t) + \sum_{i=1}^{n_a} A_i y(t - i\Delta t) = \sum_{j=1}^{n_b} B_j u(t - j\Delta t) + e(t) \tag{3.1}$$

where $y(t)$ is the vector of outputs at time t, $y(t - i\Delta t)$ and $u(t - j\Delta t)$ are the vectors of previous outputs and inputs, n_a and n_b are the model orders, A_i and B_j are matrices containing the model parameters, and $e(t)$ is the error term. The system is solved using the arx function in Matlab by minimizing the trace of the prediction error covariance matrix (Matlab, 2007). Extensive system identification studies of the two-span bridge, including the determination of frequencies and mode shapes using a MIMO ARX model, were performed by Ranf (2007).

To define the response of the bridge system, the inputs included the table accelerations measured in both the transverse and longitudinal directions, and the outputs included data measured from the six accelerometers shown in Figure 3.1. The measured data was filtered using an 8th-order lowpass Chebyshev Type I filter with a cutoff frequency equal to 20 Hz. The stability diagram in Figure 3.2 compares the variation of the identified frequencies with increasing model

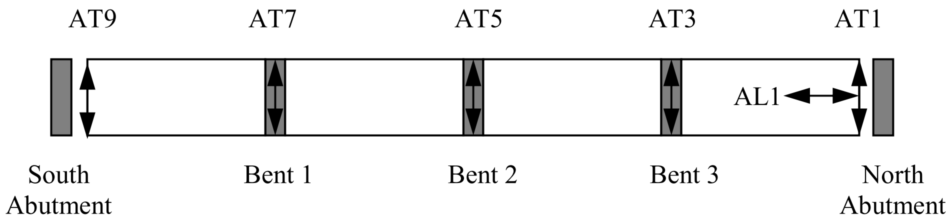

Fig. 3.1 Location of accelerometers used in system identification studies of the 4-span bridge.

order. The modal phase collinearity (Pappa and Elliott, 1993) is used to quantify the extent to which the mode shapes display monophase behavior. Data points are plotted according to which of the following selection criteria are met: a relative difference of less than 10% with increasing model order for the frequency or damping ratio and MPC $\geq$ 0.85. Similar selection criteria were used by Pakzad (2008) in system identification studies of the Golden Gate Bridge. The identified frequencies, damping ratios, and computed MPC values for increasing model order are tabulated in Table 3.1. The mode shapes and frequencies vary greatly from Test 1D to Test 2 as shown in Figure 3.4. The mode associated with twisting about bent 2 for translation in the transverse direction is much more flexible during Test 1D than Test 2. This discrepancy stems from the extent to which significant pounding occurs at the abutments during these tests. The measured absolute transverse and relative longitudinal deck displacements at the south end of the bridge are plotted in Figure 3.3. Pounding at the bridge ends during Test 2 restricts the motion of the bridge deck in the transverse direction to a greater extent observed during Test 1 resulting in greater stiffness for the aforementioned mode.

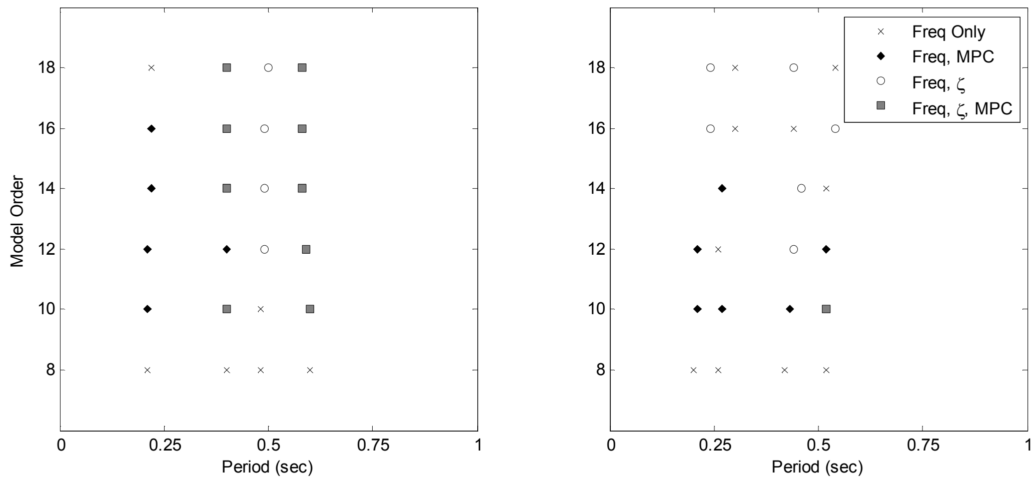

Fig. 3.2 Stability diagrams from system identification of the 4-span bridge using measured data during Tests 1D and 2.

Table 3.1 Results from system identification studies of the 4-span bridge.

Test 1D												
Model Order	T_1 (sec)	ζ_1 (%)	MPC	T_2 (sec)	ζ_2 (%)	MPC	T_3 (sec)	ζ_3 (%)	MPC	T_4 (sec)	ζ_4 (%)	MPC
8	0.60	9.66	0.88	0.48	12.43	0.10	0.40	10.39	0.95	0.21	3.76	1.00
10	0.60	9.19	0.87	0.48	16.61	0.20	0.40	10.58	0.97	0.21	6.38	0.98
12	0.59	8.87	0.91	0.49	17.79	0.08	0.40	12.05	0.97	0.21	7.30	0.95
14	0.58	9.69	0.91	0.49	19.29	0.12	0.40	12.27	0.97	0.22	8.71	0.91
16	0.58	9.62	0.89	0.49	20.14	0.15	0.40	12.39	0.98	0.22	9.95	0.85
18	0.58	9.62	0.91	0.50	18.64	0.31	0.40	12.13	0.98	0.22	11.14	0.83
Test 2												
8	0.52	7.55	0.95	0.42	9.47	0.92	0.26	1.07	0.97	0.20	7.50	0.99
10	0.52	7.99	0.96	0.43	8.37	0.93	0.27	0.94	0.98	0.21	11.67	0.94
12	0.52	7.10	0.86	0.44	8.58	0.74	0.26	11.40	0.80	0.21	17.97	0.89
14	0.52	6.44	0.70	0.46	8.66	0.44	0.27	13.35	0.95	0.24	22.42	0.90
16	0.54	6.45	0.71	0.44	6.91	0.54	0.30	16.15	0.60	0.24	22.42	0.19
18	0.54	5.60	0.59	0.44	6.33	0.50	0.30	19.59	0.14	0.24	21.77	0.52

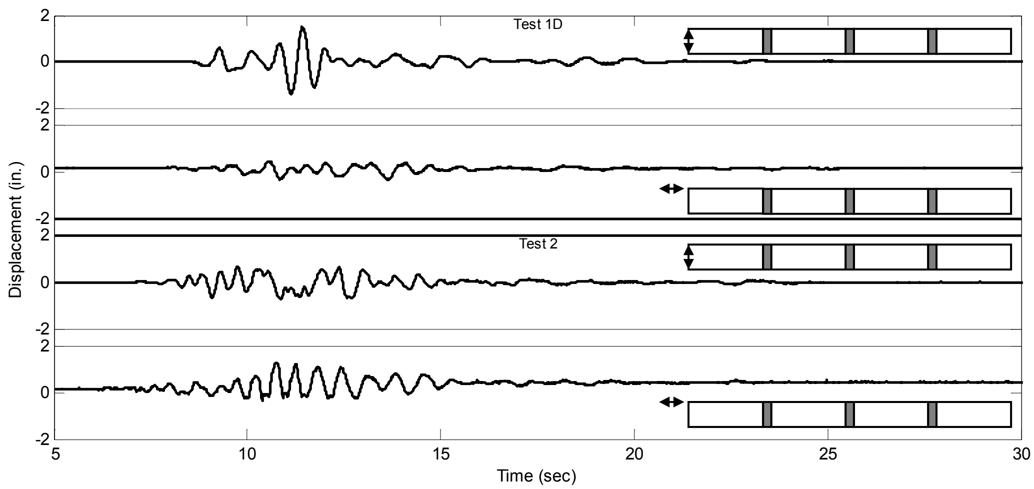

Fig. 3.3 Measured absolute transverse and relative longitudinal deck displacements at the south end of the 4-span bridge during Tests 1D and 2.

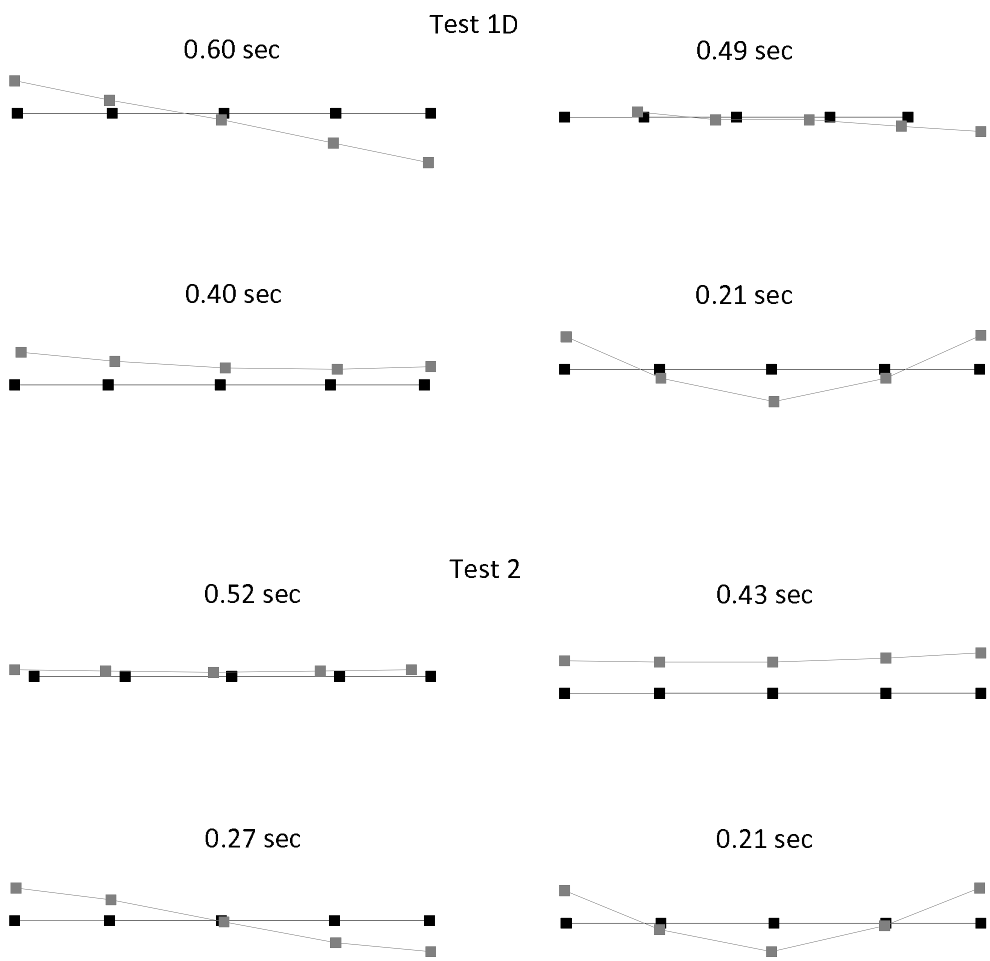

Fig. 3.4 Mode shapes from system identification of the 4-span bridge using measured data during Tests 1D and 2. The results are shown for a model order equal to 10.

3.3 DESCRIPTION OF SIMULATION MODELS

While one purpose of the experimental tests is to provide insight into the system behavior of a reinforced concrete bridge, they also serve as a benchmark to which simulation models may be calibrated and validated. Simulations of the shaking table tests have been performed using OpenSees (McKenna et al., 2000). A calibration procedure has been developed wherein pertinent parameters for the simulation model are selected to correlate with the global response recorded during two specific experimental tests. Additional simulation models are developed using various assumptions regarding the strain penetration along the anchored reinforcement at the column ends. For the simulations, the earthquake excitation is applied to the model using the recorded actuator displacements and neglects any interaction between the hydraulic system and the structure.

3.3.1 Material Modeling

To represent the nonlinear response of the bridge specimen under dynamic loading, it is necessary to model accurately the cyclic response of the materials in the structure. The following describes the material models utilized in the simulation model and the selection of parameters to provide agreement with the experimental data.

Concrete

Concrete is modeled using the Concrete02 uniaxial material in OpenSees. The monotonic response is based on the work of Kent and Park (1971) and was modified by Scott et al. (1982). Further work by Yassin (1994) extended this model to incorporate unloading and reloading with degrading stiffness and linear tension softening. The peak strength for the unconfined concrete model is based on tests of concrete cylinders performed near the date of the shaking table tests. The confined concrete compressive strength, ${f'}_{cc}$, has been calculated in accordance with the work of Mander et al. (1988) and is:

$$ {f'}_{cc} = {f'}_{co}\left(-1.254 + 2.254\sqrt{1 + \frac{7.94{f'}_l}{{f'}_{co}}} - 2\frac{{f'}_l}{{f'}_{co}}\right) \tag{3.2} $$

where f'_{co} is the unconfined concrete compressive strength. The effective lateral confining stress, f'_l, due to the spiral reinforcement is:

$$f'_l = \frac{1}{2}\left(\frac{1-\frac{s'}{2d_s}}{1-\rho_{cc}}\right)\rho_s f_{yh} \tag{3.3}$$

where s' is the clear vertical spacing between spiral bars, d_s is the diameter of spiral between bar centers, ρ_{cc} is the ratio of area of longitudinal reinforcement to area of confined concrete core, ρ_s is the ratio of the volume of transverse confining steel to the volume of confined concrete core, and f_{yh} is the yield strength of the transverse reinforcement. The ultimate strain for the confined concrete was determined using the energy balance approach developed by Mander et al. (1988). The parameters for the concrete material models that were used in the simulations are listed in Table 3.2. The response of these models under cyclic loading is shown in Figure 3.5.

Table 3.2 Concrete material properties.

Test	Concrete Type	$f'_{co}(ksi)$	ϵ_{co}	$f'_{cu}(ksi)$	ϵ_{cu}
2-Span	Unconfined	5.9	0.002	0.0	0.006
	Confined	7.5	0.0048	4.8	0.022
4-Span	Unconfined	6.7	0.002	0.0	0.006
	Confined	8.3	0.0044	4.7	0.024

Steel

The Hysteretic uniaxial material model in OpenSees was selected to model the response of the steel reinforcement to match the monotonic response observed during the steel coupon tests. The parameters included in this model are noted in Table 3.3. A comparison of the monotonic response of the steel material model with the results of the coupon tests, as well as a plot of the response of the steel material model under cyclic loading, is shown in Figure 3.6.

3.3.2 Column Modeling

Strain Penetration at Column Ends

Additional deformation at the column ends results from elongation of the steel reinforcement at beam-column joints as well as column-to-foundation connections. As shown in Figure 3.7, a bi-uniform bond stress distribution is assumed along the length of the anchored bar based on the

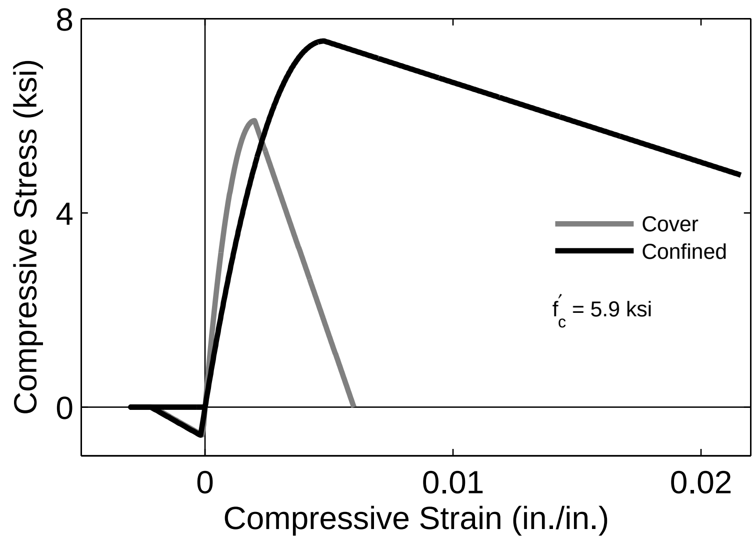

Fig. 3.5 Material models for confined and unconfined concrete models used in simulations of the 2-span tests.

Table 3.3 Steel material properties.

Test	$F_1(ksi)$	ϵ_1	$F_2(ksi)$	ϵ_2	$F_3(ksi)$	ϵ_3
2-Span	67	0.0023	92	0.028	97	0.12
4-Span	61	0.0021	91	0.028	97	0.12
	pinchX	pinchY	damage1	damage2	beta	
	0.4	0.6	0.0	0.0	0.25	

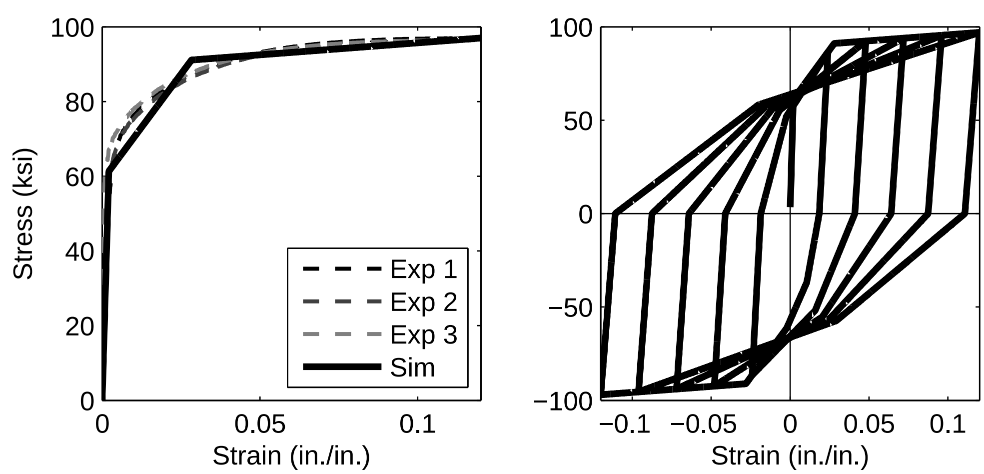

Fig. 3.6 Material modeling of steel reinforcement.

simplified model developed by Lehman and Moehle (1998). The relationship between the stress

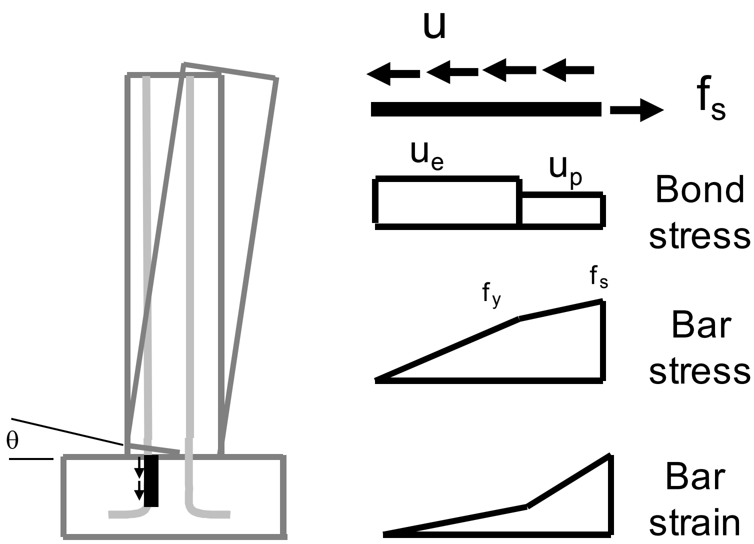

Fig. 3.7 Rigid-body rotation due to bar slip (based on Mazzoni et al. (2004)).

in the reinforcing bar and the bond stress along the surface is given by equilibrium. Prior to yield, the bar stress is:

$$f_s = \frac{\pi d_b u_e l_d}{A_b} \tag{3.4}$$

where f_s is the bar stress, A_b is the cross-sectional area of the bar, d_b is the bar diameter, u_e is the elastic bond stress, and l_d is the development length. After yield, the strain-hardening branch follows a parabolic curve given by the relationship developed by Mander (Chang and Mander, 1994):

$$f_s = f_u + (f_y - f_u)\left(\frac{\epsilon_{su} - \epsilon_s}{\epsilon_{su} - \epsilon_{sh}}\right)^P \tag{3.5}$$

where f_u is the ultimate stress, f_y is the stress at yield, ϵ_s is the steel strain, ϵ_{sh} is the steel strain at the onset of strain hardening, ϵ_{su} is the ultimate steel strain. The exponent P is:

$$P = E_{sh}\left(\frac{\epsilon_{su} - \epsilon_s}{f_u - f_y}\right) \tag{3.6}$$

where E_{sh} is the strain-hardening modulus that is assumed to be 1500 ksi. At yield, the anchorage length necessary to equilibrate the bar stress is:

$$l_e = \frac{f_y d_b}{4u_e} \tag{3.7}$$

Subsequent to yielding, the additional development length, l_p, required for equilibrium is:

$$l_p = \frac{(f_s - f_y)d_b}{4u_p} \tag{3.8}$$

where u_p is the plastic bond stress. The total development length for the bond stress distribution to equilibrate the force in the bar is:

$$l_d = l_e + l_p \tag{3.9}$$

The bar elongation, δ, may then be determined by integrating the strain over the development length:

$$\delta(x) = \int_0^{l_d} \epsilon_s(x)dx \tag{3.10}$$

The stress-slip relationship is calculated using bond stress values based on a calibration done by Ranf (2007) to match strain gauge data recorded along the length of the anchored reinforcement during the shaking table tests of the two-span bridge. The bond stress is assumed to have constant bond stress of $u_e = 8\sqrt{f'_c}$ over the portion of the bar that remains elastic and a constant bond stress of $u_p = 4\sqrt{f'_c}$ over the remaining portion of the bar. Slip values are computed for the three stress values used to define the backbone curve for the material response of the steel reinforcement as was discussed in Section 3.3.1. The stress-slip relationship for the steel reinforcement is shown in Figure 3.8.

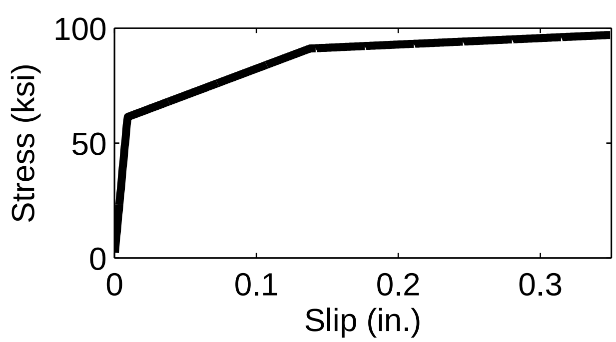

Fig. 3.8 Stress-slip response for steel reinforcement.

Column Modeling Approaches

Three different approaches are considered for modeling the reinforced concrete columns in the simulations. Each model includes a forceBeamColumn element based on the force formulation presented by Spacone et al. (1996). Using the principle of virtual work, the element deformations are computed through numerical integration of the curvature along the length of the element as discussed in a summary of the force formulation by Filippou and Fenves (Bozorgnia and Bertero, 2004). The section response is evaluated using a cross-section discretization with two and four subdivisions in the radial direction for the core and cover concrete, respectively, and 16 subdivisions in the tangential direction. The reinforcement details and column geometry are listed in Table 3.4. The moment-curvature response for the column sections in the two-span and four-span tests is shown in Figure 3.9 for an axial load index of 0.08. The yield curvature is defined from a bilinear approximation to the moment-curvature curve as defined in the Caltrans Seismic Design Criteria (Caltrans, 2004). Special consideration must be taken when validating the local response of this

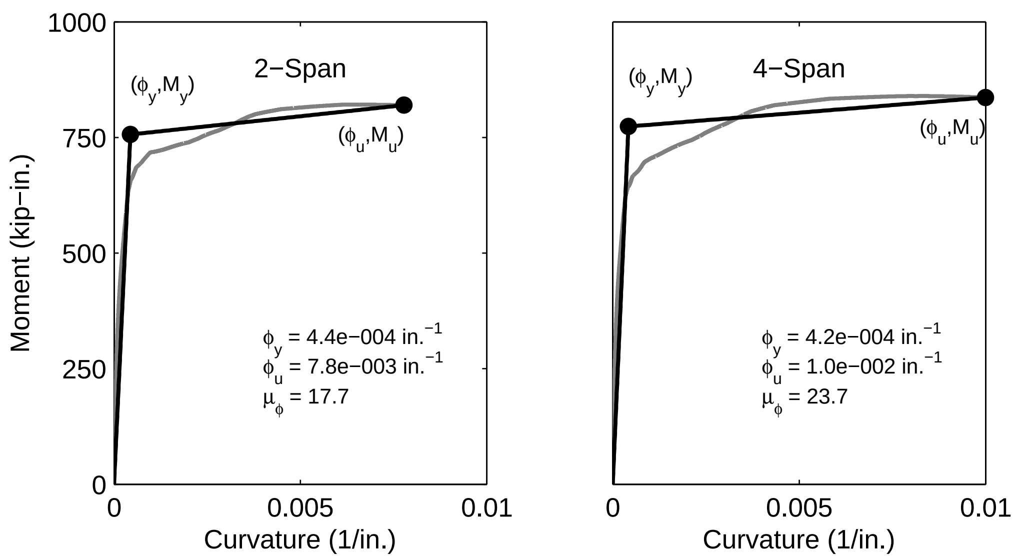

Fig. 3.9 Moment-curvature analysis of reinforced concrete circular column sections used in the 2-span and 4-span bridges. Bilinear approximations are determined for the purpose of computing curvature ductilities.

Table 3.4 Column geometry and reinforcement details.

	2-span	4-span
cover	0.5 in.	0.75 in.
D_{col}	12 in.	
ρ_{long}	1.56 %	
ρ_{lat}	0.9 %	

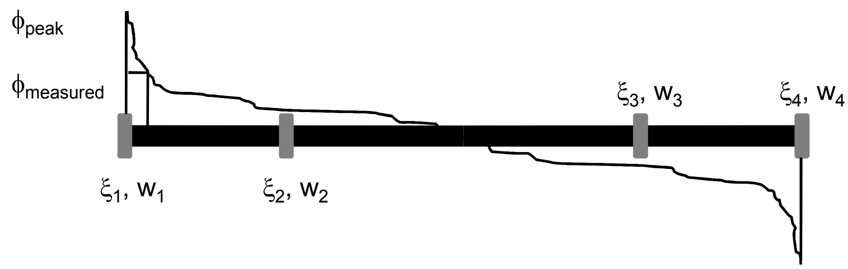

Fig. 3.10 Comparison of determination of peak calculation in the experiment and simulation. The integration points and weights are shown for determination of the element response in the simulation.

element based on the experimental results. The peak curvature is sampled at the element end in the simulation model for the purposes of numerical integration. In the experimental setup, the curvatures are averaged using rotation measurements from displacement transducers as was discussed in Section 3.2.1. While the average curvatures from the experiment do include the effect of the additional flexibility at the column ends due to strain penetration along the anchored reinforcement, they are measured five in. from the column ends and thus do not capture the peak column curvature. Figure 3.10 illustrates that the peak curvatures from the simulation may be much larger than those measured from the experiment due to the large strain gradient that exists at the column ends.

The column models differ in the way they account for the additional flexibility at the column ends due to strain penetration along the anchored reinforcement. An illustration of the different models is shown in Figure 3.11. The first one represents the columns by using a nonlinearBeamColumn element with four-point Gauss-Lobatto quadrature and zero-length elements at the column ends. The zero-length elements, proposed by Mazzoni et al. (2004), include degrees of freedom describing the moment-rotation response about the longitudinal and transverse axes of the bridge to account for bar slip. As discussed in Mazzoni et al. (2004), bar slip occurs in two modes: elongation due to the variation in strain along the length of the anchored bar resulting from bond to the surrounding concrete, and rigid body slip of the bar that is resisted by friction from the surrounding concrete. Since the joints in the shaking table specimen included sufficient anchorage of the reinforcement, the latter mode of slip is not included. The response is modeled using the Hysteretic uniaxial material, which consists of a backbone curve that is described by three points

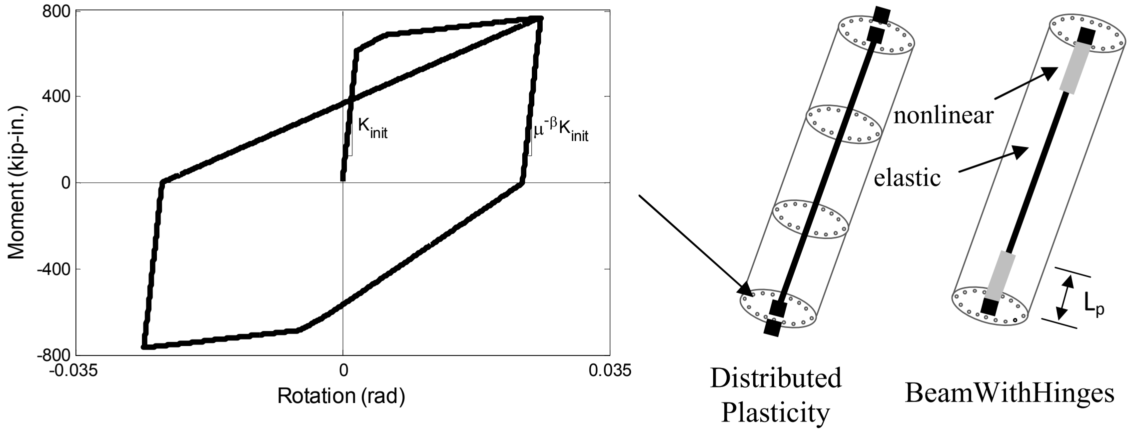

Fig. 3.11 Column models considered in the simulations.

in the positive and negative directions, respectively. The model developed by Mazzoni et al. (2004) accommodates the limitations of the Hysteretic material by basing the moment-rotation response on three stages from the moment-curvature analysis of the cross-section as shown in Figure 3.12.

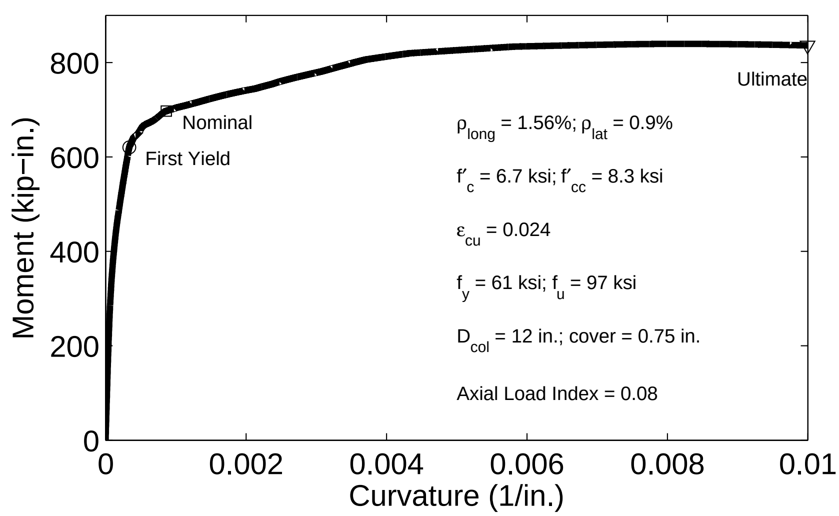

Fig. 3.12 Moment-curvature analysis of reinforced concrete circular column section used in the 4-span bridge.

These stages correspond to first yield of the reinforcement, nominal moment where the outermost fiber in compression reaches $\epsilon_c = 0.003$, and ultimate moment when the confined concrete crushes. For each stage, the stress in the outer reinforcing bar in tension is determined, and the corresponding slip is computed using the relationship shown in Figure 3.8. The section rotation is then:

$$\theta = \frac{\delta}{d_{NA}} \tag{3.11}$$

where δ is the bar elongation of the outermost bar in tension and d_{NA} is the distance from the outermost bar in tension to the neutral axis.

The other two column models include the beamWithHinges element with a plastic hinge integration method developed by Scott and Fenves (2006). This quadrature rule enables the analyst to specify the lengths over which nonlinear response is assumed to occur at the element ends while restricting the interior of the element to remain elastic. Two modeling recommendations are followed to determine the fixed plastic hinge length, L_p, and the flexural stiffness for the interior elastic region of the element. The first approach uses the relationship for L_p given by Priestley et al. (1996):

$$L_p = 0.08L + 0.15 f_{ye} d_{bl} \leq 0.3 f_{ye} d_{bl} \qquad (f_{ye} \text{ in ksi}) \tag{3.12}$$

where L is the distance from the column end to the point of contraflexure, taken as one half the clear column height, f_{ye} is the yield strength of the longitudinal reinforcement, and d_{bl} is the diameter of the longitudinal reinforcement. The elastic portion of the element is assumed to have an effective stiffness equal to M_y/κ_y found from the moment-curvature analysis of the cross-section.

The second column modeling approach using the beamWithHinges element incorporates modeling recommendations by Berry et al. (2008). Using data from 37 tests of well-detailed bridge columns, Berry proposed relationships for the plastic hinge length and effective elastic stiffness based on regression analyses. The effective stiffness is modified to ensure compatibility between the yield displacement computed from a hand calculation with that computed from the beamWithHinges element. A comparison of the plastic hinge lengths and effective stiffness for the column models that include the beamWithHinges element is shown in Table 3.5.

Table 3.5 Comparison of plastic hinge lengths and effective stiffness for beamWithHinges elements.

	L_p/D_{col}		
	Bent 1	Bent 2	Bent 3
Priestley (Priestley et al., 1996)	0.52	0.60	0.48
Berry (Berry et al., 2008)	0.37	0.42	0.34
	EI_{eff}/EI_g		
	Bent 1	Bent 2	Bent 3
M-κ	0.37	0.37	0.37
Berry (Berry et al., 2008)	0.32	0.37	0.29

3.3.3 Bent Cap

The bent cap beams are modeled using linear elastic beam-column elements with geometric properties calculated using assumptions regarding the effective width of the cap beam and reduction of its stiffness due to cracking. As shown in Figures 3.13 and 3.14, different cap beam designs were used for the two-span and four-span bridges. For the two-span bridge model, the cap beams at all bents are assumed to have a depth of 15 in. and an effective width of 15 in. The effective width is selected as such given that the amount of longitudinal reinforcement outside this effective width is small. A rigid-joint offset of 8 in. in the vertical direction and 6 in. in the horizontal direction is applied at the top of the columns to model the rigid behavior of the beam-column joints. For the four-span bridge model, two separate beams contribute to the flexural resistance of the bents during motion in the transverse direction. The 15 in. by 15 in. cap beam is integral with the reinforced concrete columns and transfers moment through the beam-column joint. An inverted T-beam is connected to the cap beam using vertical steel rods placed at two locations along the length of the beam and hydrostone is applied at the interfaces. The inverted T-beam supports the prestressed concrete beams that form the bridge deck.

The cap beams are modeled using linear elastic beam-column elements with rigid joint offsets to account for the beam-column joints. At each end of the bridge bent, two nodes are placed at the location of the interface between the inverted T-beam and the square cap beam as shown in Figure 3.15. A rigidLink bar constrains the translational degrees of freedom of these nodes. A zero-length element is used to introduce rotational flexibility at these interfaces for rotation about the axis shown in Figure 3.15 during longitudinal movement of the bridge. As is discussed in

Section 3.5.2, the rotational flexibility is calibrated to match the results of system identification studies of the four-span bridge. A reduction factor, α, is applied to the flexural stiffness to account for cracking in the member. Based on the recommendations of the Caltrans Seismic Design Criteria (SDC) (Caltrans, 2004), the value of α may be selected within the range of $0.5 - 0.75$, where 0.5 corresponds to a lightly reinforced section, and 0.75 corresponds to a heavily reinforced section.

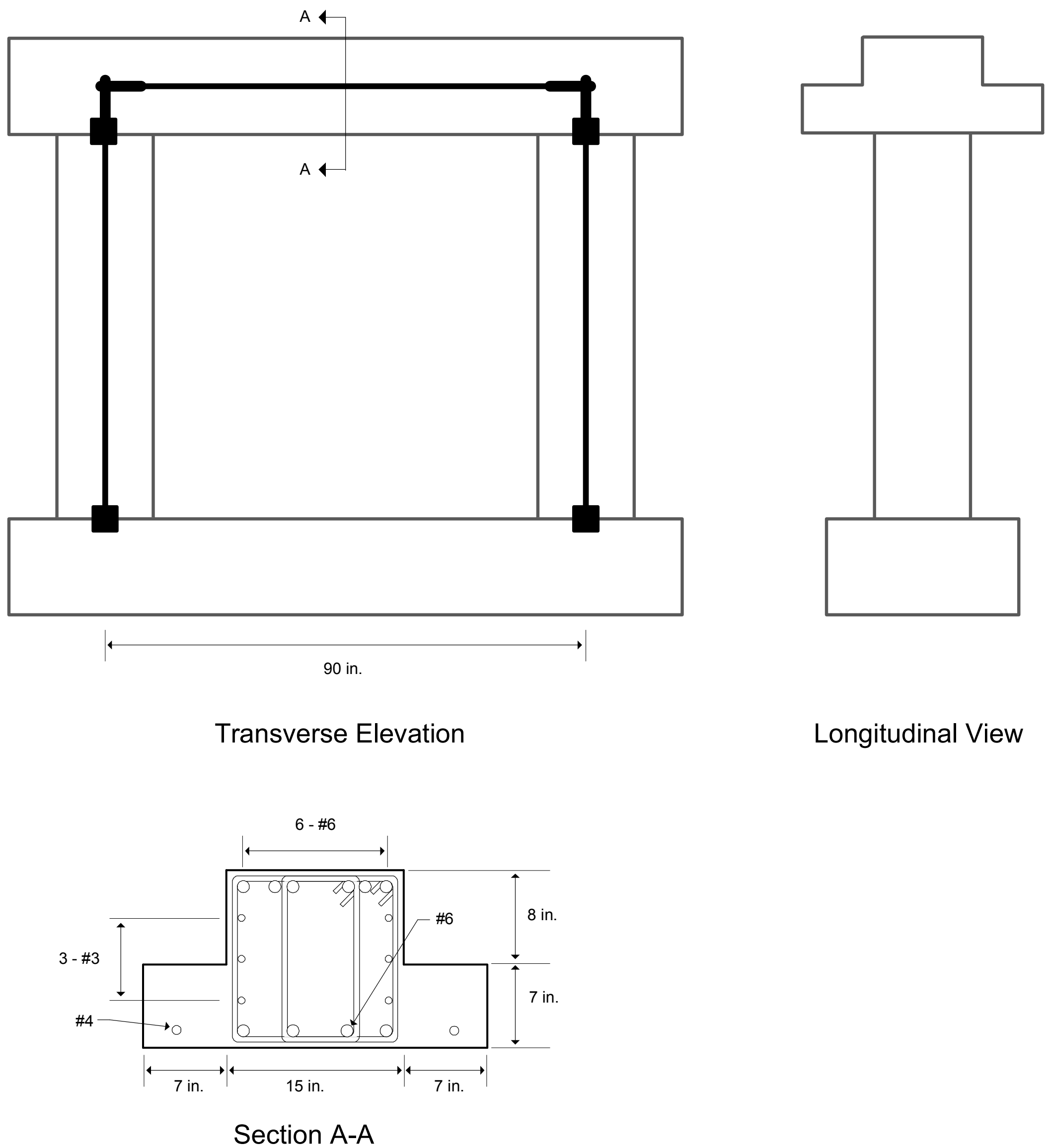

Fig. 3.13 Cap beam details for the 2-span bridge.

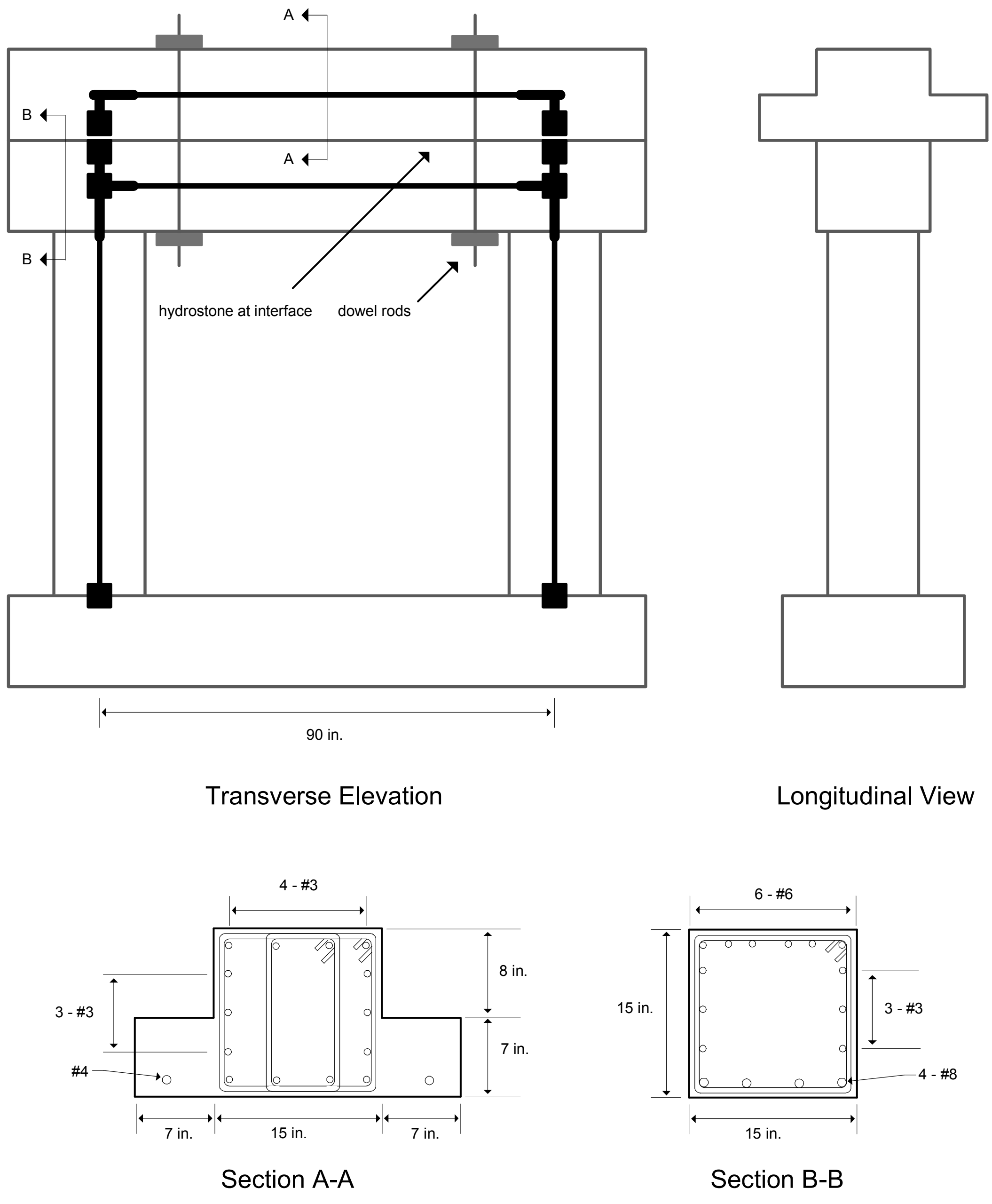

Fig. 3.14 Cap beam details for the 4-span bridge.

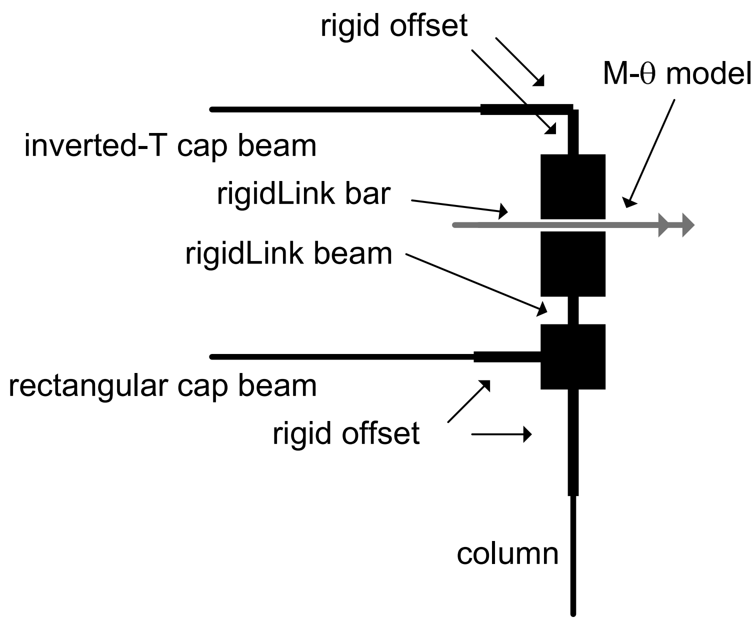

Fig. 3.15 Nodal constraints at the cap beam interface for the 4-span bridge model.

3.3.4 Superstructure

The superstructure consists of prismatic prestressed concrete members that are prestressed in both the longitudinal and transverse directions. Each segment of the superstructure is modeled with a linear elastic beam-column element. No stiffness reduction has been taken for these elements based on common modeling assumptions and the recommendations of the SDC. No reduction of the torsional moment of inertia is taken, since this bridge meets the Ordinary Bridge requirements of the SDC.

3.3.5 Mass Distribution

Point masses are placed along the longitudinal axis of the bridge model. Sources of mass that are modeled include the gravity load of the bridge deck and columns, and additional concrete and lead blocks used for similitude. The mass of the abutment is included in the simulations of the four-span bridge.

3.3.6 Damping

Damping is incorporated into the simulation models using Rayleigh damping with the last committed structural stiffness matrix. The first-mode frequency in the transverse direction for the two-span bridge and the first-mode frequency in the longitudinal direction for the four-span bridge are used to compute the associated stiffness-proportional damping coefficient. A damping ratio of 2% matches the results of system identification studies performed by Ranf (2007).

3.3.7 Pounding

To account for the impact of the bridge deck with the abutments, zero-length elements are included at the ends of the bridge. A study performed by Muthukumar (2003) showed the limitations of existing impact models and introduced a nonlinear Hertz contact model. The Hertz contact is approximated using a bilinear spring including a gap for ease of implementation in existing finite element software. Further studies including this impact model were performed by Nielson (Nielson, 2005) in the seismic fragility analysis of highway bridges. The energy dissipated during impact is:

$$\Delta E = \frac{K_h \delta_m^{n+1} \left(1 - e^2\right)}{n+1} \tag{3.13}$$

where K_h is the impact stiffness factor, δ_m is the amount of penetration, n is the the exponent for the nonlinear Hertz model, and e is the coefficient of restitution. The effective stiffness of the impact model is:

$$K_{eff} = K_h \sqrt{\delta_m} \tag{3.14}$$

The impact stiffness factor, K_h, is computed as $0.5 E_c A_{deck}/L_{bridge}$, to account for the fact that two impact elements are included at each end of the bridge. The maximum penetration, δ_m, is consistent with the assumed value by Muthukumar (2003). The yield penetration during impact is:

$$\delta_y = a \delta_m \tag{3.15}$$

where a must satisfy the relation:

$$a < 1 - \frac{2}{5}(1 - e^2) \tag{3.16}$$

The initial stiffness and post-yield stiffness of the Hysteretic model may then be derived to give the energy dissipation during impact, ΔE, shown in Equation 3.13. The initial stiffness, K_{t_1}, of the impact model is:

$$K_{t_1} = K_{eff} + \frac{\Delta E}{a\delta_m^2} \tag{3.17}$$

The post-yield stiffness, K_{t_2}, of the impact model is:

$$K_{t_2} = K_{eff} - \frac{\Delta E}{(1-a)\delta_m^2} \tag{3.18}$$

The selected impact model parameters are shown in Table 3.6. The hysteretic response of the impact model during a pounding event is shown in Figure 3.16. Initial gap sizes were selected using the measured relative displacements at the east and west side of each respective end of the bridge during Test 4D as shown in Figure 3.17.

Table 3.6 Impact model parameters.

K_{t_1}	4715 kip-in	e	0.8
K_{t_2}	1623 kip-in	a	0.1
K_h	2452 kip-in	n	1.5
δ_m	0.62 in.		

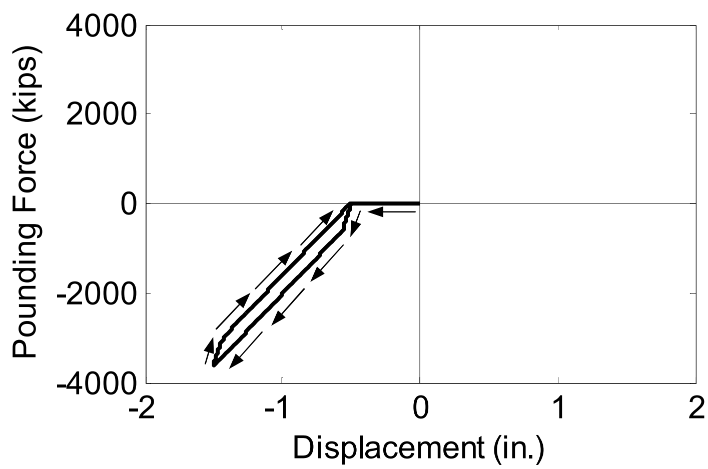

Fig. 3.16 Hysteretic behavior of impact model for pounding at abutments.

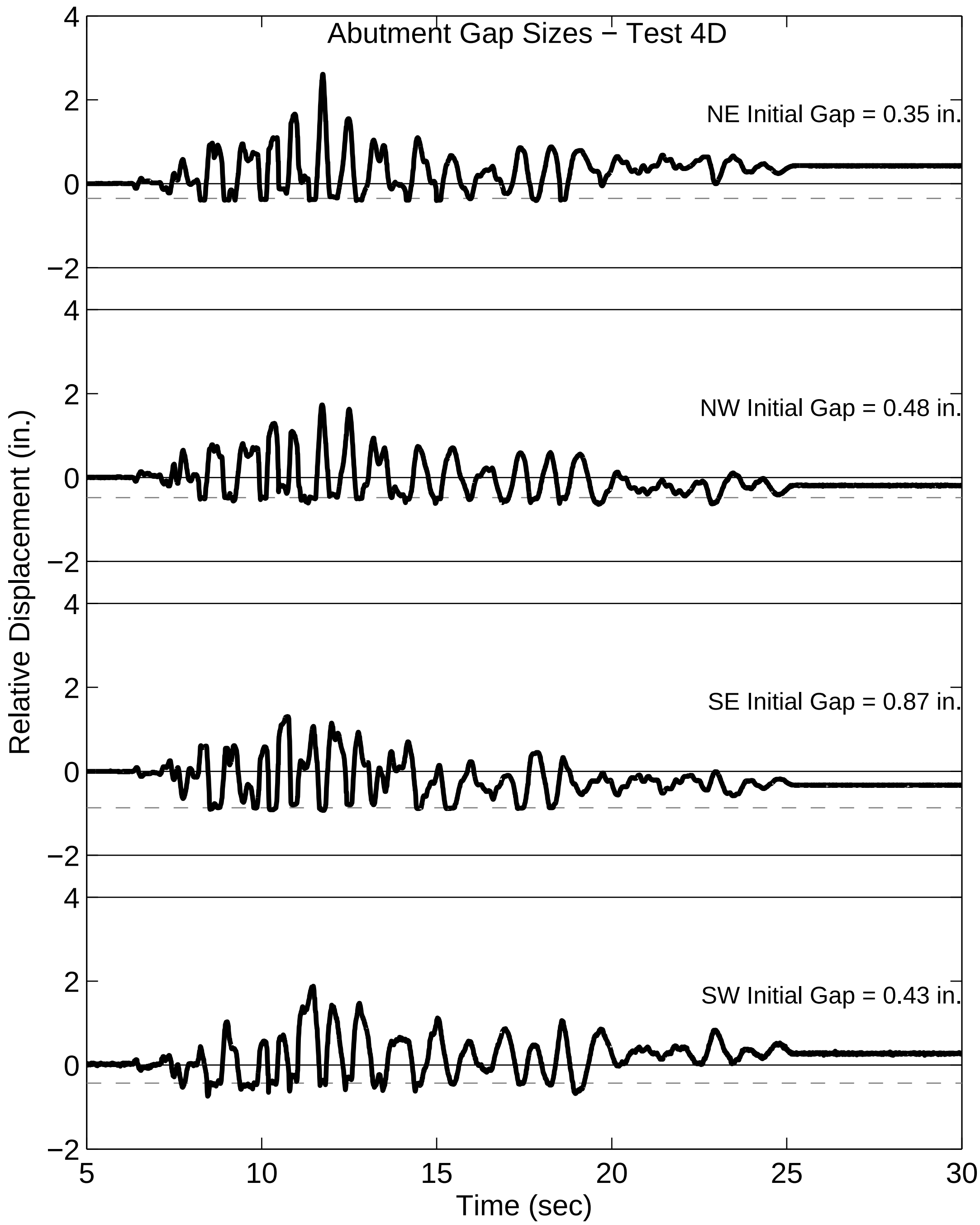

Fig. 3.17 Relative displacements at abutments at the north and south ends of the 4-span bridge during Test 4D.

3.4 DEVELOPMENT OF A CALIBRATED SIMULATION MODEL

The shaking table tests provide an opportunity to calibrate a simulation model to the global response observed at the experimental scale. Following the calibration, the performance of the bridge at the local level, as represented by the model, may be investigated. The Calibrated simulation model also sets a benchmark to which other simulation models using different modeling assumptions for the concrete columns may be compared. Finally, using the laws of similitude, this Calibrated simulation model may be scaled to study the earthquake response of prototype bridge systems.

The simulation model is calibrated to agree with the displacement time histories recorded at the top of each bridge bent during the shaking table tests of the two-span bridge. Two tests are used in the calibration procedure, Test 12 where the response can be considered to be elastic (low level), and Test 15 where the structure behaves nonlinearly (high level). Nonlinear dynamic analyses are conducted using only the table motions for the particular test under consideration. Modeling parameters are judiciously chosen to be varied during the calibration procedure and an evaluation metric is selected to compare the simulation results to those of the shaking table tests.

3.4.1 Selection of Parameters

Based on the data from the experimental tests, there was uncertainty regarding the extent of cracking in the cap beam and the amount of rotation at the column ends due to the strain penetration along the anchored reinforcement. The calibration process involved sensitivity studies with variation in parameters associated with the cap beam bending stiffness and the bar-slip model. For the low-level test, it is necessary to match the elastic period of the structure to capture the response accurately. The parameters necessary for inclusion in the calibration procedure to match the fundamental period are:

1. The reduction factor, γ, applied to the initial stiffness, K_{init}, of the moment-rotation model used to represent bar slip at the column ends.
2. The reduction factor, α, applied to the gross stiffness of the cap beam when modeling this member as a linear-elastic element.

For the high-level test, the sensitivity of the model to variation in the parameters associated with the bar-slip model was investigated. These parameters were selected as:

1. The variation of the unloading stiffness of the bar-slip model with increase in ductility as denoted by the parameter β.
2. The pinching factor of the bar-slip model.

3.4.2 Evaluation Metric

An evaluation metric was selected to assess the sensitivity of the simulation model to variations in the parameters selected for inclusion in the calibration procedure. The metric measures the agreement between the displacement time histories in the simulation and those in the experiment for a complete time history response. To avoid problems associated with a constant time shift as shown in Figure 3.18, the metric is evaluated with comparisons made in the frequency domain, as developed by McVerry (1980):

$$E = \frac{\sum_{i=1}^{N} \sum_{l=l_{min}}^{l=l_{max}} \left|A^i{}_{exp}(l\Delta\omega) - A^i{}_{sim}(l\Delta\omega)\right|^2}{\sum_{i=1}^{N} \sum_{l=l_{min}}^{l=l_{max}} \left|A^i{}_{exp}(l\Delta\omega)\right|^2} \tag{3.19}$$

where $A^i{}_{exp}$ and $A^i{}_{sim}$ are the Fourier amplitudes of the displacement time histories at bent i for the experiment and the simulation, respectively; N is the number of bents, l_{min} and l_{max} determine the frequency range over which the metric is calculated, and $\Delta\omega = 2\pi/T$, where T is the final time for the test under consideration. The evaluation metric is a measure of the summation of the mean square error of the simulation response divided by the summation of the mean square of the experimental response for the Fourier transforms of the displacement time histories at the three bents. An illustration of a comparison of the Fourier transform of the displacement time histories is shown in Figure 3.18.

3.4.3 Parameter Study

Nonlinear dynamic analyses of the simulation model were performed using the table motions for Test 12. This test was selected because yielding of the reinforcement had not yet occurred in the test specimen, and the objective for the sensitivity studies associated with the low-level test was to match the elastic response seen in the experiment. The simulation model included only the effects of damage from the table motions associated with Test 12, while the experimental results

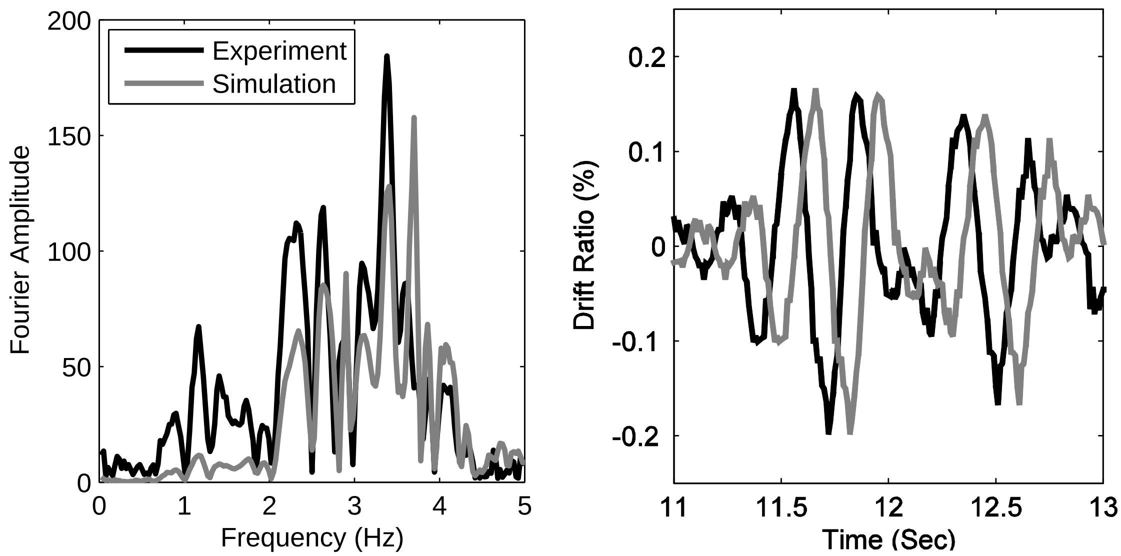

Fig. 3.18 Comparison of the Fourier amplitudes of the displacements of the 2-span bridge at bent 3 during Test 12 used in calculating the evaluation metric and an example of a constant time shift in a displacement time history.

included damage from all of the low-level tests prior to and including Test 12. This difference was accepted to reduce the computational time for the sensitivity studies and to investigate a wide range of parameters. As was discussed in Section 3.4.1, the parameters varied during the calibration for the low-level test were γ, the reduction factor applied to the initial stiffness of the bar slip model, and α, the reduction factor applied to the cap beam bending stiffness. These two parameters were identified as having the most significant impact on the elastic period of the model and thus on the low-level response.

Sensitivity studies of the simulation model for the low-level response were performed using the range of parameters given in Table 3.7. For each set of parameters, the metric was calculated using Equation 3.19. The results of the sensitivity studies are shown in Figure 3.19. The calibrated parameters selected based on the results of the sensitivity studies for the low-level tests are shown in Table 3.7.

Table 3.7 Parameters for low-level calibration.

	Range	Calibrated Value
γ	0.6-1.2	0.65
α	0.4-1.0	0.75

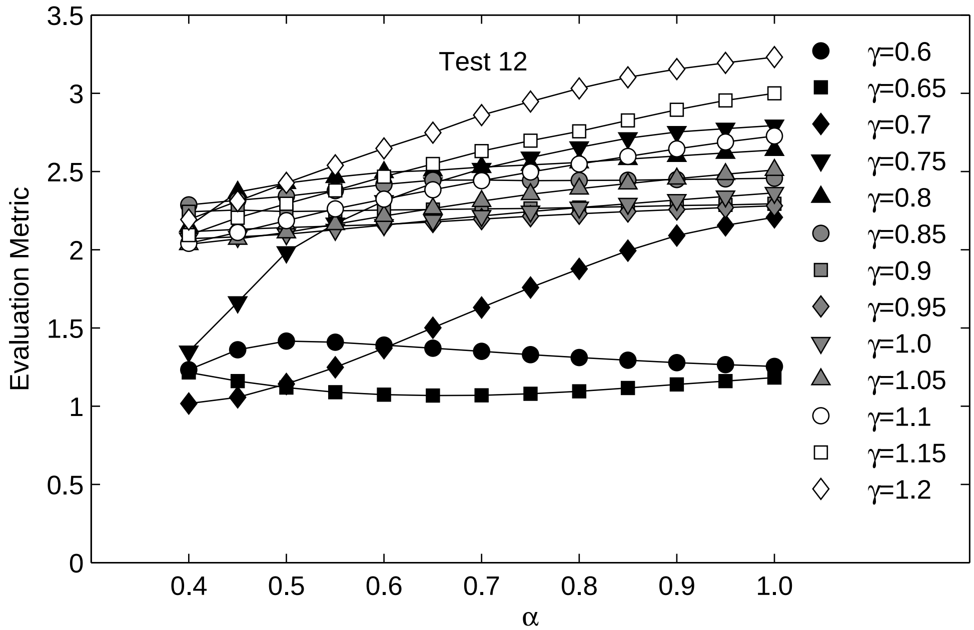

Fig. 3.19 Sensitivity of the evaluation metric during calibration study of the 2-span bridge for Test 12.

The improvement in the representation of the vibration periods of the simulation model as a result of the low-level calibration is shown in Table 3.8 for modes associated with translation in the transverse direction. The vibration periods from the experiment in Table 3.8 were determined based on system identification studies performed by Ranf (2007).

Table 3.8 Vibration periods prior to and following calibration.

	Mode		
	2	3	6
Simulation (Starting Assumptions)	0.30	0.23	0.07
Simulation (After Calibration)	0.33	0.25	0.07
Experiment	0.34	0.26	0.08

The mode shapes and vibration periods for the simulation following the low-level calibration were determined using OpenSees and are shown in Figure 3.20. The first mode includes

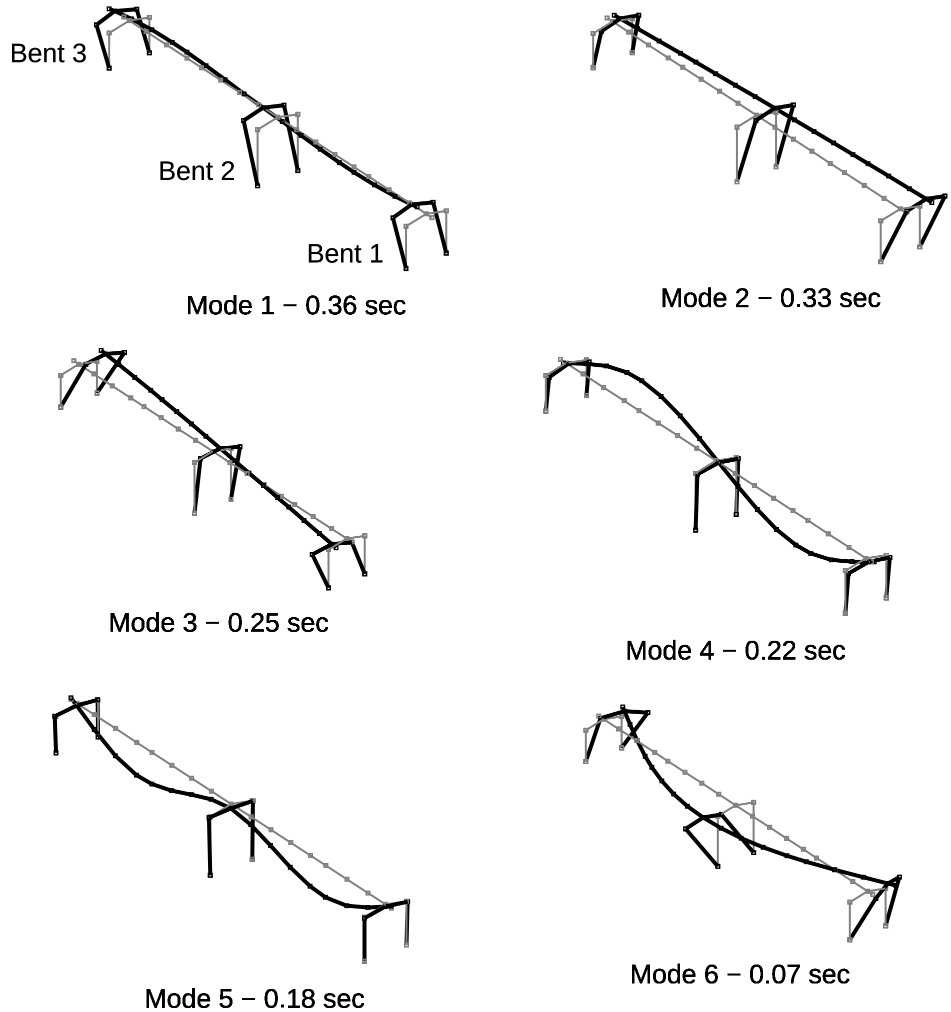

Fig. 3.20 Mode shapes and periods of vibration for the simulation model of the 2-span bridge following low-level calibration.

translation in the longitudinal direction. The second mode includes translation in the transverse direction with rotation about bent 3. Mode 3 is primarily translation in the transverse direction with twisting occurring about bent 2. Modes 4 and 5 are due to in-plane bending of the deck. The sixth mode is out-of-plane bending of the deck in the transverse direction.

Additional parameter studies were performed to calibrate the simulation model to the results from a test where significant nonlinear deformation occurred. Test 15, for which drift ratios greater than 2% at bents 1 and 3 were observed, was selected for the comparison to a high-level test. Sensitivity studies of the simulation model for the high-level response were performed using the range of parameters for the bar-slip model given in Table 3.9.

Table 3.9 Range of parameters for high-level calibration.

	Parameter Range
β	0.0-0.5
pinching factor	0.0-0.75

The simulation model included only the effects of damage from the table motions associated with Test 15, while the experimental results included damage from all of the low-level tests prior to and including Test 15. As was the case for the low-level calibration, this limitation was accepted because of the difficulty in modeling accumulated damage over many tests, and to decrease the computation time required for investigating a wide range of parameters. The results of sensitivity studies for different assumptions regarding the bar slip model are shown in Figure 3.21. The default values of 0.0 for the parameters, β and the pinching factor, for the bar slip model were selected to satisfy the minimum evaluation metric calculated during the calibration study. The cyclic response of the bar slip model prior to and following the low-level and high-level calibration is shown in Figure 3.22.

Further comparisons in Figure 3.23 illustrate the difference in the displacement time histories and moment-rotation response for different values of the evaluation metric. Increased pinching in the moment-rotation model leads to a poorer comparison between the experimental and simulation displacement histories. To determine the effect of extensive nonlinear deformation on the value of the evaluation metric for different assumptions in the bar slip model, additional analyses were conducted using the recorded table motions during Test 18. For the same selected set of parameters for the bar slip model, Figure 3.24 demonstrates that the same trend in the value of the evaluation metric is observed with increased pinching of the moment-rotation model in the simulations for both Tests 15 and 18. In the following section, the performance of the simulation model developed from the calibration procedure described above is assessed for the response to all table motions recorded during the shaking table tests.

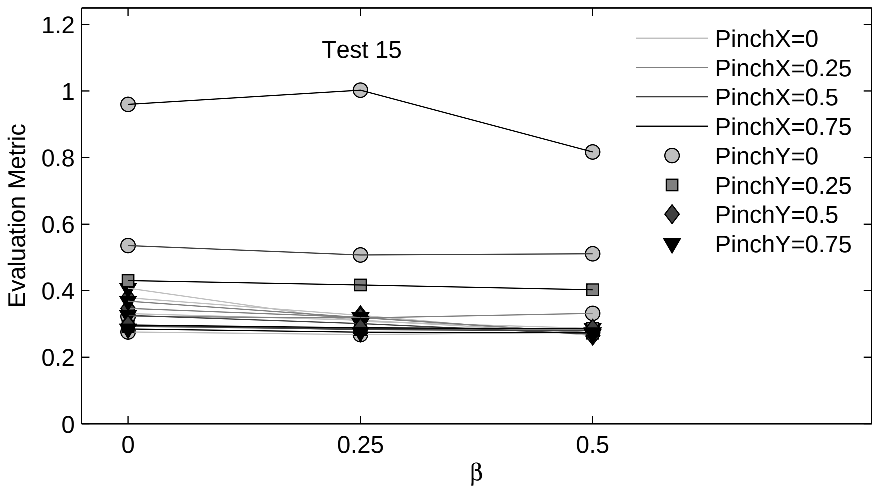

Fig. 3.21 Sensitivity of the evaluation metric during calibration study of the 2-span bridge for Test 15.

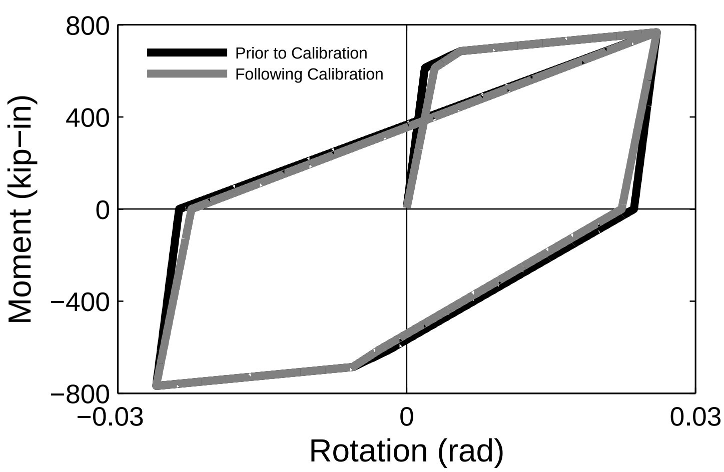

Fig. 3.22 Moment-rotation model for bar slip after calibration.

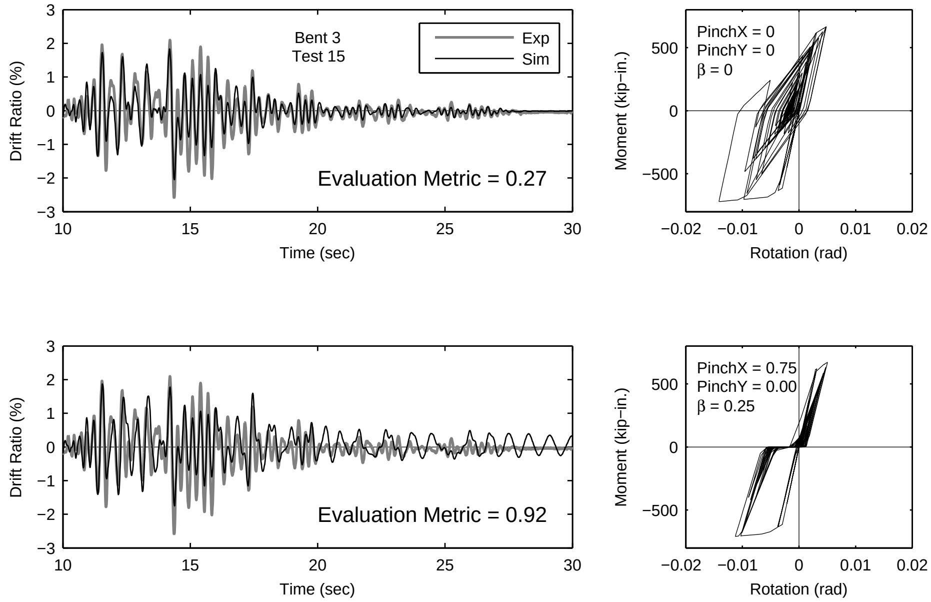

Fig. 3.23 Results of calibration study of the 2-span bridge for Test 15. Moment-rotation response from the simulation model is shown at the bottom of the west column in bent 3.

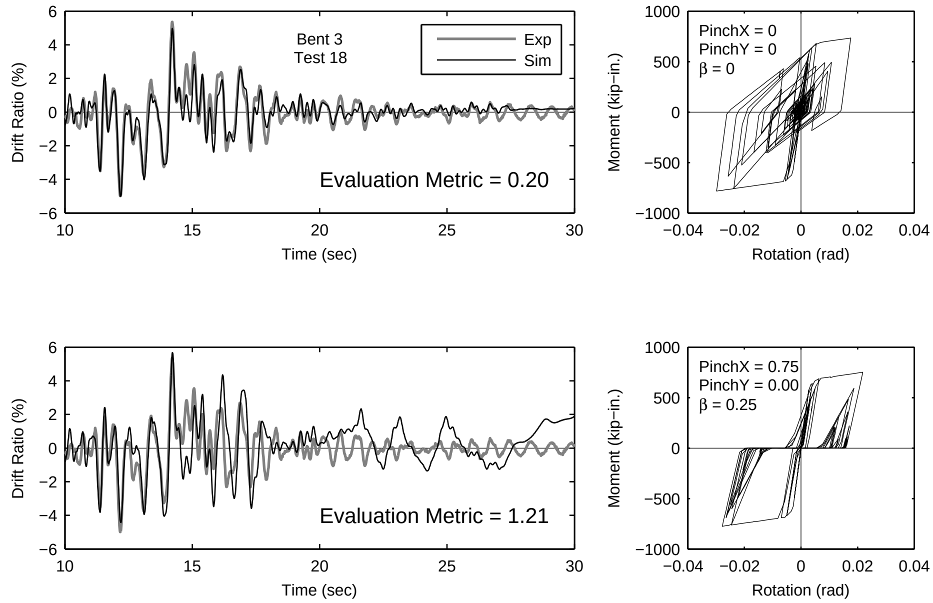

Fig. 3.24 Results of calibration study of the 2-span bridge for Test 18. Moment-rotation response from the simulation model is shown at the bottom of the west column in bent 3.

3.5 VALIDATION OF SIMULATION MODELS

3.5.1 Two-Span Bridge

Nonlinear dynamic analyses of the shaking table specimen were performed using simulations with the different column models described in Section 3.3.2. The excitation was applied using the multiple support pattern with the measured table displacements. These simulations provide insight into the accuracy of the Calibrated model, described in Section 3.4, when the accumulated damage from all of the shaking table tests is considered. The results from the Calibrated model may also be used as a benchmark to assess the extent to which the two other simulation models being considered are capable of capturing the response measured during the shaking table tests.

Comparisons of the global response of the simulation model are made using periods of vibration, the evaluation metric proposed in Section 3.4, and relative displacement time histories measured at the top of each bridge bent and the table supporting it. Table 3.10 shows the vibration periods calculated from modal analysis of each simulation model. The Priestley (Priestley et al., 1996) and Berry (Berry et al., 2008) models underestimate the period of vibration at the second mode by 21% and 12%, respectively. A comparison of the displacement time history response during Test 12 at bent 3 for the different simulation models is shown in Figure 3.25. While the Berry model gives closer agreement to the periods of vibration identified during the two-span tests listed in Table 3.10, a larger evaluation metric is computed for the displacement time history response of this model than for the Priestley model. The agreement of the low-level response, where yielding has not yet occurred, of the simulation models is very sensitive to any difference of the periods of vibration compared with the experimental specimen.

Table 3.10 Comparison of periods of vibration (in sec) for the 2-span bridge models.

	Mode					
Simulation	1	2	3	4	5	6
L_p Priestley (Priestley et al., 1996)	0.32	0.27	0.19	0.22	0.17	0.07
L_p Berry (Berry et al., 2008)	0.35	0.30	0.23	0.22	0.18	0.07
Calibrated	0.36	0.33	0.25	0.22	0.18	0.07
Experiment		0.34	0.26			0.08

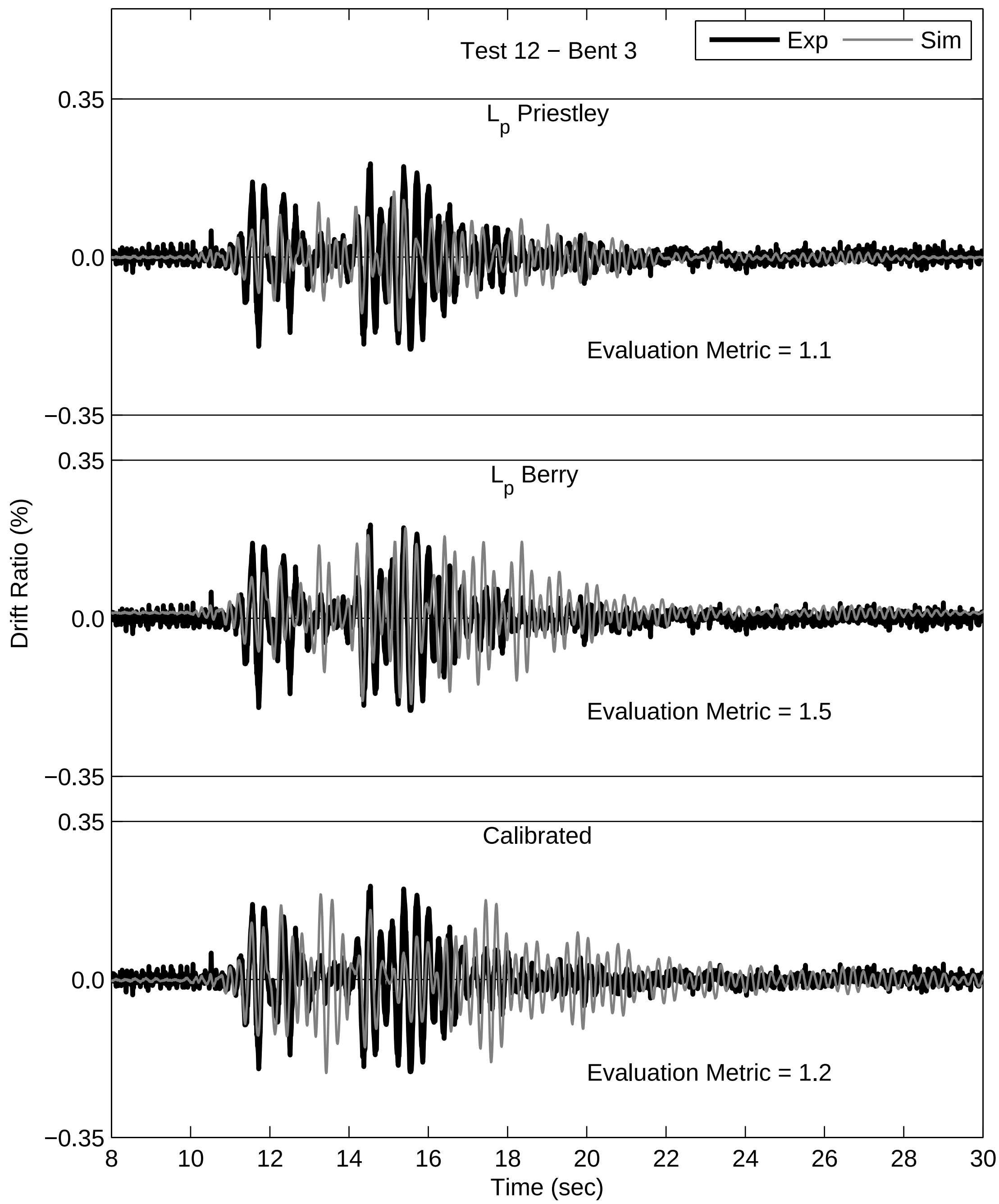

Fig. 3.25 Comparison of displacement time histories of the 2-span bridge during Test 12 when using different column models in the simulations.

Additional comparisons of the displacement time history response of the simulations considered for Tests 15 and 18 are shown in Figures 3.26 and 3.27, respectively. For these higher-level tests where significant nonlinear deformation occurs, there is much less discrepancy between the results of each simulation model. The frequency content, which proved to be very sensitive to modeling assumptions for the low-level tests, is less sensitive to changes in the modeling assumptions at these higher-level tests.

The peak drift ratios computed using the selected simulation models are shown in Figure 3.28. The simulation models give excellent predictions of the peak drift ratios at each bent beginning with Test 15, where significant yielding has taken place, until Test 18, at the onset of bar buckling in bent 3. For these tests, the simulations match the peak drift ratios within a 20% error. Following Test 18, substantial bar buckling and fracture of the longitudinal and transverse reinforcement took place. The simulation models do not account for such phenomena and thus cannot track the displacement time histories during these final tests.

A comparison of the superstructure displacements at the instants when the peak response of bent 3 is reached during Test 18 is shown in Figure 3.29. The superstructure displacement profile at these instants gives insight into the ability of the simulation models to capture the displacements during the shaking table tests. For the first instant shown, the measured response displays greater twisting about bent 2 than do the simulation models, resulting in a greater absolute displacement at bent 3. At the second instant shown, the deck displacement at bent 3 from each of the simulations is in close agreement with that of the measured response; however, the different amounts of twist result in either an overestimate or underestimate of the response at bent 1 depending on the selected column model. To predict the system response of this bridge with varying column heights, it is necessary to reproduce accurately the twisting response noted during the shaking table tests. The validated simulation models demonstrate the ability to predict the peak global response within an acceptable accuracy despite the twisting effect not being fully represented.

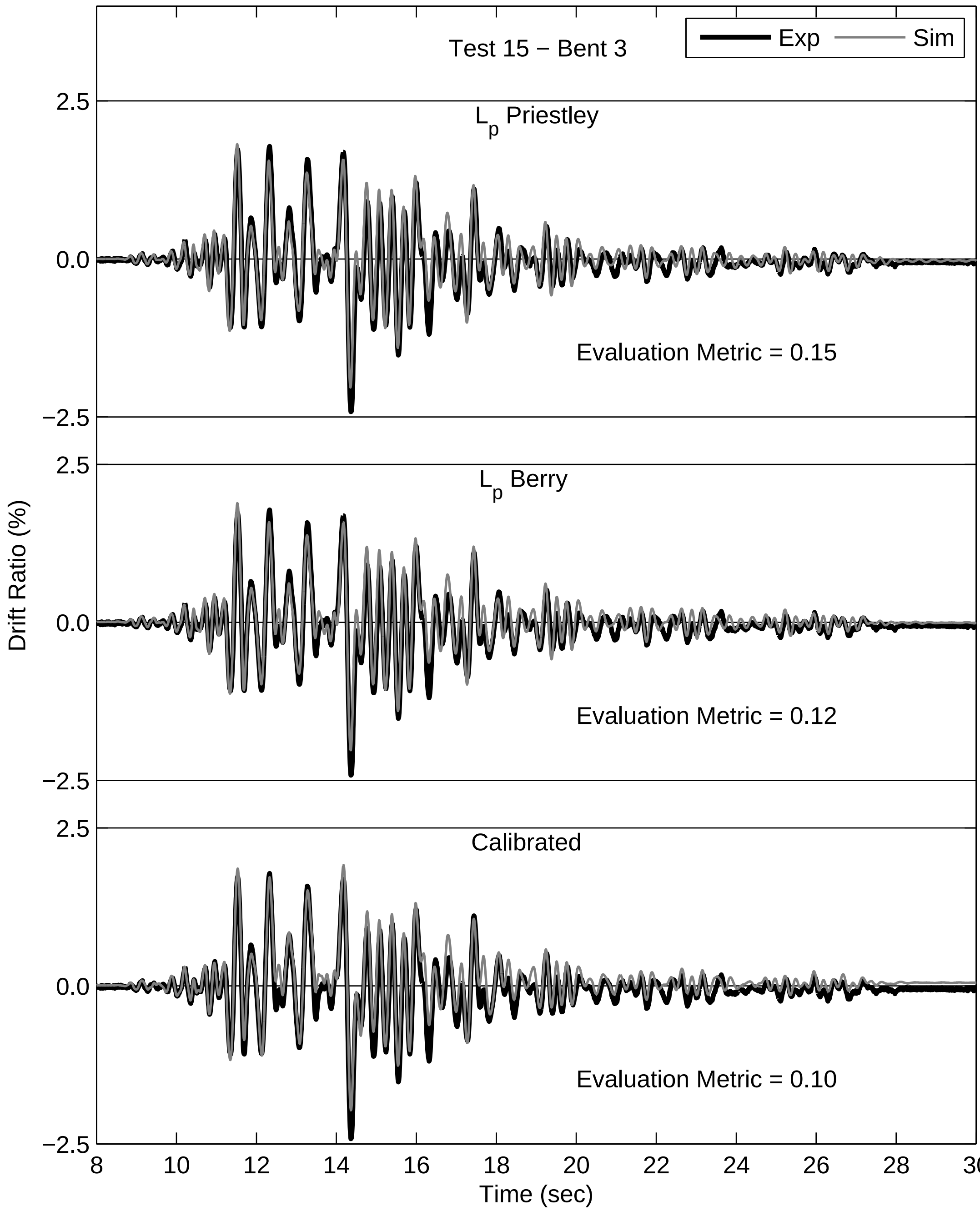

Fig. 3.26 Comparison of displacement time histories of the 2-span bridge during Test 15 when using different column models in the simulations.

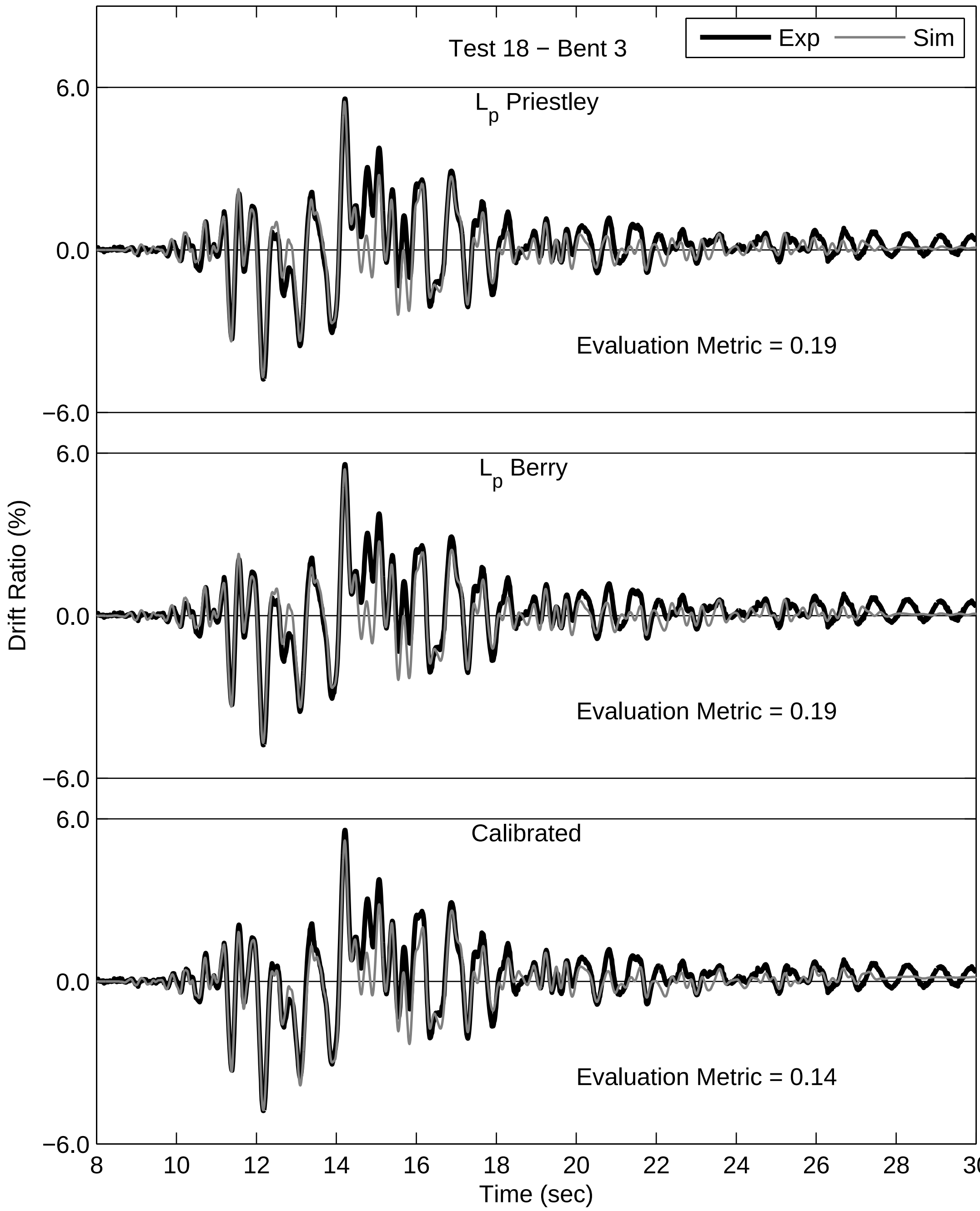

Fig. 3.27 Comparison of displacement time histories of the 2-span bridge during Test 18 when using different column models in the simulations.

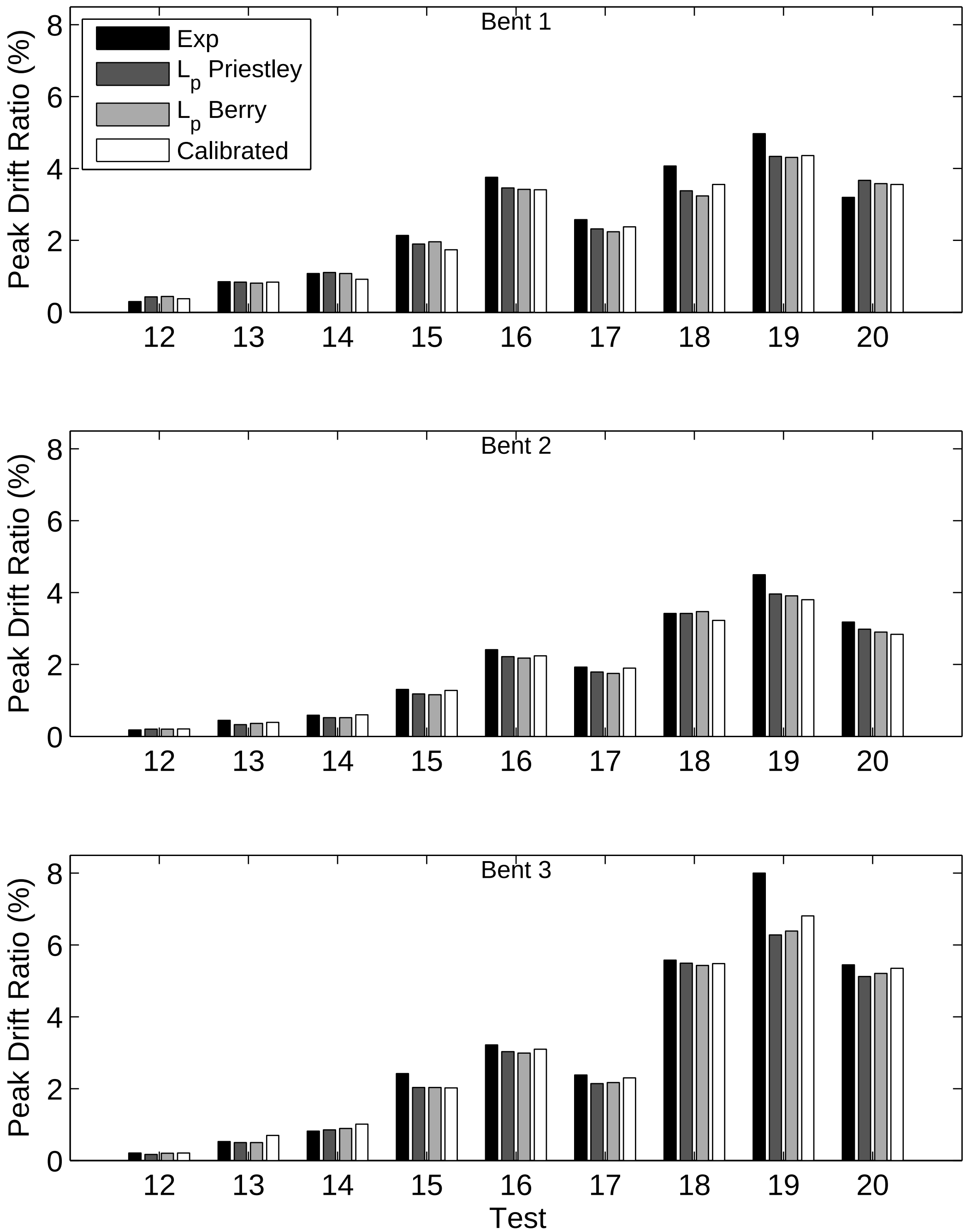

Fig. 3.28 Comparison of peak drift ratios of the 2-span bridge when using different column models in the simulations.

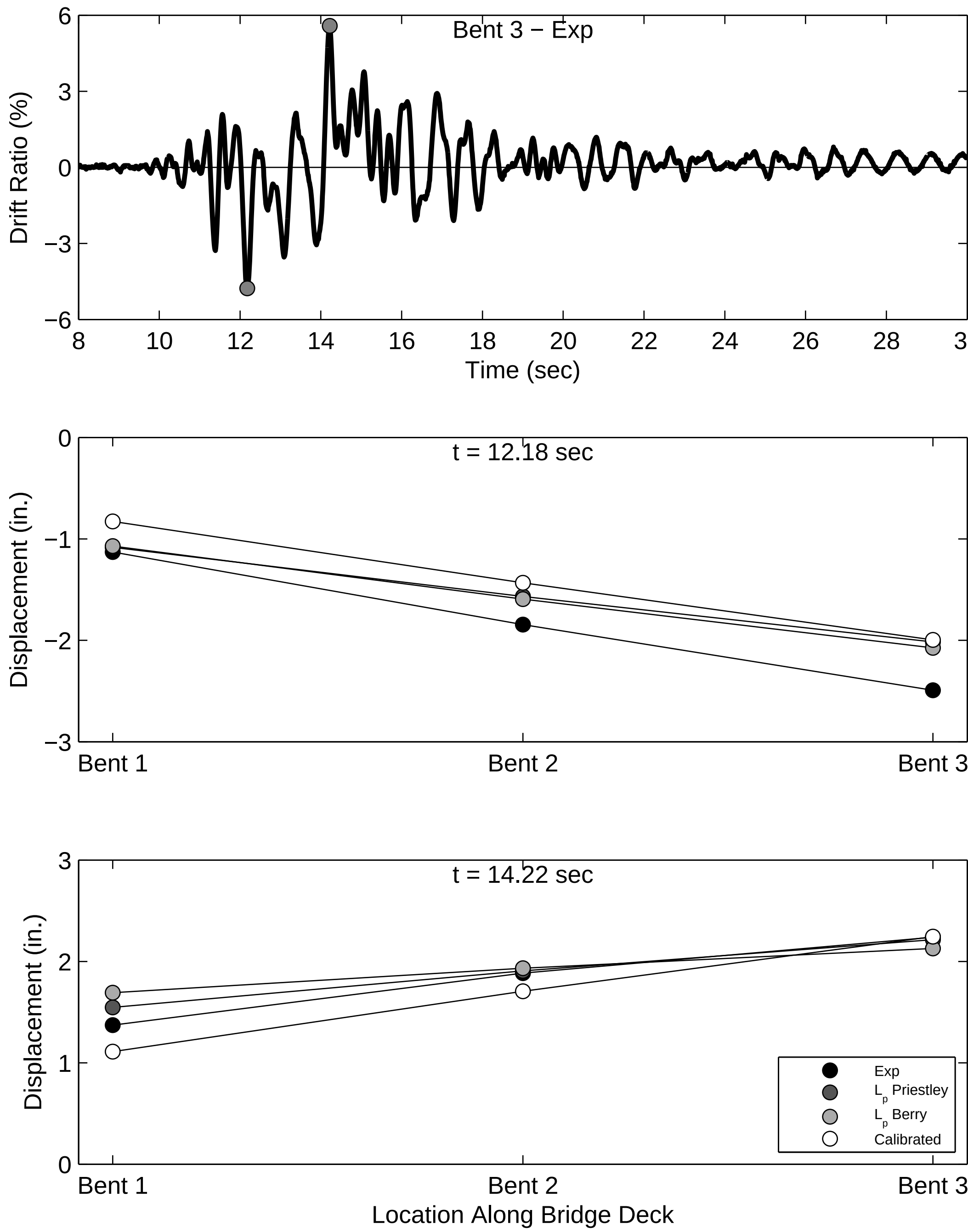

Fig. 3.29 Comparison of superstructure displacements of the 2-span bridge at peak displacements during Test 18 when using different column models in the simulations.

The comparisons of the local response of the simulation models with that of the experiment are also of interest, since these response quantities are associated with limit states in performance-based earthquake engineering methodologies. The columns of the two-span bridge were instrumented with displacement transducers along the height of the column as shown in Figure A.2. Using these measurements, the average curvatures at the column ends during the tests are:

$$\phi_{avg}^{exp} = \frac{d_2 - d_1}{l_{gauge} h_{gauge}} \tag{3.20}$$

where d_2 and d_1 are the measured displacements, l_{gauge} is the distance of 19 in. between the displacement transducers, and h_{gauge} is the distance of 5 in. over which the average curvature is taken. It is important to note that the average curvature determined from the experiment includes the effect of the additional rotation of the column due to strain penetration along the anchored reinforcement. To compare with this measured quantity, the local responses from the Calibrated simulation model must be adjusted as follows:

$$\phi_{avg}^{Calibrated} = \phi^{bc} + \frac{\theta^{barslip}}{h_{gauge}} \tag{3.21}$$

where ϕ^{bc} is the curvature computed from the force beam-column element; and $\theta^{barslip}$ is the rotation from the zero-length element at the column ends. The curvature computed from the simulation models with the beamWithHinges element is not modified, since this element does not differentiate between the local behavior due to material response of the steel and strain penetration along the anchored reinforcement.

The peak curvature ductility measured at the bottom of each column is shown in Figure 3.30. According to ATC-32 (1996), well-detailed bridge columns must have sufficient transverse reinforcement to ensure a dependable section curvature ductility capacity of at least 13. The expected curvature ductility capacity may be much larger, on the order of 20. The bridge performed well when subjected to significant ground motions, including Test 18 where longitudinal reinforcement was at the onset of buckling and curvature ductilities were greater than 20 in bent 3. A comparison of the peak curvatures from the experiment and the simulation models is shown in Figure 3.31. Although the experimental response is averaged and does not measure the peak curvature at the column end as discussed in Section 3.3.2, this measurement does include the additional curvature due to strain penetration along the anchored reinforcement and thus contains inherent conservatism when used as a means for comparison. The Priestley model demonstrates excellent agreement within 7% of the measured response for curvature ductilities exceeding 20 in bent 3 during Test 18. For the high-level tests considered, 15−18, the Priestley model also produces agreement within 22% for the average curvatures at bents 1 and 3. The Berry model, which has smaller fixed plastic hinge lengths, consistently overestimates the curvature by as much as 43% in bent 3 during Test 18. The Calibrated model predicts curvatures due to the material response alone that are up to 30% less than the measured response at bents 1 and 3 during Test 18.

Due to the fact that the analyst typically computes curvatures from material response alone, these latter two models do not accurately estimate the local response at levels of nonlinear deformation approaching failure. The beamWithHinges element with fixed plastic hinge lengths defined by the Priestley relationship is the recommended model in light of the performance of the models considered when predicting the response of the two-span bridge during the shaking table tests.

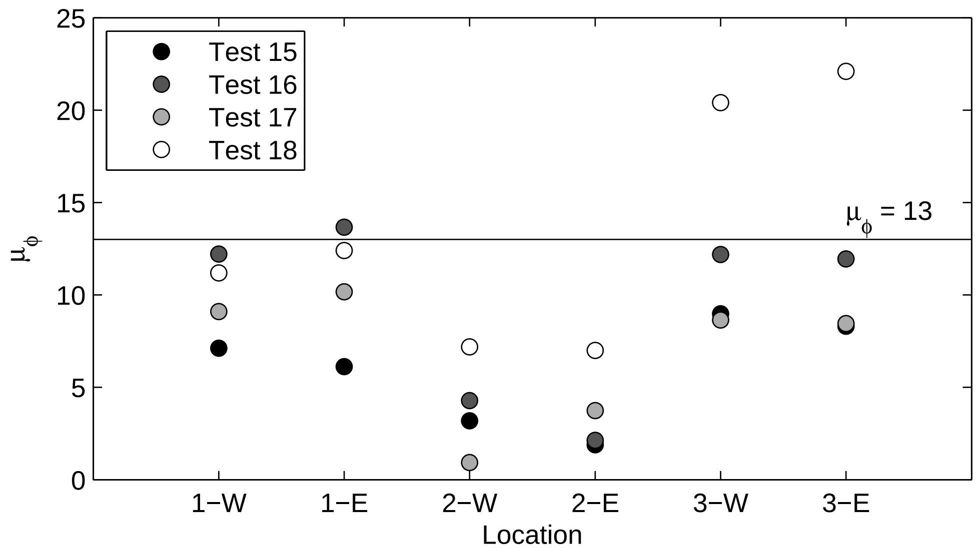

Fig. 3.30 Peak curvature ductilities measured at the bottom of each column of the 2-span bridge.

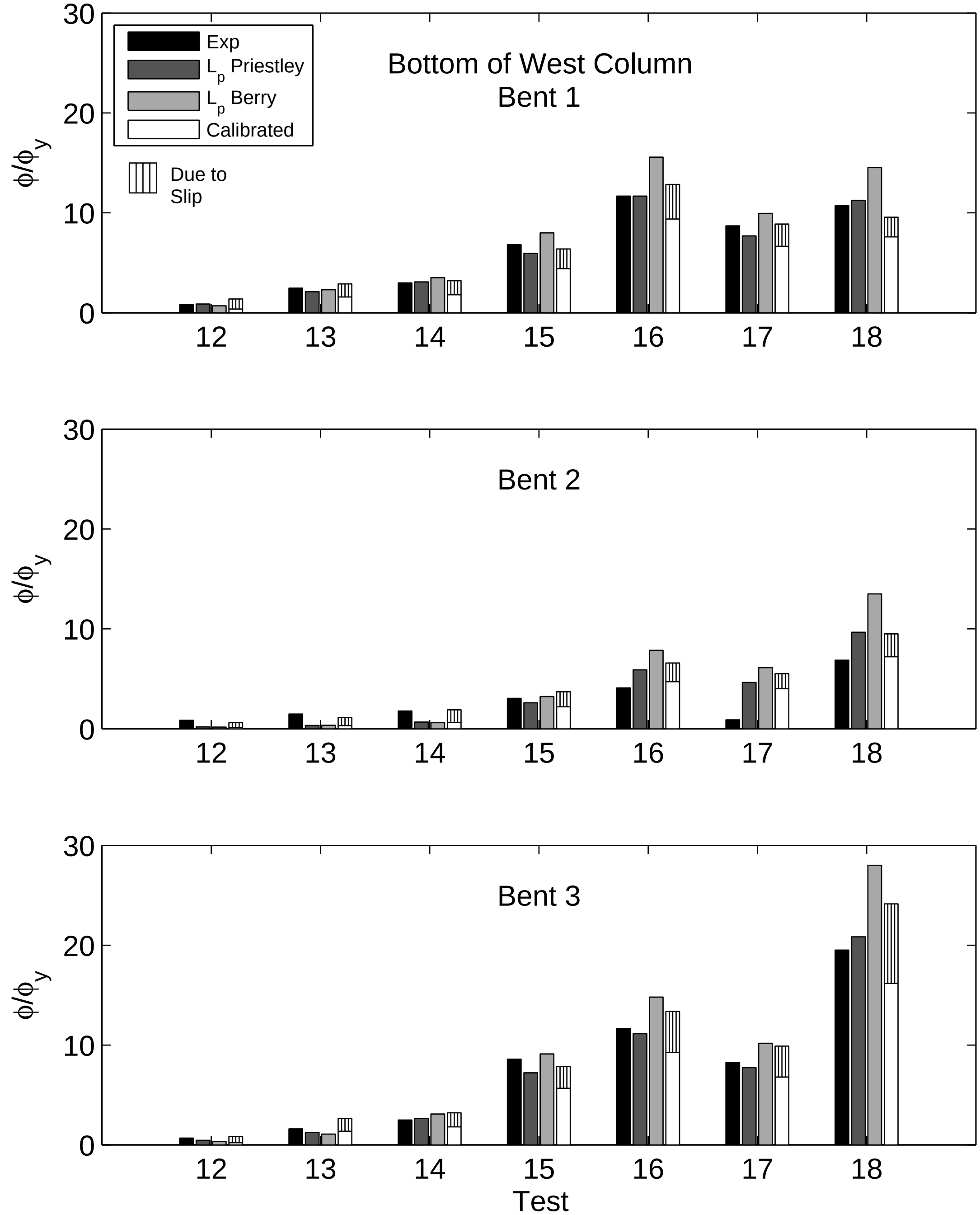

Fig. 3.31 Comparison of peak curvatures of the 2-span bridge when using different column models in the simulations.

3.5.2 Four-Span Bridge

Additional validation studies were performed for the four-span bridge by comparing the results of finite element simulations to the measured response. The nonlinear dynamic analyses in OpenSees included Tests 4D−7 from the test protocol listed in Table A.3. Only the final four high-level tests were considered in the simulations, since Test 4D was the first test with table motions applied in both horizontal directions for which no bridge restrainers were present. The simulation of the response of the four-span bridge during Tests 4D−7 presents significant modeling challenges and the following limitations must be addressed when assessing the results.

1. Both conventional and shape memory alloy (SMA) bridge restrainers were used at the abutments during Tests 1B, 4A, and 4B, thus modifying the bridge response considerably. Since the response of these restrainers was outside the scope of this simulation effort, no consideration has been given to the accumulation of damage in the bridge prior to Test 4D.
2. The actuators delivering the imposed displacement at the abutments had a maximum load capacity of 110 kips. The contact model considered is not restricted to this maximum value nor does it account for any fluid-structure interaction that occurs between the compliant hydraulic system of the actuator and the bridge during pounding events.
3. The abutment sliding system does not have sufficient restraint to prevent rotation of the abutment during pounding events.
4. The gap between the bridge deck and the abutment was not measured in between each test. The measured relative displacement at these locations fluctuates during pounding events rather than consistently returning to zero. As a result, interpretation of the initial gap size prior to each test from the measured relative displacement is less precise.
5. Friction develops during pounding events where the bridge deck is in contact with the abutment for a finite period of time. No allowance for the modification of the translation of the bridge in the transverse direction due to friction during pounding has been made in the simulation.
6. Square-wave and snap-back tests were not performed to give a more direct measurement of the flexibility at the cap beam interface for each bridge bent.

The measured table displacements as well as the measured absolute displacements at both ends of each abutment were applied using the multiple support pattern in OpenSees as shown in Figure 3.32. Initial gap sizes at the abutment ends and the pounding model were selected as discussed in Section 3.3.7. The nodal restraints for the input excitation at the abutments are shown in Figure 3.33. At the locations where the abutment displacements are imposed, the nodes are restrained to move only in the longitudinal direction. The node at the end of the bridge deck is restrained from translating in the vertical direction as well as rotating about the longitudinal axis.

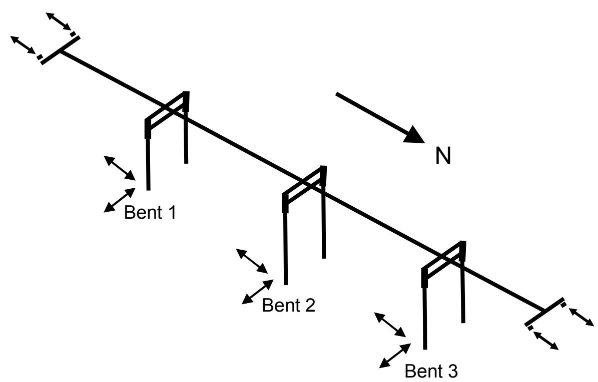

Fig. 3.32 Location of input excitation for the 4-span bridge model.

Three different simulation models were considered in the validation studies. All columns in the simulation are modeled using a beamWithHinges element with a fixed plastic hinge length computed from the Priestley relationship and an effective flexural stiffness determined from a moment-curvature analysis. The parameter varied during the study is the rotational flexibility at the top of the cap beam discussed in Section 3.3.3. The models are identified as NoRelease, Calibrated, and WithRelease to correspond to the moment-rotation model for rotation about the transverse axis at the top of the cap beam. The NoRelease model includes no rotational flexibility at the cap beam interface. The Calibrated model has a moment-rotation model such that the first-mode frequency of the bridge matches that found from system identification of low-level tests as discussed in Section 3.2.2. To calibrate the moment-rotation model, an optimization procedure in Matlab, fminsearch, minimizes the square of the error of the first-mode period divided by the square of the first-mode period determined from the system identification. The optimization procedure reaches the minimum by using the downhill simplex method (Nelder and Mead, 1965). The

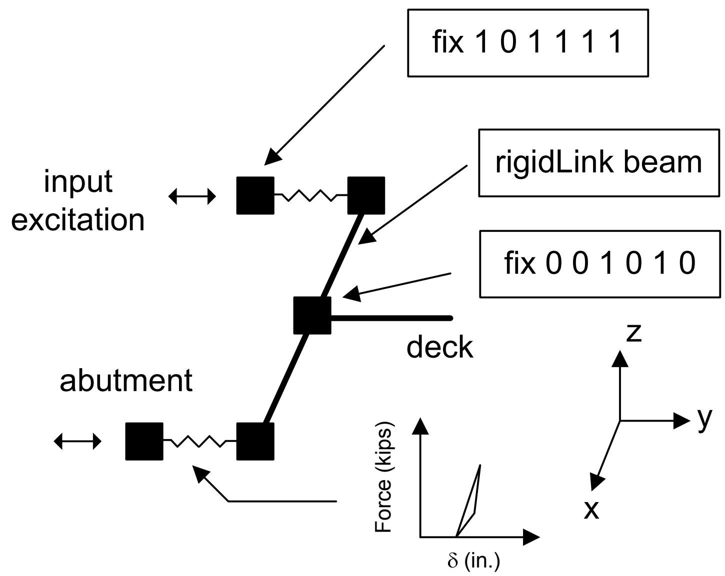

Fig. 3.33 Nodal restraints and modeling of impact at the abutments for the 4-span bridge model.

WithRelease model uses a moment release for rotation about the transverse axis at the cap beam interface. A comparison of the vibration periods obtained from a modal analysis of each model is given in Table 3.11. The corresponding mode shapes are shown in Figure 3.34. The first mode is translation in the longitudinal direction. The second mode is translation in the transverse direction with rotation about bent 2. Mode 3 is translation in the transverse direction with twisting occurring about bent 3. Modes 4 and 5 are due to in-plane bending of the deck. The sixth mode is translation in the transverse direction due to out-of-plane bending of the deck.

Table 3.11 Comparison of periods of vibration (in sec) for the 4-span bridge models.

	Mode					
Simulation	1	2	3	4	5	6
NoRelease	0.34	0.33	0.25	0.17	0.15	0.16
Calibrated	0.52	0.33	0.25	0.18	0.16	0.15
WithRelease	0.72	0.33	0.25	0.19	0.16	0.15

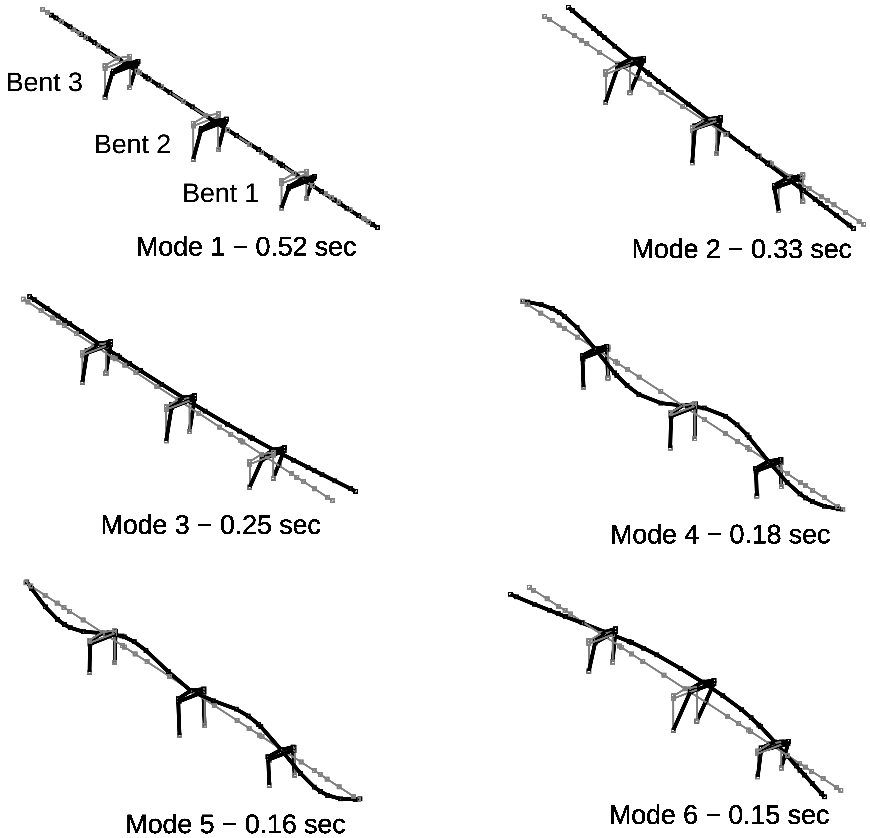

Fig. 3.34 Mode shapes and periods of vibration for the simulation model of the 4-span bridge.

The peak drift ratios in both the transverse and longitudinal directions computed from the simulations are compared to those measured during the experiment in Figures 3.35 and 3.36. At Test 6, spalling has occurred completely around the perimeter of the ends of the columns in bent 1 and the longitudinal bars at these locations are at the onset of buckling. The simulations for Test 6 underestimate the peak drift ratios at bents 1 and 3 by as much as 29%, while overestimating the drift of bent 2 by as much as 67%. In addition to the modeling challenges enumerated earlier, some insight may be gained into this lack of agreement by considering the deck profile at particular instants during Test 6. The deck profile is plotted in Figure 3.37 at the beginning and end of the pounding event prior to the excursion of bent 1 towards the peak drift ratio. As contact between the bridge deck and the abutment occurs at the northeast end of the bridge, the abutment rotates clockwise. The contact over a finite period of time allows for the point of contact to serve as a pivot. When the abutment rotates, it induces a minor rotation of the bridge deck while maintaining a nearly constant drift ratio at bent 1. The deck profile is compared to that from the Calibrated simulation model in Figure 3.38 immediately following the pounding event and also at the instant of the peak drift ratio in bent 1. The bridge deck in the experiment exhibits considerably greater rotation than that seen in the simulation model. This accounts for the larger drift ratios observed at bents 1 and 3 in the experiment than those from the simulations.

The lack of rotation of the bridge deck in the simulations may be attributed to the high-frequency pounding response from the impact model at the abutments. Such response does not allow for a sustained pounding event over a finite period of time during which the abutment may serve as a pivot about which the bridge deck can rotate. For all simulation models, good agreement is achieved between the displacement time history response at bent 1 during Test 6 until the pounding event at 10.85 sec as shown in Figure 3.39. While the sustained pounding event restricts the drift ratio at bent 1 to fluctuate very little in the experiment, the simulation models all recoil to large drift ratios in the opposite direction between 10.85 sec and 11 sec. Following this large excursion, the simulation models no longer accurately track the time history response at bent 1, including the residual drift ratio measured at the end of the test.

The simulations give excellent predictions of the peak drift ratios in the longitudinal direction within 17% of the measured response at all bents during Test 6. The displacement time histories in the longitudinal direction during Test 6 are compared in Figure 3.40. High-frequency vibrations are present in the simulations during pounding events and may be observed more readily by comparing the relative displacement time histories at the northeast side of the bridge as shown in Figure 3.41. Although the simulation models do introduce hysteretic damping during pounding at the abutments as shown in Figure 3.42, there is greater damping observed during the experiment of which a major contribution may be postulated as stemming from the fluid-structure interaction with the hydraulic systems of the actuators.

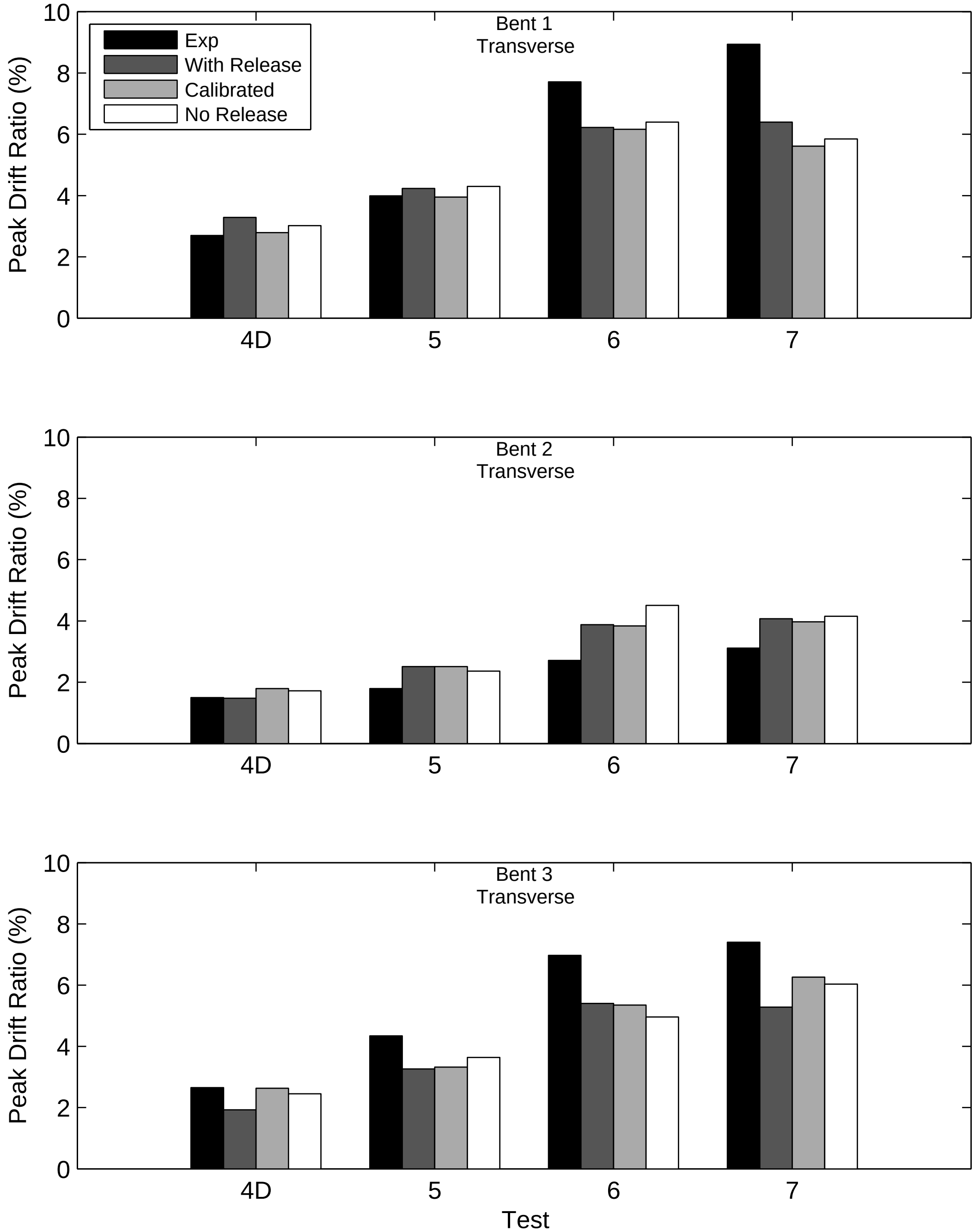

Fig. 3.35 Comparison of drift ratios in the transverse direction of the 4-span bridge when using different assumptions for the flexibility at the top of the cap beam.

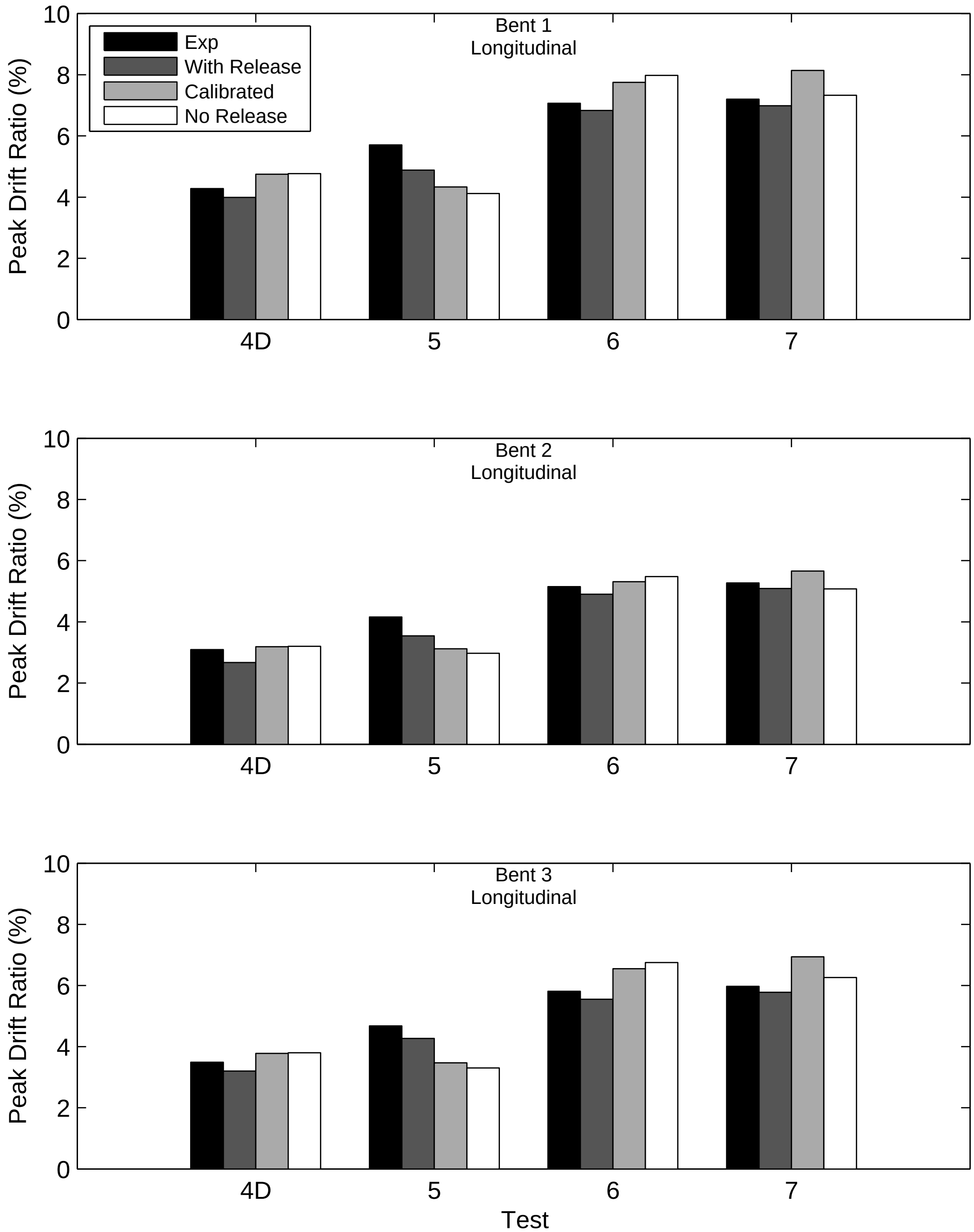

Fig. 3.36 Comparison of drift ratios in the longitudinal direction of the 4-span bridge when using different assumptions for the flexibility at the top of the cap beam.

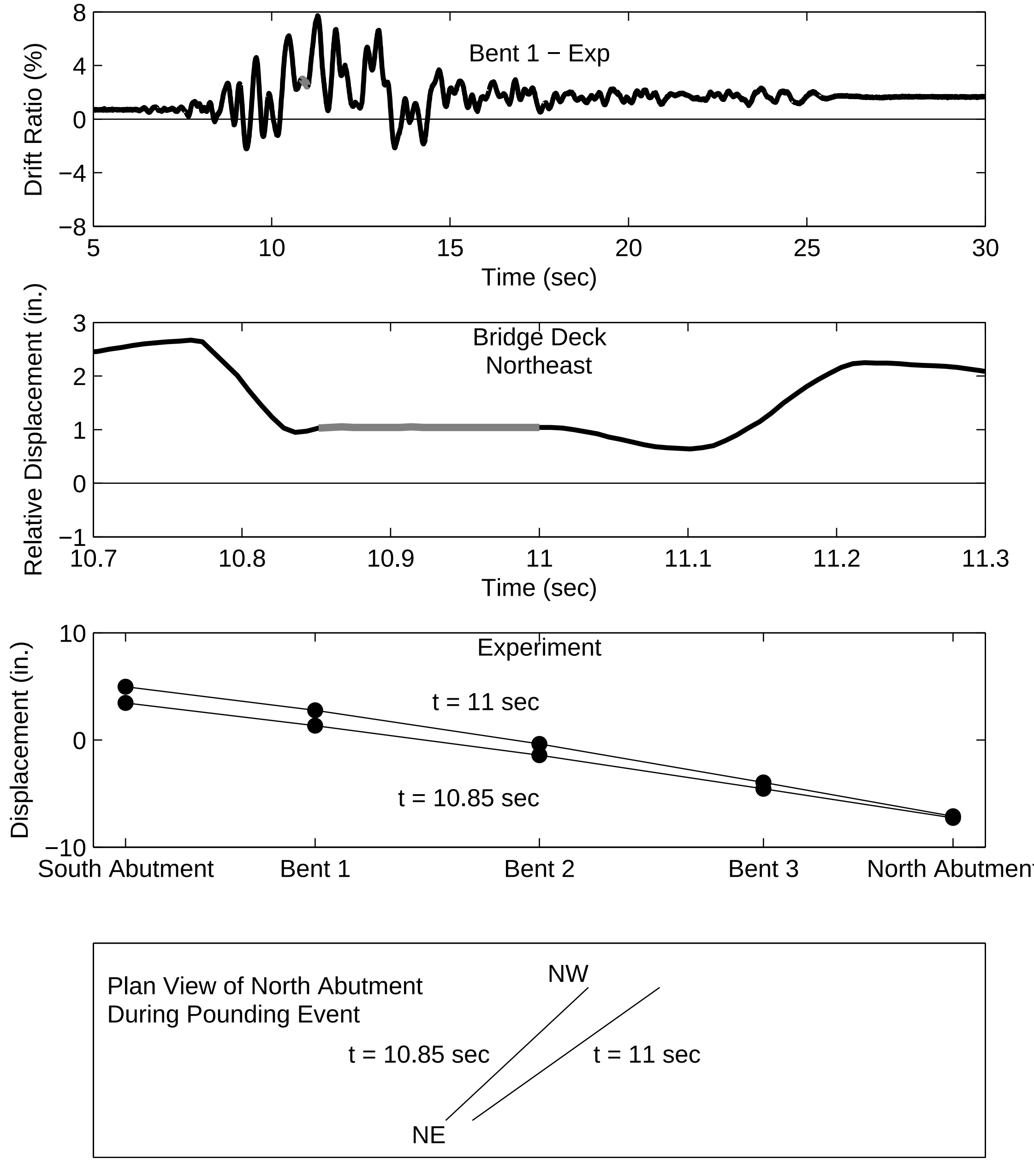

Fig. 3.37 Profiles of the 4-span bridge deck and abutment during a pounding event from Test 6.

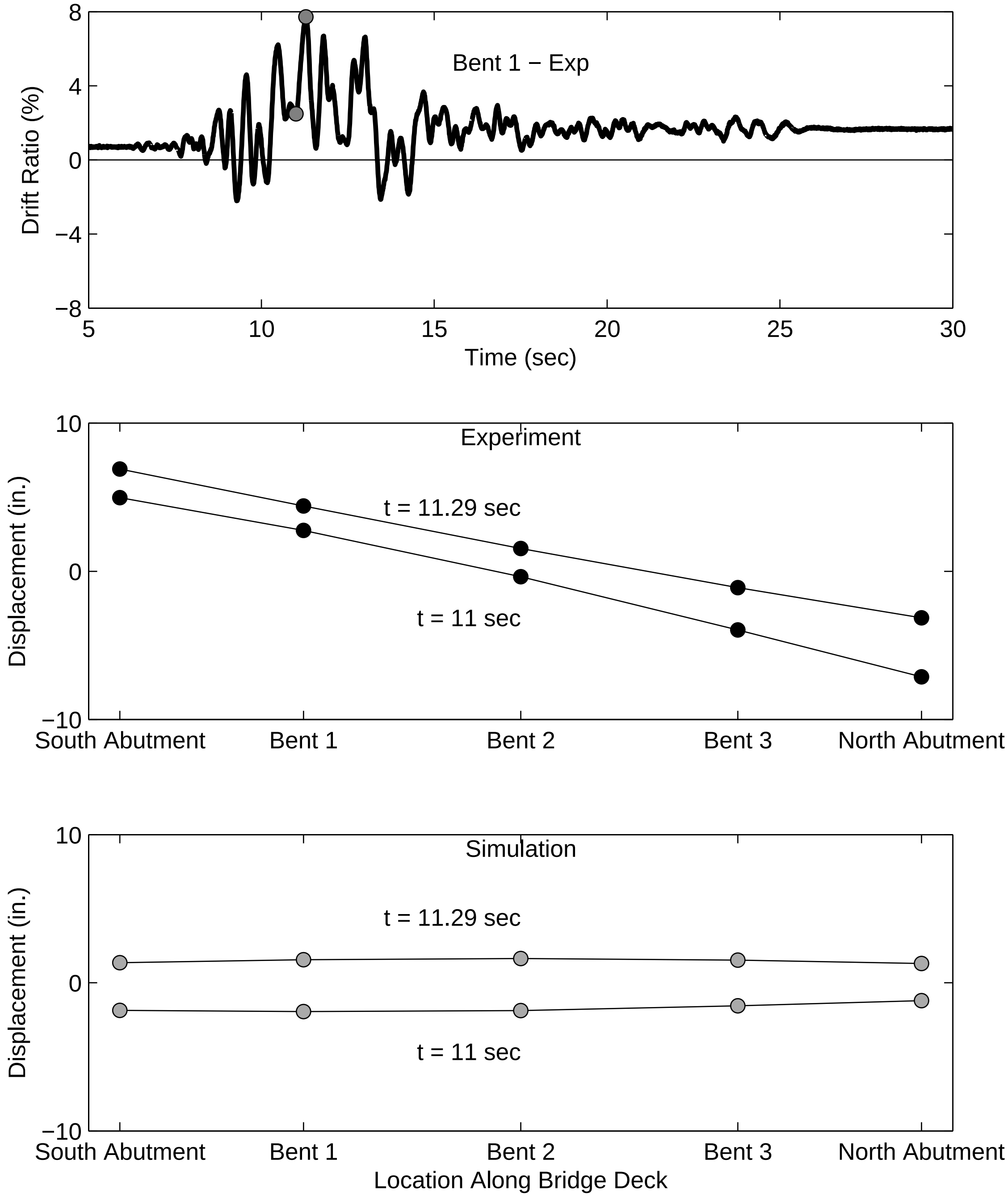

Fig. 3.38 Deck profiles from the experiment and Calibrated simulation model following a pounding event and at the peak drift ratio in bent 1 during Test 6.

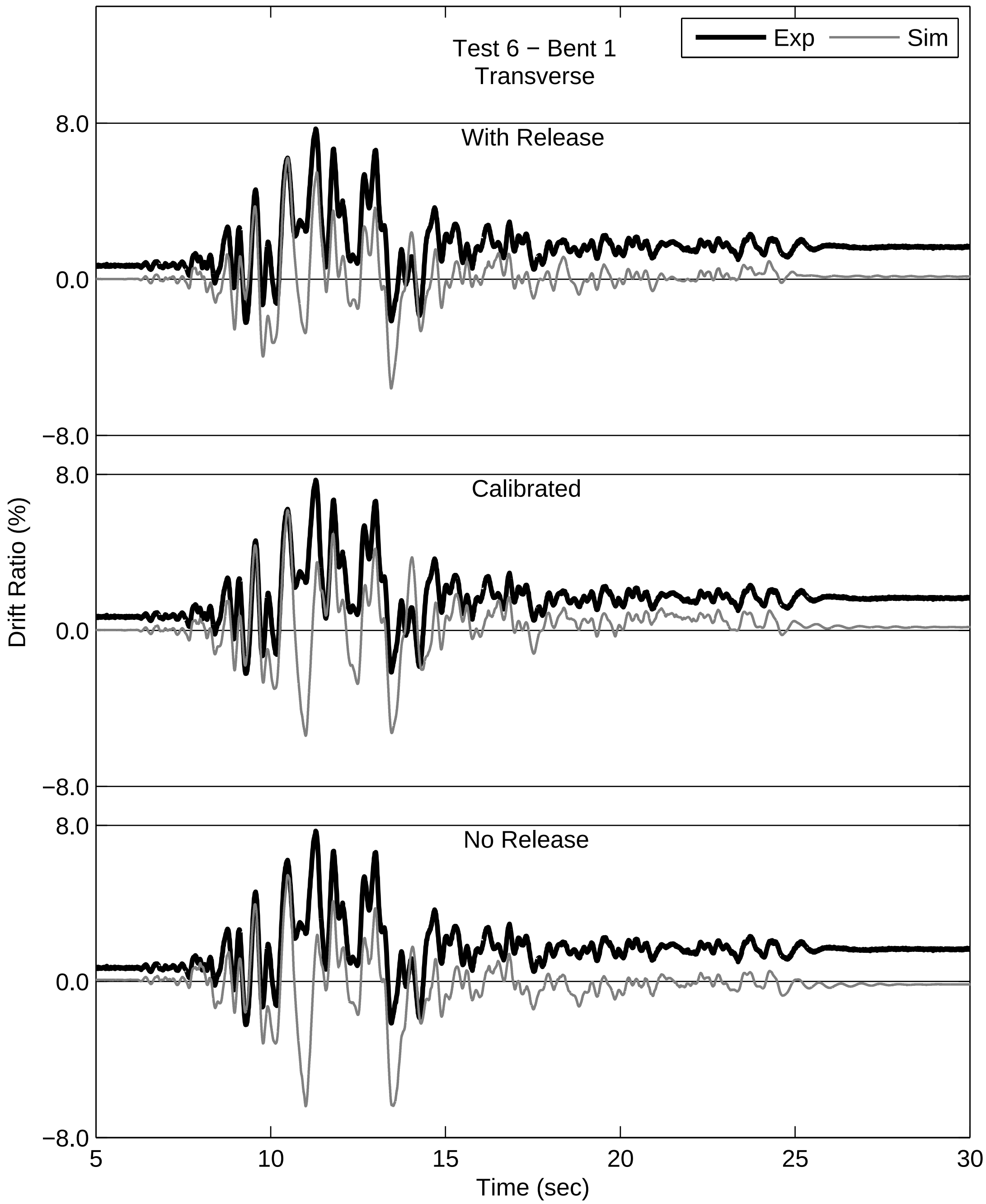

Fig. 3.39 Comparison of drift ratios at bent 1 in the transverse direction during Test 6 of the 4-span bridge when using different assumptions for the flexibility at the top of the cap beam.

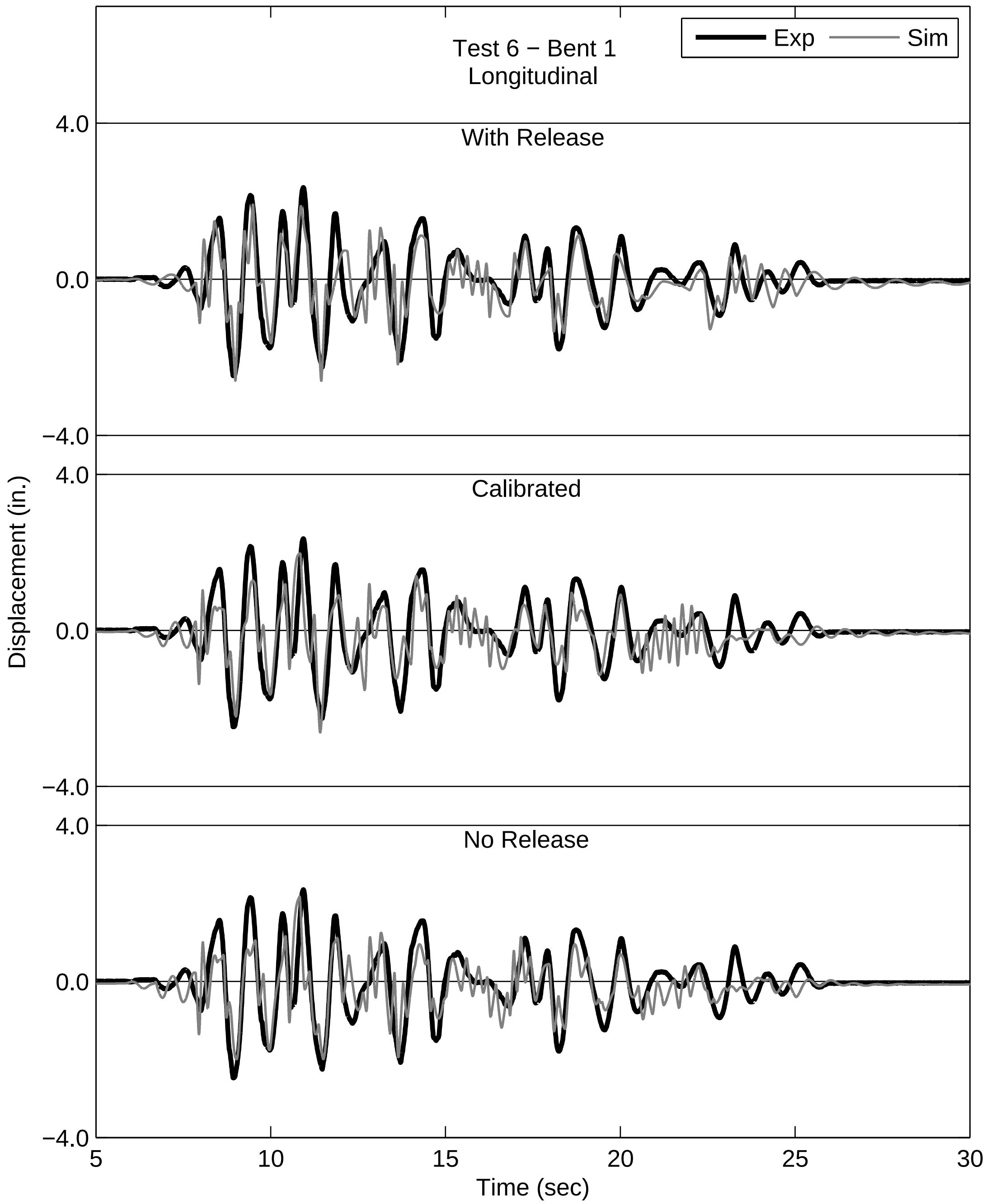

Fig. 3.40 Comparison of drift ratios at bent 1 in the longitudinal direction during Test 6 of the 4-span bridge when using different assumptions for the flexibility at the top of the cap beam.

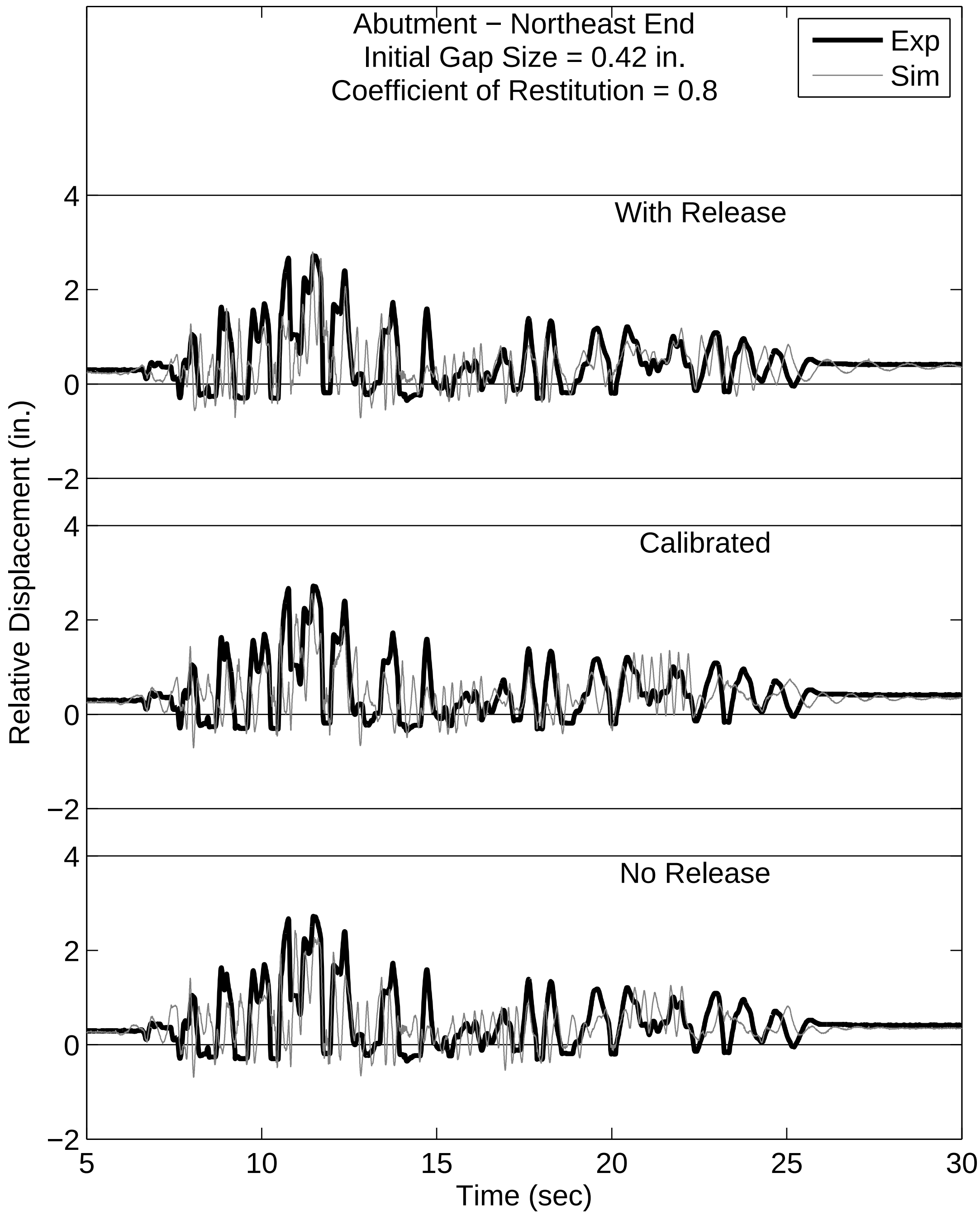

Fig. 3.41 Comparison of relative displacements between the deck and the abutment at the northeast of the 4-span bridge when using different assumptions for the flexibility at the top of the cap beam.

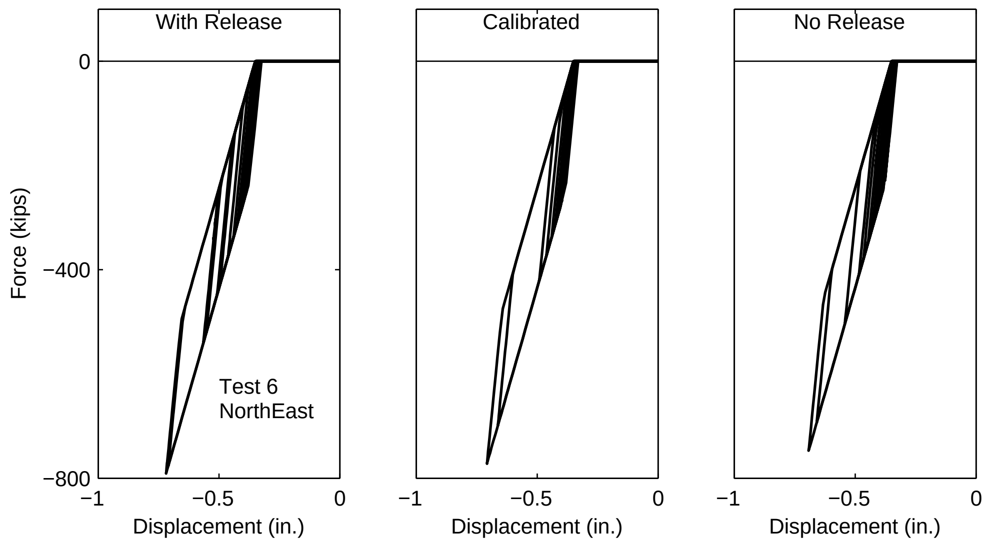

Fig. 3.42 Comparison of pounding between the deck and the abutment at the northeast of the 4-span bridge when using different assumptions for the flexibility at the top of the cap beam.

The peak curvature ductilities in both the transverse and longitudinal directions are compared in Figures 3.43 and 3.44. The predicted local response from the simulations gives good agreement with the measured curvatures in the transverse direction at bents 1 and 3 during Test 6, where curvature ductilities exceed 20 in bent 1. At these locations, the simulations do not overestimate or underestimate the local response by more than 25%. For Tests 4D and 5, when the response is not as nonlinear, the simulations do not predict the local response with such accuracy. The local response from the simulation models is more sensitive to the modeling assumptions for the curvatures in the longitudinal direction than for those in the transverse direction. For greater rotational restraint at the cap beam interface, the simulations predict larger curvatures in the longitudinal direction. Although the simulations predict drift ratios in the longitudinal direction during Test 6 within 17% relative error, the predicted curvature varies from 5−52% of that measured at bent 1. The greater stiffness of the moment-rotation model at the cap beam interface requires additional deformation concentrated at the bottom of the column giving significantly greater curvatures.

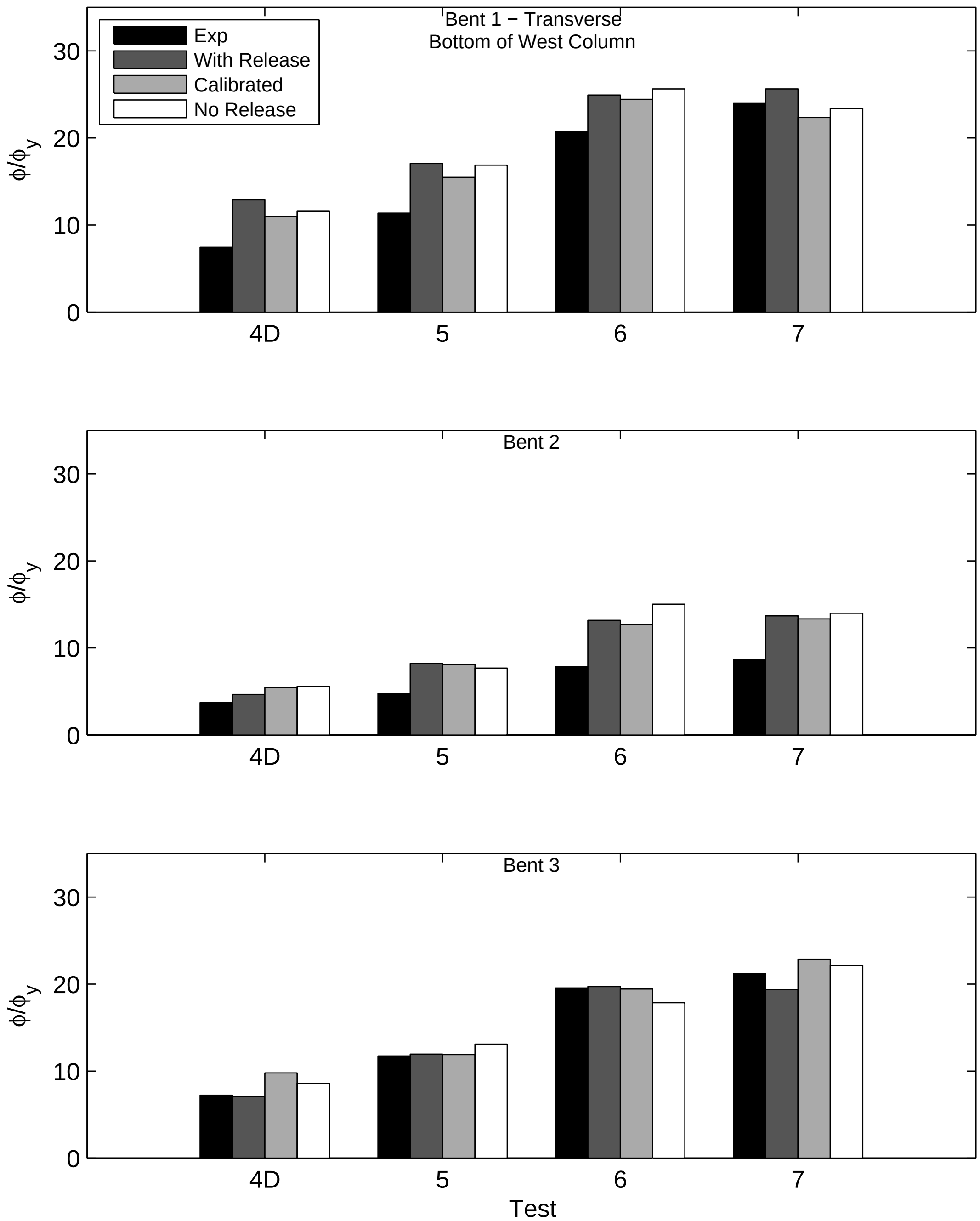

Fig. 3.43 Comparison of curvature ductilities in the transverse direction of the 4-span bridge when using different assumptions for the flexibility at the top of the cap beam.

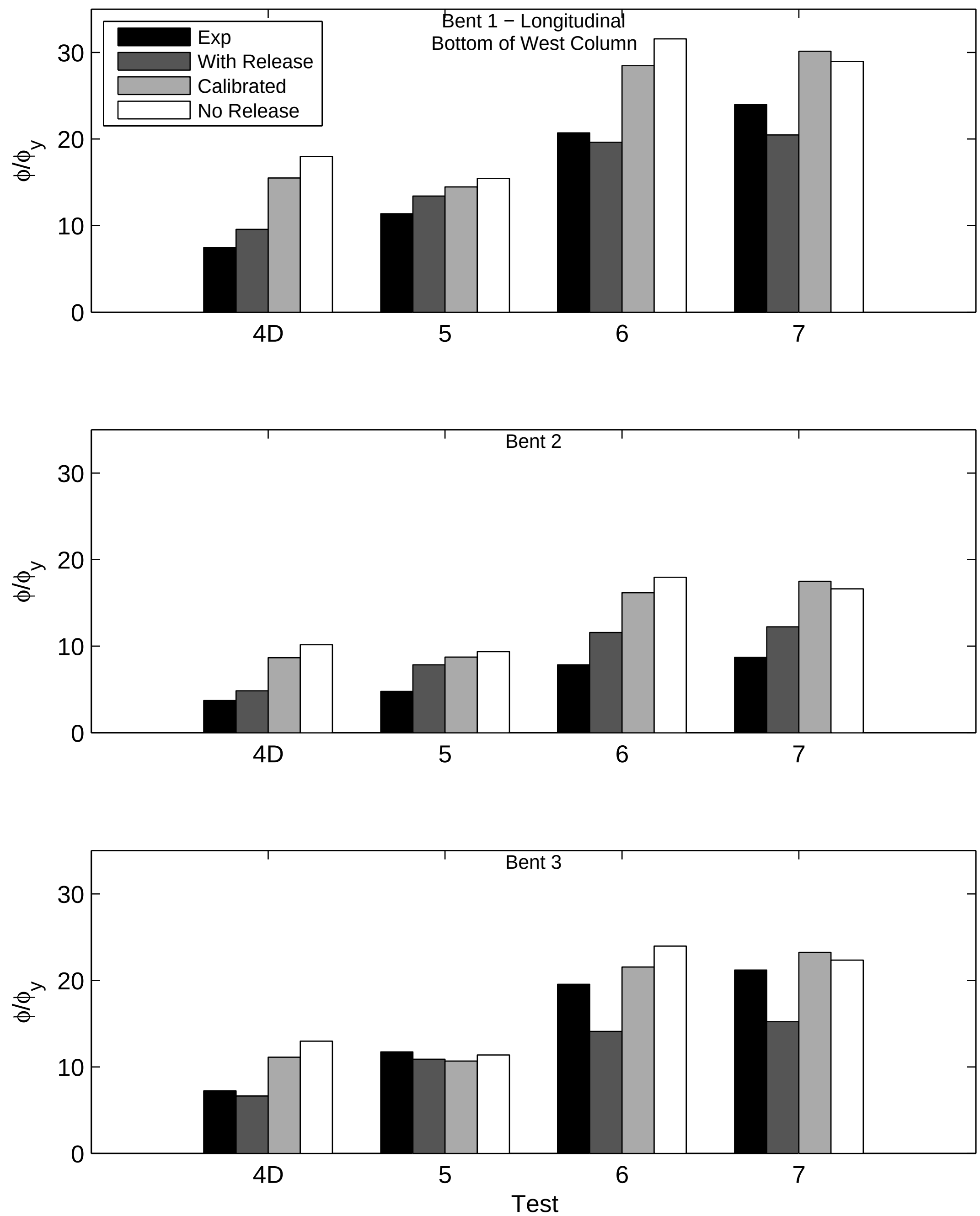

Fig. 3.44 Comparison of curvature ductilities in the longitudinal direction of the 4-span bridge when using different assumptions for the flexibility at the top of the cap beam.

3.6 CONCLUSIONS

Simulations of a two-span, reinforced concrete bridge using different column models demonstrate the ability to estimate accurately the global and local response for levels approaching failure. Appropriate simplified models that incorporate degradation with increasing damage are necessary to give accurate predictions of the collapse of reinforced concrete bridges to facilitate performance-based engineering. In the absence of explicit models for aspects of failure including bar buckling, loss of confinement, and hoop fracture, the BWH model with a fixed plastic hinge length defined by Priestley matches both the local and global response well until the onset of failure. Column models employing a zero-length element at the column ends to account for strain penetration may underestimate the local response. The analyst must carefully select the fixed plastic hinge length for the BWH model as a shorter length may significantly influence the predicted local response. Further studies of the system response of a four-span, reinforced concrete bridge including abutments illustrate the complex interaction that can take place during pounding. The friction at contact points during sustained pounding events restricts the motion of the bridge in the transverse direction causing it to be driven to larger drift ratios upon release.

Careful coordination between the experimentalist and the analyst is vital to the development of a specimen and test protocol that will enhance validation studies. The experimentalist should execute the design by asking how the analyst might validate the results given the instrumentation and test sequence. Examples of such consideration may include the selection of the sampling interval and length of the measured record for system identification studies, applying multiple white noise tests between strong motion tests, acquiring appropriate instrumentation to measure peak curvatures at the column ends, and implementing a test protocol that will challenge the analyst to differentiate between widely varying levels of damage from one test to the next. More refined models for flexural failure including loss of confinement and buckling of longitudinal reinforcement must be developed to facilitate the accurate prediction of collapse by the simulations. In light of the ever increasing computing power available to structural engineers, well-validated models will enable greater confidence in decisions made within a performance-based engineering framework using high-fidelity simulations.

4 Development of a Prototype Bridge Model Including SFSI

4.1 INTRODUCTION

This chapter addresses the development of a prototype bridge model and input excitation used to investigate the influence of soil-foundation-structure interaction (SFSI) on the bridge response. The following details the prototype bridge system, defines the hazard, including the selection of ground motions and the site response analysis to account for the soil profiles considered, and describes the OpenSees simulation model. Using the modeling assumptions defined in this chapter, large-scale parameter studies of prototype bridge systems are conducted to quantify the SFSI effect as discussed in Chapter 5.

4.2 PROTOTYPE BRIDGE SYSTEM

The prototype bridge is based on scaled properties of the two-span and four-span bridges that were tested at 1/4 scale as discussed in Chapter 3. The bridge design consists of the column heights and cap beam geometry from the two-span tests and span lengths from the four-span bridge. A depth to fixity of two column diameters gives clear column heights of 12 ft, 24 ft, and 16 ft for bents 1, 2, and 3, respectively. The reinforcement ratios for the longitudinal and transverse reinforcement of the columns and cap beams remain the same as for the two-span bridge. Figure 4.1 shows the geometry for the post-tensioned box girder deck described by Johnson et al. (2006). The bridge foundations are cast-in-drilled-hole shafts with embedment lengths scaled from 1/52-scale centrifuge tests performed in a companion study (Shin et al., 2006).

This study is concerned with the variation in bridge response for different hazard levels and site effects and investigates two different soil profiles as shown in Figure 4.2. Table 4.1 lists pertinent geometry for the prototype bridge system. The first soil profile is a medium-dense Nevada sand consistent with that used in the centrifuge tests (Shin et al., 2006). The second soil profile has a soft clay above the sand layer that extends from bedrock to the pile ends. For both soil profiles, the water table is located at the ground surface for bent 2. These soil profiles are not representative of one individual site, but rather they are selected to study the impact of SFSI on the bridge response for a range of site conditions.

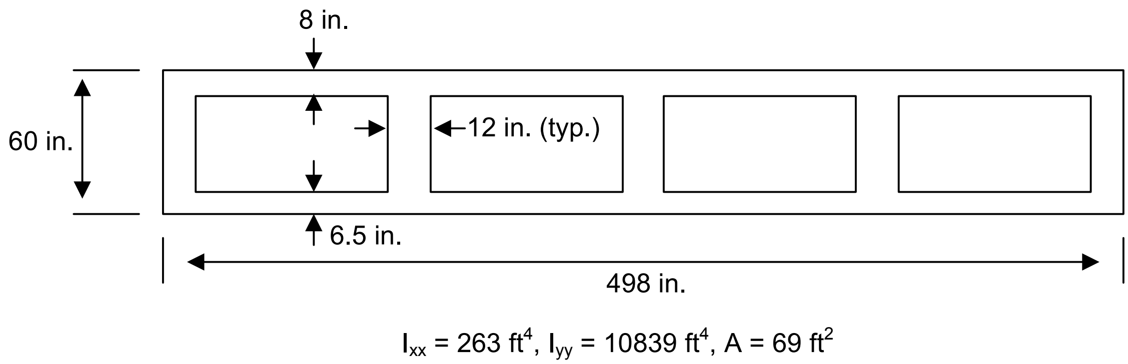

Fig. 4.1 Cross section of box girder for prototype bridge model.

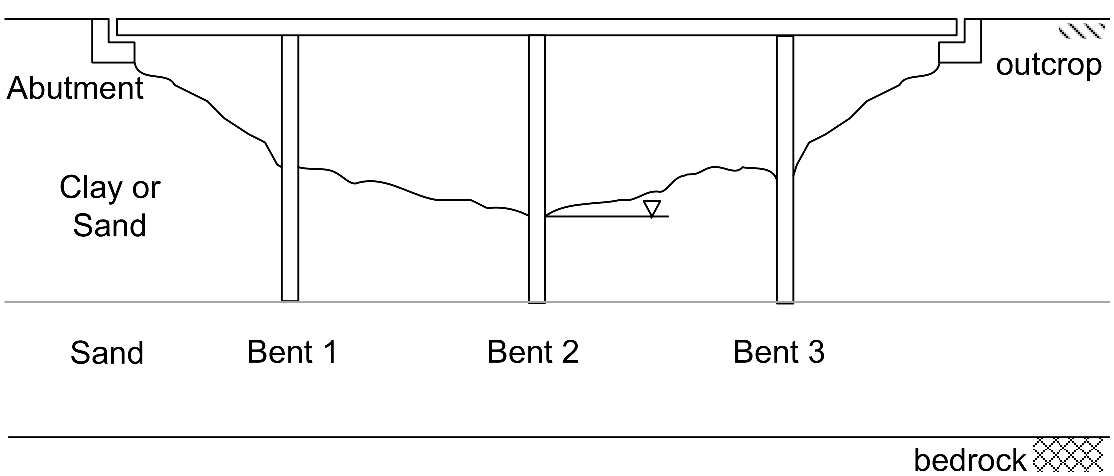

Fig. 4.2 Soil profile for prototype bridge model.

Table 4.1 Dimensions for prototype soil profile.

Location	Depth Below Centroid of Deck (ft)			
	Abutments	Bent 1	Bent 2	Bent 3
Ground Surface	0	14.5	26.5	18.5
Drilled Shaft Tip	N.A.	65.3	65.3	65.3
Bedrock	113.7	113.7	113.7	113.7

4.3 DEFINITION OF INPUT EXCITATION

The designs of the prototype bridges used to develop similitude relationships for the two-span and four-span bridges comply with guidelines developed through the National Cooperative Highway Research Program (NCHRP) Project 12-49 (ATC/MCEER, 2003). Section 3.2.1 summarizes the design criteria for the prototype bridge associated with the tests of the two-span bridge. It is important to note that the structural designs of these prototype bridges are unique and apply to a specific hazard level dependent on the location and site conditions under consideration. However, the general trends for this typical bridge and sites are instructive in understanding the influence of SFSI on the structural response within a performance-based engineering framework.

4.3.1 Selection of Outcrop Ground Motions

Ground motions of varying magnitude and distance from the fault constitute the basis for the probabilistic seismic hazard analysis. Other researchers have utilized this approach to quantify structural demands for a range of buildings and bridges with different periods using a performance-based framework developed within the Pacific Earthquake Engineering Research Institute (PEER) (Mackie and Stojadinovic, 2003; Medina and Krawinkler, 2004; Aviram et al., 2008b). To investigate the sensitivity of the bridge response to a variety of hazard levels, Mackie defined the input using ground motions from four bins (Mackie and Stojadinovic, 2003). Each bin has two horizontal components for twenty ground motions, and the criteria for organizing the bins is:

- Large Magnitude-Large Distance, LMLR, (6.5 $<M_w<$ 7.0, 30 km $<$ R $<$ 60 km)
- Large Magnitude-Small Distance, LMSR, (6.5 $<M_w<$ 7.0, 13 km $<$ R $<$ 30 km)
- Small Magnitude-Large Distance, SMLR, (5.8 $<M_w<$ 6.5, 30 km $<$ R $<$ 60 km)
- Small Magnitude-Small Distance, SMSR, (5.8 $<M_w<$ 6.5, 13 km $<$ R $<$ 30 km).

Medina provides additional detail for the selection of the ground motions (Medina and Krawinkler, 2004). The ground motions originate from the PEER strong motion database for sites with shear wave velocities between 590−1200 ft/s (NEHRP Site D). Since the spectral acceleration at the fundamental period, $S_a(T_1)$, was the intensity measure, the frequency content was an important consideration when selecting the ground motions. To reduce the sensitivity of the response to frequency content, the ground motions from each bin have median spectral shapes that are comparable when scaled to an intensity measure dependent on the spectral acceleration at a particular period. Figure 4.3 shows the variation of magnitude and distance for each of the 80 ground motions included in the study. The response spectra in Figure 4.4 compare the mean of the SRSS of the two horizontal components for each ground motion in the bins with the design spectra. While the ground motion bins do not attempt to match a particular design level, this plot provides further insight into the hazard level associated with the input excitation selected as the basis for this study.

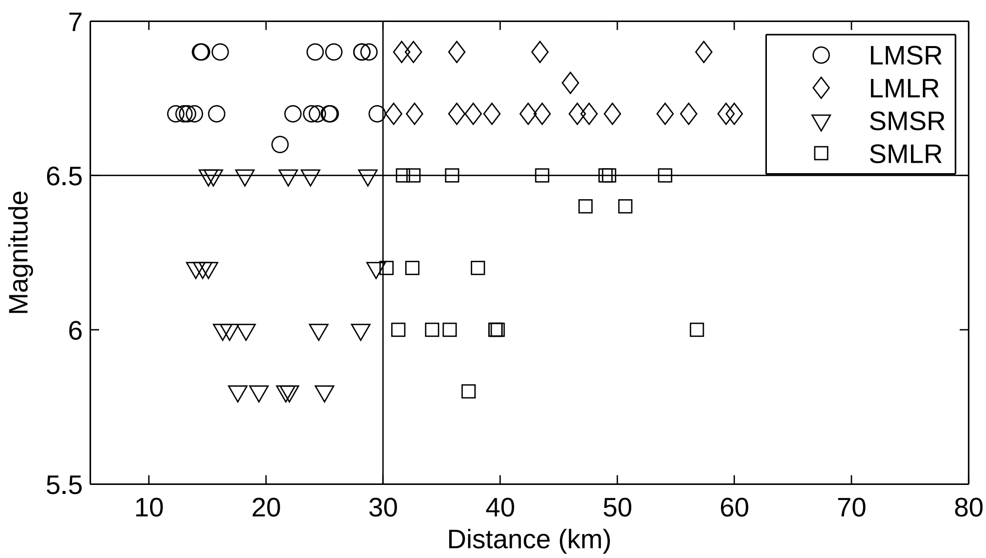

Fig. 4.3 Distribution of magnitudes and distances for ground motions considered.

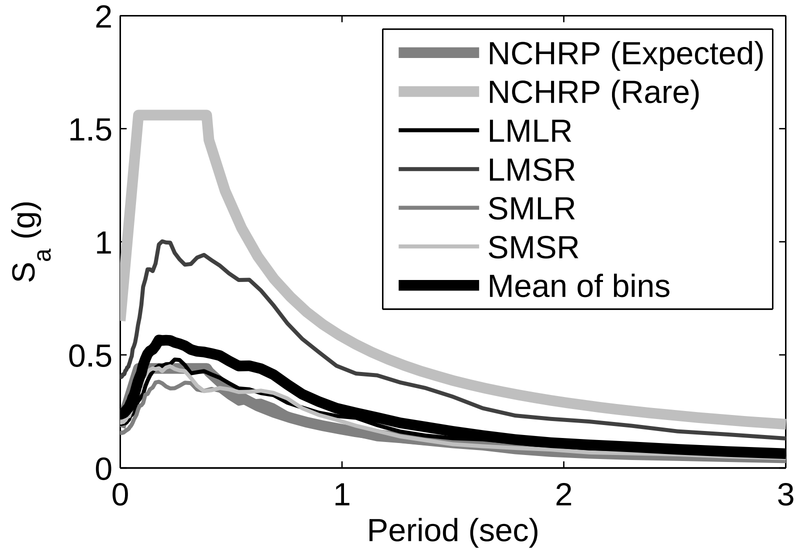

Fig. 4.4 Comparison of design response spectra versus ground motion bins.

4.3.2 Site Response Analysis

The input excitation consists of the free-field accelerations along the length of the drilled shaft foundations and at the abutments computed using Shake91 (Idriss and Sun, 1992). Table 4.2 lists the unit weights for the soils considered in the site response analyses. The values of the maximum

Table 4.2 Unit weights for SHAKE analyses.

Soil	Unit Weight (lb/ft^3)	
	Above Water Table	Below Water Table
sand	119	127
clay	100	104

shear modulus, G_{max}, for the soils follow the relationships utilized in a study by Boulanger et al. (1999). Using the relationship given by Seed and Idriss (1970), G_{max} for sand is:

$$\frac{G_{max}}{P_{atm}} = 21.8K_{2,max}\sqrt{\frac{\sigma'_m}{P_{atm}}} \tag{4.1}$$

where $K_{2,max}$ = 0.65, σ'_m = $(1 + 2K_0)\sigma'_{vc}$/3, K_0 = 0.6, P_{atm} is atmospheric pressure, σ'_m is the mean effective stress, σ'_{vc} is the vertical effective stress, and K_0 is the coefficient of lateral stress at rest. The maximum shear modulus for clay derives from the ratio $G_{max}/c_u = 380$, where c_u, the shear strength of the clay, is:

$$c_u = 0.35\sigma'_{vc}OCR^{0.8} \tag{4.2}$$

where OCR is the overconsolidation ratio. The overconsolidation ratio is assumed to be the average of an initial value equal to 8 and the final value following the earthquake increased by 30% to take into account additional consolidation that occurs during shaking. This overconsolidation ratio does not reflect a particular soil profile, but gives the soil a theoretical shear strength that is not greatly exceeded by the maximum shear stresses computed from the SHAKE analyses. Figure 4.5 compares the profiles for the maximum shear modulus at each layer used in the SHAKE analyses.

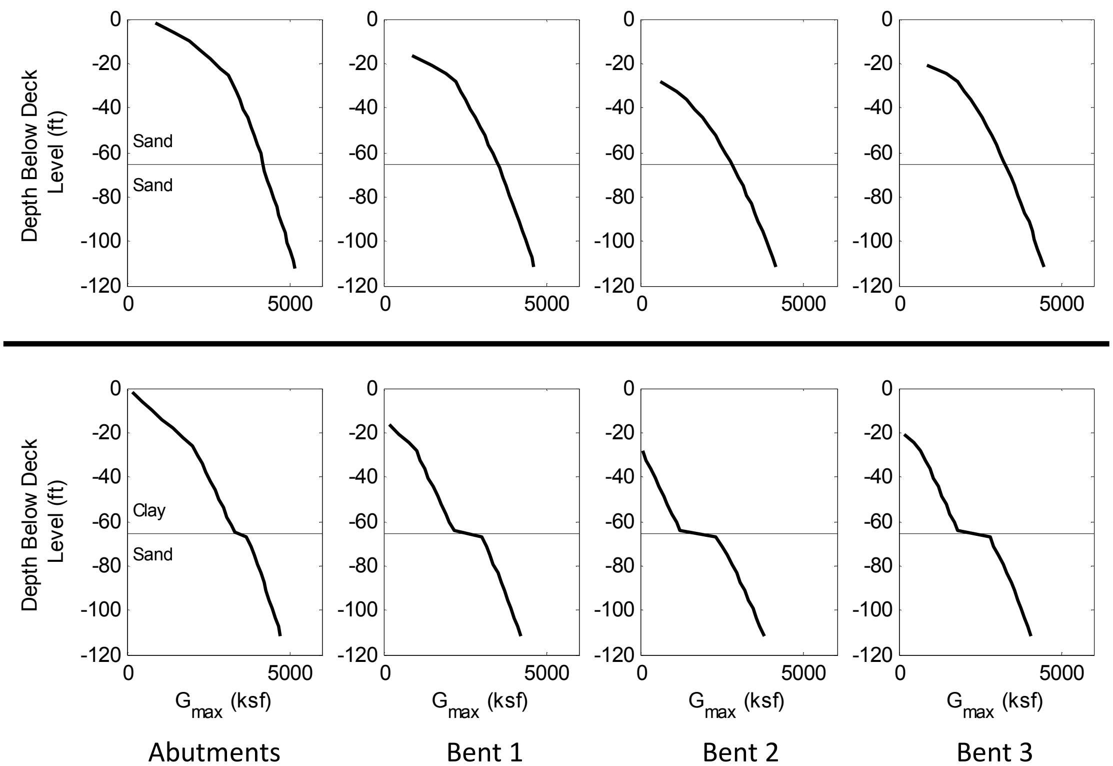

Fig. 4.5 G_{max} **profiles used in SHAKE analyses.**

To determine the sand material properties for the equivalent linear analysis, the average modulus reduction and damping relationships given by Seed and Idriss (1970) are used. The modulus reduction and damping relationships for clay assume the Vucetic and Dobry (1991) model for a plasticity index equal to 50. At large strains, G/G_{max} for clay equals 0.17 to limit the peak shear stress as described by Boulanger et al. (1999). Figure 4.6 compares the aforementioned relationships. For both horizontal components of each recorded ground motion, the bedrock motions

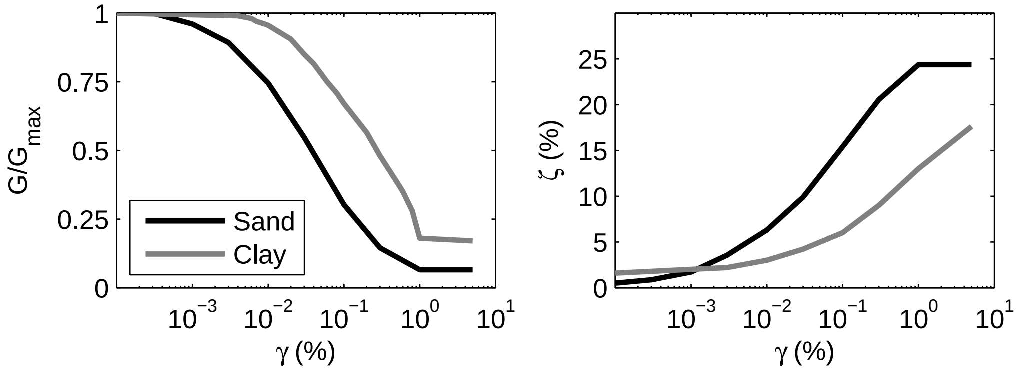

Fig. 4.6 Modulus reduction and damping relationships for sand and clay soil used in SHAKE analyses.

are evaluated by deconvolution of the input outcrop motions at the abutments, and the acceleration time histories at the soil layers of interest are then calculated by solving the wave equation. The number of layers is 30, 26, 23, and 25 at the abutments and bents 1, 2, and 3, respectively. The layer thickness for the SHAKE analyses does not exceed 4.4 ft and the selected discretization allows for appropriate transitions of material properties at the water table and for changes in the soil type. The material relationships for bedrock follow those given by Schnabel with a unit weight of 140 lb/ft^3 and shear wave velocity equal to 4000 ft/s. The ratio of the equivalent uniform shear strain to the maximum shear strain for each layer is 0.65 and the number of iterations is 10. Each ground motion has at least an additional 300 values to be included for use in the Fourier transform and the cutoff frequency is 25 Hz.

Figures 4.7 and 4.8 show the profiles of maximum shear strain versus depth for each of the sites and ground motion bins included in the SHAKE analyses. The computed maximum shear strains lie within acceptable limits with excessive strains over 1% observed only for several ground motions at the top of the clay layer. Figures 4.9 and 4.10 provide more insight into the SHAKE results by comparing the computed maximum shear stress with the theoretical shear strength of the soils. Equation 4.2 gives the theoretical shear strength of the clay and that of the sand is:

$$c_u = \sigma'_{vc} tan(\phi') \tag{4.3}$$

where ϕ' is the effective friction angle for the sand. The maximum shear stresses calculated from SHAKE are within acceptable limits given that the focus of this study is to assess the impact of SFSI on the structural response. Tables 4.3 through 4.10 list the peak ground accelerations for the outcrop and bedrock motions as well as the amplification factors for the surface motions computed using SHAKE. Significant amplification of the peak ground accelerations occur at the surface with this effect being more pronounced in the soil profile with clay overlying sand.

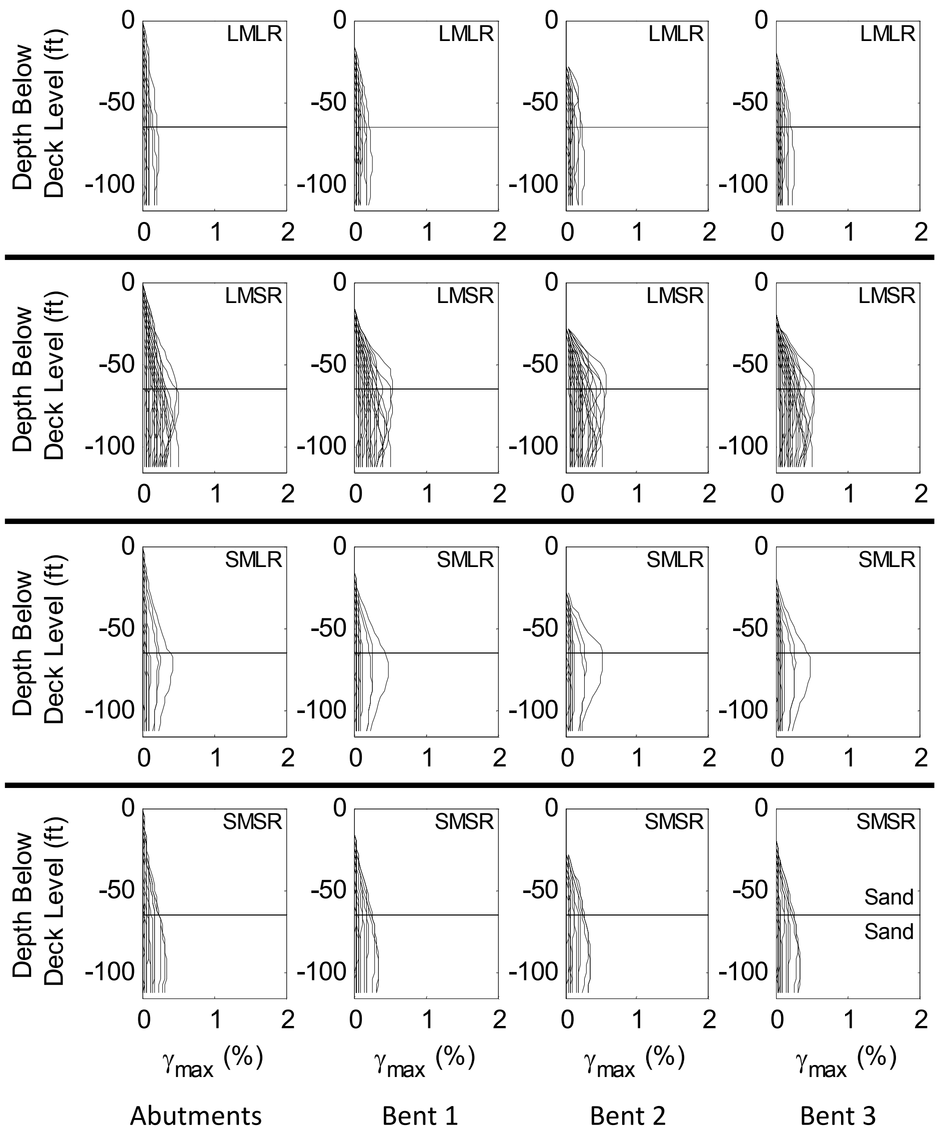

Fig. 4.7 Maximum shear strain for sand soil profile in SHAKE analyses.

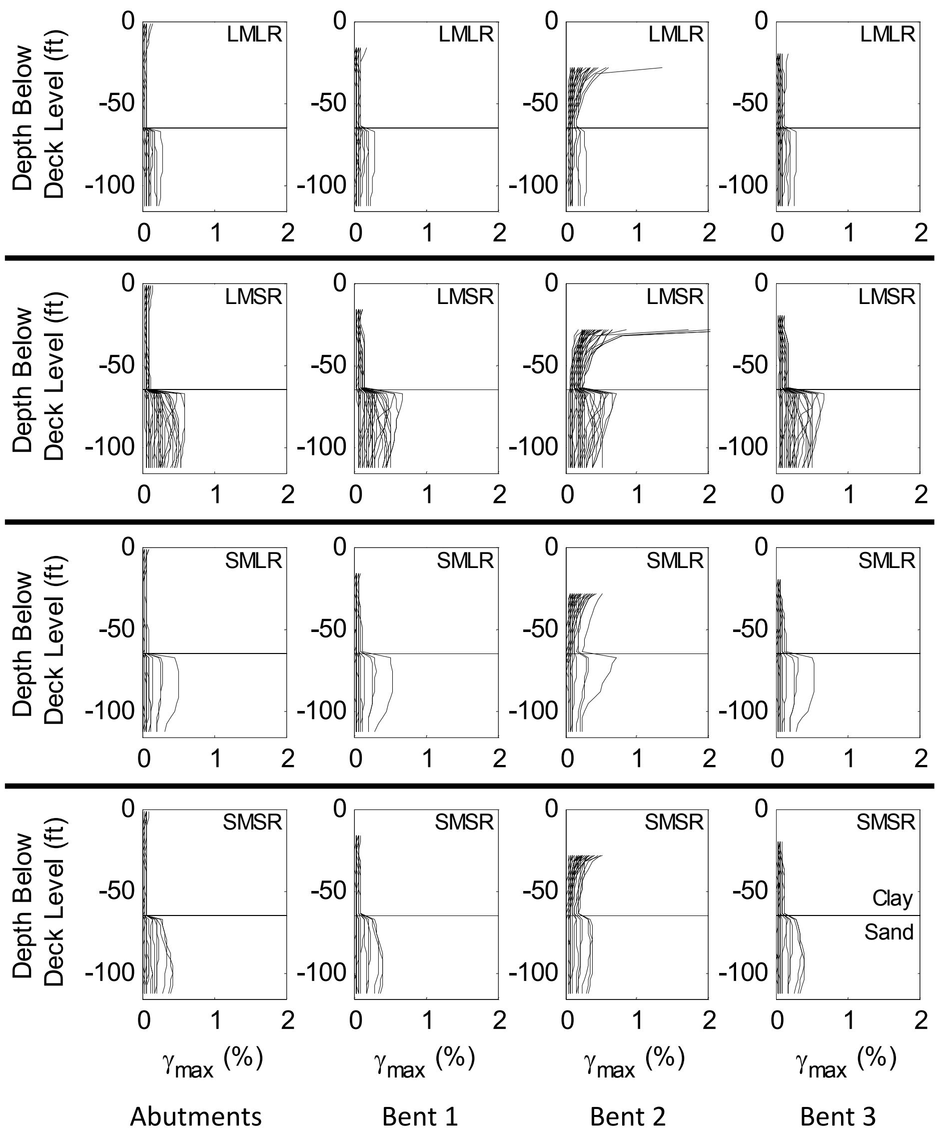

Fig. 4.8 Maximum shear strain for clay over sand soil profile in SHAKE analyses.

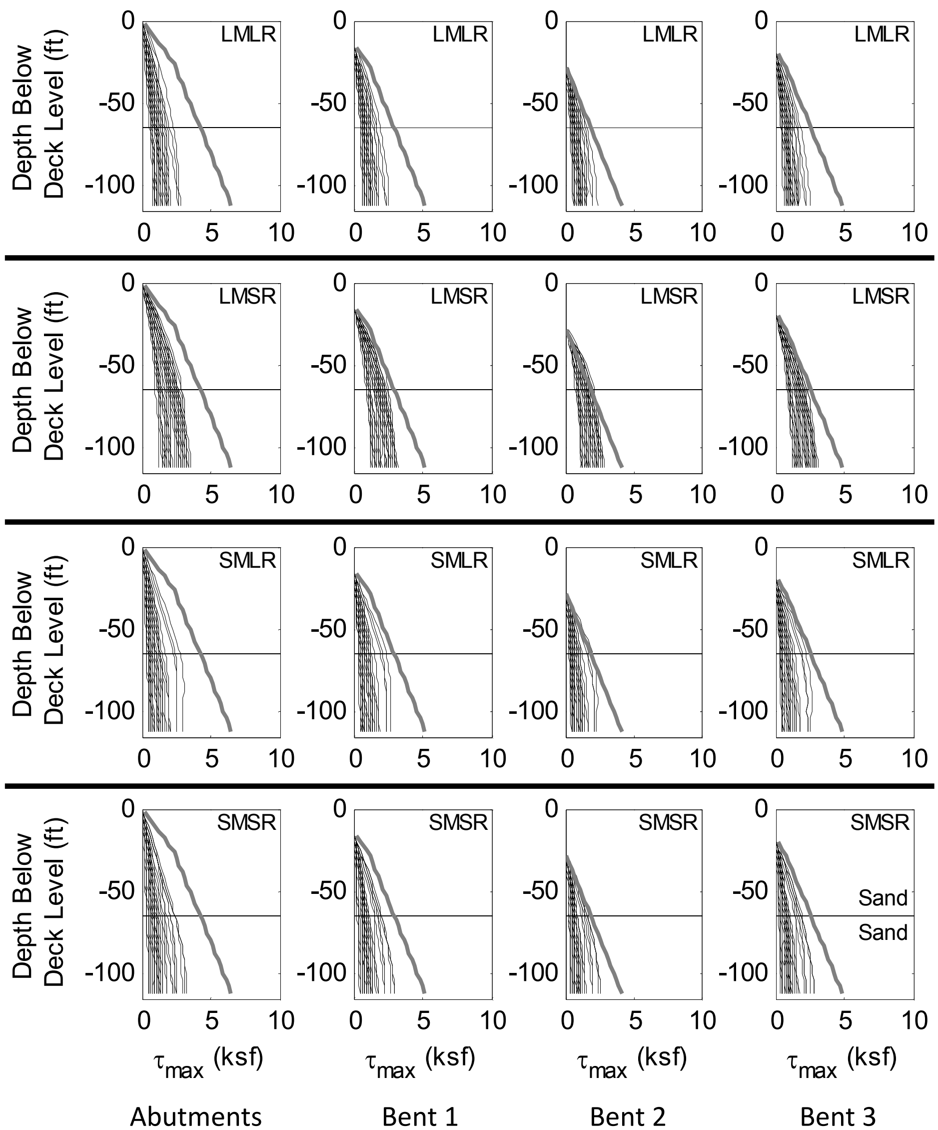

Fig. 4.9 Maximum shear stress for sand soil profile in SHAKE analyses. The gray line denotes the theoretical shear strength of the soil.

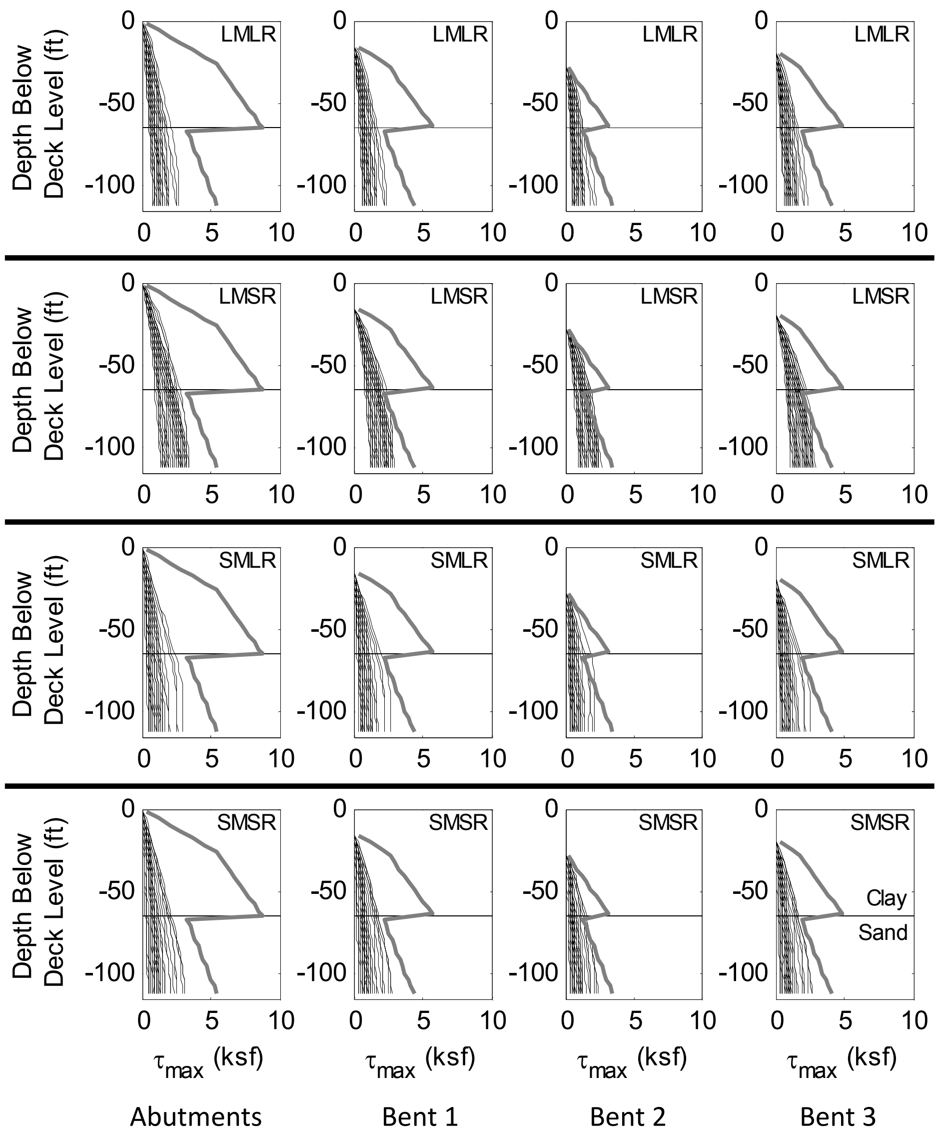

Fig. 4.10 Maximum shear stress for clay over sand soil profile in SHAKE analyses. The gray line denotes the theoretical shear strength of the soil.

Table 4.3 Peak ground accelerations for sand profile for LMLR bin.

	PGA (g)		$PGA_{surface}/PGA_{bedrock}$			
Record	outcrop	bedrock	Abutments	Bent 1	Bent 2	Bent 3
A2E000	0.17	0.15	1.90	1.85	1.99	1.87
A2E090	0.14	0.11	2.01	2.01	2.12	2.01
AELC180	0.13	0.11	1.83	1.79	1.88	1.80
AELC270	0.06	0.05	1.57	1.65	1.60	1.63
BAD000	0.10	0.08	2.34	2.41	2.64	2.47
BAD270	0.08	0.06	2.84	2.96	3.16	2.99
CAS000	0.09	0.08	2.05	2.07	2.57	2.26
CAS270	0.14	0.11	1.81	1.95	2.17	1.96
CEN155	0.46	0.38	1.50	1.48	1.58	1.48
CEN245	0.32	0.26	1.67	1.66	1.66	1.64
DEL000	0.14	0.12	1.68	1.50	1.66	1.50
DEL090	0.12	0.10	2.22	2.22	2.42	2.20
DWN090	0.16	0.14	1.94	1.96	2.01	1.95
DWN360	0.23	0.19	1.83	1.79	1.99	1.82
FMS090	0.19	0.15	2.00	1.87	1.78	1.83
FMS180	0.14	0.12	1.73	1.96	2.17	2.01
HVR000	0.13	0.11	1.94	1.84	1.79	1.83
HVR090	0.10	0.09	2.41	2.28	2.44	2.25
JAB220	0.10	0.07	2.69	2.53	2.66	2.54
JAB310	0.07	0.06	2.10	2.16	2.20	2.18
LH1000	0.09	0.08	2.14	2.09	2.22	2.11
LH1090	0.08	0.06	2.15	2.06	1.92	2.01
LOA092	0.09	0.08	1.72	1.88	2.08	1.94
LOA182	0.15	0.12	1.79	1.95	2.21	1.98
LV2000	0.09	0.07	2.06	1.83	1.62	1.73
LV2090	0.06	0.05	2.86	2.51	2.56	2.46
PHP000	0.06	0.05	1.97	2.12	2.21	2.11
PHP270	0.07	0.05	2.07	1.87	1.98	1.96
PIC090	0.10	0.08	2.84	2.90	3.10	2.95
PIC180	0.18	0.14	2.15	2.14	2.17	2.15
SJW160	0.09	0.07	2.08	2.26	2.35	2.28
SJW250	0.11	0.09	2.27	2.12	2.24	2.14
SLC270	0.19	0.15	2.08	2.07	2.14	2.06
SLC360	0.28	0.25	1.33	1.46	1.68	1.52
SOR225	0.06	0.05	2.35	2.25	2.50	2.24
SOR315	0.07	0.05	2.23	2.29	2.58	2.37
SSE240	0.13	0.12	1.98	2.01	2.03	2.00
SSE330	0.20	0.16	2.02	1.76	1.89	1.77
VER090	0.12	0.12	1.63	1.42	1.46	1.41
VER180	0.15	0.11	2.42	2.60	2.75	2.65
mean	0.14	0.11	2.05	2.04	2.15	2.05

Table 4.4 Peak ground accelerations for sand profile for LMSR bin.

	PGA (g)		$PGA_{surface}/PGA_{bedrock}$			
Record	outcrop	bedrock	Abutments	Bent 1	Bent 2	Bent 3
AGW000	0.17	0.16	1.28	1.48	1.66	1.55
AGW090	0.16	0.13	1.85	1.95	2.11	1.98
BICC000	0.35	0.30	1.33	1.36	1.40	1.36
BICC090	0.25	0.21	1.83	1.84	1.93	1.85
BIVW090	0.16	0.13	1.48	1.52	1.52	1.52
BIVW360	0.21	0.18	1.79	1.83	1.89	1.84
BWSM090	0.17	0.14	1.81	1.93	1.99	1.95
BWSM180	0.21	0.18	1.63	1.55	1.49	1.48
CAP000	0.51	0.46	1.12	1.13	1.16	1.13
CAP090	0.40	0.35	1.40	1.44	1.56	1.46
CNP106	0.36	0.32	0.97	1.04	1.12	1.05
CNP196	0.42	0.38	1.22	1.25	1.40	1.27
FAR000	0.27	0.22	1.96	1.97	2.02	1.97
FAR090	0.24	0.21	1.62	1.67	1.71	1.68
FLE144	0.16	0.13	2.15	2.10	2.15	2.09
FLE234	0.24	0.21	1.58	1.68	1.80	1.70
G03000	0.55	0.51	1.07	1.06	1.21	1.08
G03090	0.36	0.34	1.20	1.18	1.18	1.18
G04000	0.41	0.37	1.35	1.33	1.49	1.35
G04090	0.21	0.19	1.78	1.78	1.77	1.77
GLP177	0.34	0.28	1.41	1.33	1.42	1.30
GLP267	0.21	0.18	1.59	1.48	1.56	1.47
GMR000	0.22	0.19	1.62	1.64	1.73	1.66
GMR090	0.32	0.28	1.19	1.20	1.29	1.21
HCH090	0.25	0.21	1.84	1.86	1.92	1.86
HCH180	0.21	0.18	1.93	1.97	1.99	1.97
HDA165	0.27	0.23	1.60	1.68	1.79	1.71
HDA255	0.28	0.24	1.69	1.80	1.92	1.83
HOL090	0.23	0.19	1.74	1.75	1.90	1.79
HOL360	0.36	0.32	1.07	1.08	1.09	1.08
LOS000	0.41	0.38	1.03	1.04	1.13	1.05
LOS270	0.48	0.44	0.98	0.99	1.04	1.00
NYA090	0.18	0.14	1.62	1.84	1.86	1.84
NYA180	0.16	0.14	2.05	2.12	2.34	2.15
PEL090	0.20	0.18	1.40	1.46	1.55	1.48
PEL180	0.17	0.15	1.57	1.56	1.64	1.56
RO3000	0.28	0.27	1.52	1.60	1.69	1.61
RO3090	0.44	0.40	1.32	1.34	1.42	1.35
SVL270	0.20	0.18	1.68	1.68	1.65	1.67
SVL360	0.21	0.19	1.35	1.50	1.69	1.54
mean	0.28	0.25	1.52	1.55	1.63	1.56

Table 4.5 Peak ground accelerations for sand profile for SMLR bin.

	PGA (g)		$PGA_{surface}/PGA_{bedrock}$			
Record	outcrop	bedrock	Abutments	Bent 1	Bent 2	Bent 3
ABIR090	0.24	0.20	1.52	1.62	1.77	1.65
ABIR180	0.30	0.27	1.51	1.54	1.66	1.56
ACTS000	0.05	0.04	2.43	2.33	2.92	2.56
ACTS090	0.06	0.05	3.19	2.82	2.96	2.75
AHAR000	0.06	0.04	2.57	2.11	2.23	2.04
AHAR090	0.07	0.05	3.74	3.59	3.04	3.42
ASSE252	0.04	0.04	2.51	2.59	2.60	2.60
ASSE342	0.04	0.03	2.47	2.47	2.61	2.40
ASTC090	0.16	0.13	1.93	2.06	2.28	2.09
ASTC180	0.12	0.09	1.83	1.92	2.10	1.92
ASTP093	0.05	0.04	2.02	2.05	2.24	2.11
ASTP183	0.07	0.07	1.97	1.94	2.14	1.91
BELC000	0.07	0.05	2.14	2.21	2.26	2.24
BELC090	0.04	0.04	2.02	2.14	2.21	2.13
H06270	0.07	0.06	1.77	1.90	2.19	1.96
H06360	0.06	0.05	2.40	2.16	2.13	2.16
HC05270	0.15	0.13	1.65	1.73	1.86	1.76
HC05360	0.13	0.10	2.18	2.35	2.45	2.37
HC08000	0.10	0.08	2.30	2.23	2.18	2.21
HC08270	0.10	0.07	2.83	2.73	2.84	2.74
HCC4045	0.11	0.09	2.43	2.48	2.59	2.50
HCC4135	0.13	0.10	2.89	2.96	3.05	2.98
HCMP015	0.18	0.15	1.90	1.85	2.06	1.87
HCMP285	0.14	0.12	1.81	1.86	2.11	1.88
HDLT262	0.22	0.21	1.54	1.58	1.67	1.60
HDLT352	0.33	0.28	1.32	1.33	1.38	1.34
HNIL090	0.11	0.10	1.42	1.65	1.71	1.69
HNIL360	0.07	0.06	2.33	2.31	2.45	2.28
HPLS045	0.04	0.03	2.50	3.21	3.42	3.26
HPLS135	0.06	0.05	1.93	2.09	2.43	2.16
HVCT075	0.12	0.10	1.74	1.95	2.15	2.00
HVCT345	0.16	0.13	2.29	2.41	2.57	2.39
INO225	0.06	0.05	2.19	2.17	2.33	2.10
INO315	0.11	0.10	2.04	1.97	2.06	1.99
MCAP042	0.10	0.09	2.10	1.93	2.04	1.92
MCAP132	0.14	0.13	1.49	1.66	1.73	1.67
MHCH001	0.07	0.05	2.56	2.49	2.79	2.58
MHCH271	0.07	0.06	1.79	1.81	1.83	1.80
MSJB213	0.04	0.04	2.09	2.18	2.09	2.16
MSJB303	0.04	0.03	2.68	2.79	2.91	2.83
mean	0.11	0.09	2.15	2.18	2.30	2.19

Table 4.6 Peak ground accelerations for sand profile for SMSR bin.

	PGA (g)		$PGA_{surface}/PGA_{bedrock}$			
Record	outcrop	bedrock	Abutments	Bent 1	Bent 2	Bent 3
ACAS000	0.33	0.29	1.35	1.46	1.60	1.49
ACAS270	0.33	0.28	1.45	1.42	1.56	1.41
ACAT090	0.04	0.04	2.27	2.17	2.29	2.21
ACAT180	0.06	0.05	2.06	2.52	2.88	2.65
ADWN180	0.22	0.18	1.79	1.94	2.10	1.97
ADWN270	0.14	0.11	2.50	2.22	2.27	2.16
AKOD180	0.15	0.13	2.02	2.01	2.06	2.02
AKOD270	0.08	0.06	2.45	2.51	2.69	2.54
ASRM070	0.06	0.05	1.78	1.94	2.14	1.96
ASRM340	0.04	0.04	2.45	2.56	2.85	2.66
AW70000	0.20	0.16	1.96	1.96	1.98	1.95
AW70270	0.15	0.14	1.86	1.88	1.97	1.86
AWAT180	0.10	0.09	2.24	2.04	2.07	2.01
AWAT270	0.13	0.09	2.77	2.52	2.44	2.39
BRA225	0.15	0.13	1.74	1.82	2.00	1.83
BRA315	0.16	0.14	1.57	1.74	1.88	1.74
HCAL225	0.13	0.11	1.80	1.86	2.07	1.88
HCAL315	0.08	0.07	2.10	1.81	1.96	1.81
HCHI012	0.27	0.23	1.42	1.57	1.74	1.61
HCHI282	0.26	0.21	1.76	1.86	2.00	1.90
HE01140	0.14	0.11	2.29	2.12	2.06	2.01
HE01230	0.14	0.12	1.50	1.51	1.64	1.53
HE12140	0.14	0.12	1.56	1.55	1.65	1.52
HE12230	0.11	0.09	2.06	1.91	2.12	1.96
HE13140	0.11	0.10	2.02	1.94	2.11	1.99
HE13230	0.14	0.12	1.58	1.42	1.55	1.43
HWSM090	0.07	0.07	1.76	1.84	1.87	1.85
HWSM180	0.11	0.08	2.73	2.73	2.79	2.73
MAGW240	0.03	0.02	3.16	3.08	3.41	3.20
MAGW330	0.03	0.03	1.98	2.23	2.73	2.36
MG02000	0.16	0.12	2.12	2.07	2.15	2.04
MG02090	0.20	0.17	1.65	1.59	1.73	1.58
MG03000	0.19	0.17	1.32	1.41	1.67	1.47
MG03090	0.20	0.18	1.25	1.37	1.62	1.43
MGMR000	0.18	0.16	1.59	1.75	1.94	1.78
MGMR090	0.11	0.11	1.83	1.86	1.93	1.87
NIL000	0.10	0.08	2.26	2.15	2.14	2.06
NIL090	0.18	0.13	2.08	2.22	2.19	2.19
PHN180	0.11	0.09	2.23	2.26	2.27	2.26
PHN270	0.08	0.06	2.56	2.80	3.01	2.82
mean	0.14	0.12	1.97	1.99	2.13	2.00

Table 4.7 Peak ground accelerations for clay over sand profile for LMLR bin.

	PGA (g)		$PGA_{surface}/PGA_{bedrock}$			
Record	outcrop	bedrock	Abutments	Bent 1	Bent 2	Bent 3
A2E000	0.17	0.16	2.35	2.47	3.70	2.52
A2E090	0.14	0.11	2.83	2.75	3.90	2.75
AELC180	0.13	0.11	2.13	2.11	3.73	2.08
AELC270	0.06	0.05	2.38	2.48	4.44	2.64
BAD000	0.10	0.08	3.23	3.53	4.98	3.76
BAD270	0.08	0.06	3.72	3.82	4.72	3.96
CAS000	0.09	0.08	2.48	2.54	4.69	2.56
CAS270	0.14	0.12	3.36	3.30	4.07	3.26
CEN155	0.46	0.39	2.23	2.30	2.97	2.41
CEN245	0.32	0.26	2.55	2.48	2.45	2.42
DEL000	0.14	0.12	2.82	2.85	4.35	2.93
DEL090	0.12	0.09	3.67	3.96	5.10	4.21
DWN090	0.16	0.14	3.11	3.30	5.10	3.30
DWN360	0.23	0.20	2.62	2.74	4.01	2.83
FMS090	0.19	0.15	2.58	2.43	2.51	2.40
FMS180	0.14	0.12	2.61	2.96	4.90	3.32
HVR000	0.13	0.11	2.18	1.98	2.39	1.95
HVR090	0.10	0.09	2.75	2.57	3.63	2.56
JAB220	0.10	0.07	3.59	3.74	4.06	3.72
JAB310	0.07	0.06	3.07	3.17	4.15	3.12
LH1000	0.09	0.08	2.75	2.59	4.77	2.56
LH1090	0.08	0.07	2.98	2.95	4.58	2.93
LOA092	0.09	0.08	2.61	2.64	3.73	2.68
LOA182	0.15	0.12	3.28	3.27	3.09	3.30
LV2000	0.09	0.07	2.83	2.70	3.46	2.83
LV2090	0.06	0.05	3.76	3.47	4.26	3.58
PHP000	0.06	0.05	3.60	3.72	3.50	3.77
PHP270	0.07	0.06	3.10	2.83	3.39	2.58
PIC090	0.10	0.08	3.66	3.76	4.91	3.69
PIC180	0.18	0.15	2.35	2.39	2.99	2.44
SJW160	0.09	0.07	2.56	2.60	3.53	2.56
SJW250	0.11	0.09	2.87	3.23	5.19	3.50
SLC270	0.19	0.16	2.13	2.30	3.58	2.46
SLC360	0.28	0.25	1.97	2.03	3.32	2.06
SOR225	0.06	0.05	3.41	3.79	4.48	3.94
SOR315	0.07	0.05	3.52	3.51	4.53	3.65
SSE240	0.13	0.12	2.12	2.26	4.90	2.39
SSE330	0.20	0.17	2.27	2.37	4.14	2.70
VER090	0.12	0.11	2.80	2.90	5.33	3.04
VER180	0.15	0.11	3.80	3.47	4.29	3.29
mean	0.14	0.11	2.87	2.91	4.05	2.97

Table 4.8 Peak ground accelerations for clay over sand profile for LMSR bin.

	PGA (g)		$PGA_{surface}/PGA_{bedrock}$			
Record	outcrop	bedrock	Abutments	Bent 1	Bent 2	Bent 3
AGW000	0.17	0.16	1.86	1.85	4.80	1.95
AGW090	0.16	0.13	2.83	2.89	4.07	2.94
BICC000	0.35	0.31	1.43	1.48	2.10	1.55
BICC090	0.25	0.21	2.48	2.50	3.04	2.52
BIVW090	0.16	0.14	2.18	2.41	2.78	2.40
BIVW360	0.21	0.19	2.13	2.14	3.31	2.21
BWSM090	0.17	0.15	2.45	2.37	3.43	2.24
BWSM180	0.21	0.18	1.93	1.89	3.42	1.83
CAP000	0.51	0.45	1.54	1.50	2.83	1.54
CAP090	0.40	0.36	1.19	1.33	2.39	1.44
CNP106	0.36	0.32	1.44	1.32	1.85	1.26
CNP196	0.42	0.39	1.00	1.17	2.32	1.26
FAR000	0.27	0.22	2.31	2.35	3.08	2.41
FAR090	0.24	0.21	2.04	1.97	2.61	1.95
FLE144	0.16	0.13	3.21	3.11	4.29	3.04
FLE234	0.24	0.21	1.83	1.89	2.38	1.91
G03000	0.55	0.51	1.65	1.38	2.62	1.37
G03090	0.36	0.34	1.41	1.33	2.20	1.28
G04000	0.41	0.38	1.38	1.49	3.42	1.57
G04090	0.21	0.19	2.09	1.97	2.62	1.97
GLP177	0.34	0.28	2.64	2.55	3.42	2.52
GLP267	0.21	0.18	2.64	2.42	4.34	2.46
GMR000	0.22	0.20	3.07	2.65	3.36	2.37
GMR090	0.32	0.28	1.93	1.87	2.73	1.88
HCH090	0.25	0.21	1.76	1.88	2.38	1.93
HCH180	0.21	0.18	2.16	2.17	2.45	2.18
HDA165	0.27	0.23	1.61	1.78	1.92	1.87
HDA255	0.28	0.24	1.69	1.89	2.73	1.95
HOL090	0.23	0.19	2.14	2.13	2.54	2.09
HOL360	0.36	0.32	1.71	1.51	1.94	1.46
LOS000	0.41	0.38	1.02	1.09	2.04	1.12
LOS270	0.48	0.45	1.14	1.00	2.40	1.04
NYA090	0.18	0.14	3.10	2.83	4.15	2.81
NYA180	0.16	0.14	3.43	3.45	3.62	3.36
PEL090	0.20	0.19	1.89	1.88	3.36	1.91
PEL180	0.17	0.15	2.67	2.76	3.54	2.97
RO3000	0.28	0.26	1.84	1.94	3.12	1.99
RO3090	0.44	0.40	1.42	1.48	1.99	1.52
SVL270	0.20	0.18	2.08	1.87	2.79	1.80
SVL360	0.21	0.20	2.13	2.09	3.56	2.06
mean	0.28	0.25	2.01	1.99	2.95	2.00

Table 4.9 Peak ground accelerations for clay over sand profile for SMLR bin.

	PGA (g)		$PGA_{surface}/PGA_{bedrock}$			
Record	outcrop	bedrock	Abutments	Bent 1	Bent 2	Bent 3
ABIR090	0.24	0.20	3.02	2.74	3.23	2.58
ABIR180	0.30	0.28	1.38	1.40	2.78	1.44
ACTS000	0.05	0.04	3.40	3.37	4.35	3.40
ACTS090	0.06	0.05	4.80	4.57	5.76	4.63
AHAR000	0.06	0.04	3.63	3.17	4.97	3.27
AHAR090	0.07	0.05	4.47	4.29	5.06	4.20
ASSE252	0.04	0.04	2.99	3.20	5.16	3.46
ASSE342	0.04	0.03	3.32	3.16	5.04	3.32
ASTC090	0.16	0.13	3.24	3.17	4.41	2.97
ASTC180	0.12	0.10	3.31	3.19	4.27	3.08
ASTP093	0.05	0.04	2.46	2.60	3.95	2.71
ASTP183	0.07	0.07	2.24	2.22	3.48	2.25
BELC000	0.07	0.06	2.96	2.79	4.77	2.90
BELC090	0.04	0.04	2.95	3.24	4.44	3.65
H06270	0.07	0.06	3.47	3.46	4.12	3.82
H06360	0.06	0.04	4.01	4.06	4.67	4.03
HC05270	0.15	0.13	2.13	2.32	4.07	2.61
HC05360	0.13	0.11	2.48	2.74	3.69	2.97
HC08000	0.10	0.08	2.47	2.48	3.89	2.54
HC08270	0.10	0.08	3.07	3.08	3.95	3.09
HCC4045	0.11	0.10	3.04	3.09	3.72	3.09
HCC4135	0.13	0.10	3.16	3.27	4.28	3.37
HCMP015	0.18	0.15	3.04	3.05	4.49	3.10
HCMP285	0.14	0.12	2.92	3.09	5.19	3.23
HDLT262	0.22	0.19	1.87	1.87	2.65	1.85
HDLT352	0.33	0.29	1.65	1.51	2.37	1.46
HNIL090	0.11	0.10	2.33	2.19	3.30	2.16
HNIL360	0.07	0.06	3.59	3.76	5.70	3.68
HPLS045	0.04	0.03	4.03	4.17	5.95	3.89
HPLS135	0.06	0.05	3.33	3.59	6.85	3.45
HVCT075	0.12	0.11	3.02	2.68	4.50	2.82
HVCT345	0.16	0.13	4.21	3.84	4.49	3.58
INO225	0.06	0.05	4.26	4.07	5.18	3.82
INO315	0.11	0.10	3.61	3.47	4.50	3.22
MCAP042	0.10	0.08	4.42	3.95	4.55	3.93
MCAP132	0.14	0.14	2.68	2.29	4.73	2.21
MHCH001	0.07	0.06	2.78	2.83	3.99	2.78
MHCH271	0.07	0.07	2.38	2.37	3.88	2.30
MSJB213	0.04	0.04	3.04	3.05	4.46	3.39
MSJB303	0.04	0.03	3.37	3.49	5.01	3.69
mean	0.11	0.09	3.11	3.07	4.40	3.10

Table 4.10 Peak ground accelerations for clay over sand profile for SMSR bin.

	PGA (g)		$PGA_{surface}/PGA_{bedrock}$			
Record	outcrop	bedrock	Abutments	Bent 1	Bent 2	Bent 3
ACAS000	0.33	0.29	1.60	1.70	2.46	1.75
ACAS270	0.33	0.28	2.25	2.30	2.61	2.21
ACAT090	0.04	0.03	3.70	3.68	5.98	3.85
ACAT180	0.06	0.05	3.57	3.23	4.19	2.94
ADWN180	0.22	0.18	1.98	2.13	3.20	2.23
ADWN270	0.14	0.11	2.86	3.11	3.93	3.10
AKOD180	0.15	0.13	2.27	2.29	2.50	2.28
AKOD270	0.08	0.06	3.50	3.63	4.57	3.88
ASRM070	0.06	0.05	2.42	2.59	5.25	2.61
ASRM340	0.04	0.03	3.72	3.58	5.35	3.97
AW70000	0.20	0.17	2.12	2.17	2.83	2.19
AW70270	0.15	0.14	2.77	2.69	3.35	2.88
AWAT180	0.10	0.09	2.72	2.59	4.93	2.76
AWAT270	0.13	0.10	4.04	3.96	4.10	3.94
BRA225	0.15	0.14	3.37	3.25	4.77	3.40
BRA315	0.16	0.14	3.46	2.70	3.48	2.92
HCAL225	0.13	0.11	2.89	2.99	5.32	3.12
HCAL315	0.08	0.07	3.24	3.33	3.41	3.17
HCHI012	0.27	0.23	1.89	1.97	2.39	2.04
HCHI282	0.26	0.22	1.89	2.00	2.43	2.05
HE01140	0.14	0.11	3.61	3.38	4.08	3.42
HE01230	0.14	0.12	2.51	2.42	3.97	2.47
HE12140	0.14	0.13	2.56	2.56	2.85	2.27
HE12230	0.11	0.10	2.61	2.78	4.03	2.82
HE13140	0.11	0.10	3.05	3.08	4.03	3.20
HE13230	0.14	0.12	2.65	2.67	3.83	2.73
HWSM090	0.07	0.07	2.39	2.16	3.44	2.19
HWSM180	0.11	0.08	3.14	3.42	4.04	3.53
MAGW240	0.03	0.03	3.48	3.93	6.01	4.24
MAGW330	0.03	0.03	2.34	2.30	4.11	2.41
MG02000	0.16	0.12	3.35	3.44	4.27	3.57
MG02090	0.20	0.17	2.58	2.52	3.83	2.73
MG03000	0.19	0.17	1.98	2.20	3.90	2.39
MG03090	0.20	0.18	1.89	1.93	3.61	2.08
MGMR000	0.18	0.16	2.57	2.46	4.91	2.31
MGMR090	0.11	0.11	2.48	2.36	4.82	2.30
NIL000	0.10	0.08	3.25	3.06	4.40	3.22
NIL090	0.18	0.13	3.32	3.21	3.76	3.13
PHN180	0.11	0.09	2.64	2.61	3.20	2.62
PHN270	0.08	0.06	3.48	3.66	4.74	3.81
mean	0.14	0.12	2.80	2.80	3.97	2.87

4.3.3 Processing of Free Field Motions

To perform the nonlinear dynamic analyses of the bridge model in OpenSees, the multiple support excitation must use the displacement time histories at the location of each soil spring as well as at the abutments. The acceleration time histories computed from the SHAKE analyses are double integrated to obtain the displacement time histories. For many of the ground motions considered, such double integration leads to a significant offset in the associated displacement time histories. To prevent this error, a baseline correction applies the procedure proposed by Boore et al. (2002). The steps summarized below describe this method:

1. Subtract the mean of the acceleration time history from the whole record.
2. Integrate the acceleration to velocity.
3. Fit a quadratic to the velocity with starting value equal to zero and subtract the derivative of the quadratic from the zeroth-order-corrected acceleration.
4. Apply a fourth-order, low-cut Butterworth filter with corner frequency equal to 0.01 Hz to the corrected acceleration.
5. Double-integrate the filtered acceleration to obtain the displacement time history.

Figure 4.11 illustrates the benefit of applying this baseline correction technique to output from the SHAKE analysis.

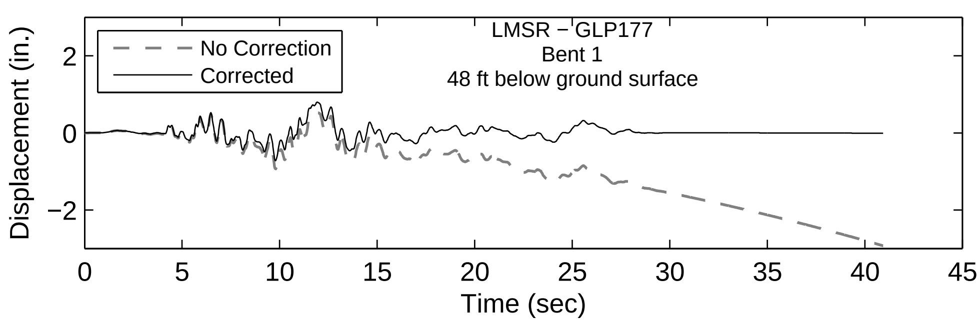

Fig. 4.11 Effect of baseline correction on displacement time histories determined using acceleration output from SHAKE analysis.

4.4 DESCRIPTION OF SIMULATION MODEL OF PROTOTYPE BRIDGE SYSTEM

Simulations of the prototype bridge system using OpenSees (McKenna et al., 2000) provide insight into the sensitivity of the structural response to modeling assumptions when considering SFSI. The simulations incorporate different boundary conditions and site effects to determine the variation of structural response at the global and local levels. The following describes the assumptions for four different prototype models: fixed base, fixed base at two column diameters below the ground surface, and sites with sand only and clay overlying sand. Large-scale parameter studies of these four prototype bridge systems are performed in Chapter 5 to determine the influence of SFSI on the structural response.

4.4.1 Material and Column Modeling

The material properties for steel and concrete are the same as those used in the four-span bridge model as described in Section 3.3.1. Concrete is modeled using the Concrete02 uniaxial material and steel is modeled using the Hysteretic uniaxial material. The column models include the beamWithHinges element with a plastic hinge integration method developed by Scott and Fenves (Scott and Fenves, 2006). The element algorithm is modified to revert to a noniterative scheme developed by Neuenhofer and Filippou (1997) in the case of no convergence as discussed in Appendix B. The fixed plastic hinge length is defined using the Priestley (Priestley et al., 1996) relationship as described in Section 3.3.2. The column longitudinal reinforcement ratio is 1.56% and the transverse reinforcement ratio is 0.9% as for the two-span and four-span tests. A 3-in. concrete cover is provided for the prototype column section. Using the same cross-section discretization as in the two-span and four-span bridge models, the moment-curvature response is as shown in Figure 4.12. The elastic portion of the column element has an effective stiffness equal to $M_y/\kappa_y = 0.38EI_g$ found from the moment-curvature analysis of the cross-section. Elastic shear and torsion properties are incorporated with the section aggregator. The elastic torsional stiffness is 20% of the gross torsional stiffness following recommendations by Caltrans (2004). The PDelta geometric transformation includes second-order effects for the columns. Different column lengths depending on the assumed boundary conditions give different plastic hinge lengths as listed in Table 4.11. For the simulation models that consider explicit representation of the soil response, the column heights are the same as in the fixed-base case.

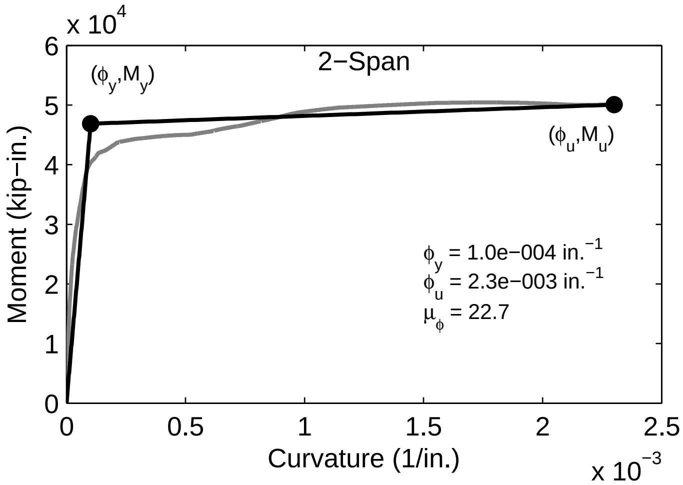

Fig. 4.12 Moment-curvature analysis of reinforced concrete circular column section used in the prototype bridge. Bilinear approximation is determined for the purpose of computing curvature ductility.

Table 4.11 Column and plastic hinge lengths for prototype model.

	Column Length (ft)			Plastic Hinge Length (in.)		
	Bent 1	Bent 2	Bent 3	Bent 1	Bent 2	Bent 3
Fixed Base	12	24	16	19.3	25.0	21.2
Fixed at 2D	20	32	24	23.1	28.9	25.0

4.4.2 Bent Cap and Superstructure

The bent cap geometry is scaled from that used in the two-span bridge. A reduction factor of 0.75 is applied to the flexural stiffness of the elastic beam-column elements used to model these members. The post-tensioned box girder deck has the cross-sectional geometry shown in Section 4.2. Outer span lengths are 1177 in. and inner span lengths are 1392 in. using a length scale factor of four applied to the dimensions of the four-span bridge. Each span is discretized into ten elastic beam-column elements.

4.4.3 Mass and Damping

Point masses associated with the dead load of the deck, cap beams, columns, and drilled shafts are applied at the nodes. From a gravity analysis of the structure, the axial load ratios, P/f_cA, are 5.7%, 5.7%, and 5.3% in bents 1, 2, and 3, respectively. The model is damped with Rayleigh damping at 2% using the last-committed stiffness. The selected damping ratio matches that determined from system identification of the two-span bridge (Ranf, 2007). Additional damping is included in the determination of the free-field motions from site response analysis using SHAKE.

4.4.4 Abutments

High-fidelity abutment models are essential when assessing the seismic behavior of bridges, since they limit displacements and transfer forces from the bridge deck to the approach embankment. While developing nonlinear analysis guidelines for the seismic response of bridges, Aviram et al. (2008b) investigated a hierarchy of complexity for modeling abutments. Nonlinear dynamic analysis of bridges warrants more sophisticated abutment models, particularly for short bridges with relatively stiff decks, since a higher level of complexity significantly impacts the predicted peak deformations for the structure (Aviram et al., 2008a). The modeling approach utilized in this research includes the consideration of passive soil resistance at the backwall and wingwalls, resistance from the bearing pads and shear keys, and inertia associated with the participating mass. Figure 4.13 depicts the adopted scheme for modeling the force-deformation response at the bridge ends.

The longitudinal response considers the bearing pad in series with the passive soil resistance at the backwall. As part of a companion study, Wilson and Elgamal investigated the static and dynamic response of an abutment-backfill system (Wilson and Elgamal, 2008). A 5.5-ft sacrificial backwall supporting well-graded sand in a laminar box was tested on the outdoor shake table at UCSD. Using the test results, they proposed abutment models capable of tracking the longitudinal force-displacement response of the abutment-backfill system. The backbone curve follows a hyperbolic relationship developed previously by Shamsabadi et al. (2007):

$$F(x) = \frac{x}{\frac{1}{K_{max}} + R_f \frac{x}{F_{ult}}} \tag{4.4}$$

where $F(x)$ is the passive soil resistance as a function of longitudinal displacement, x, F_{ult} is

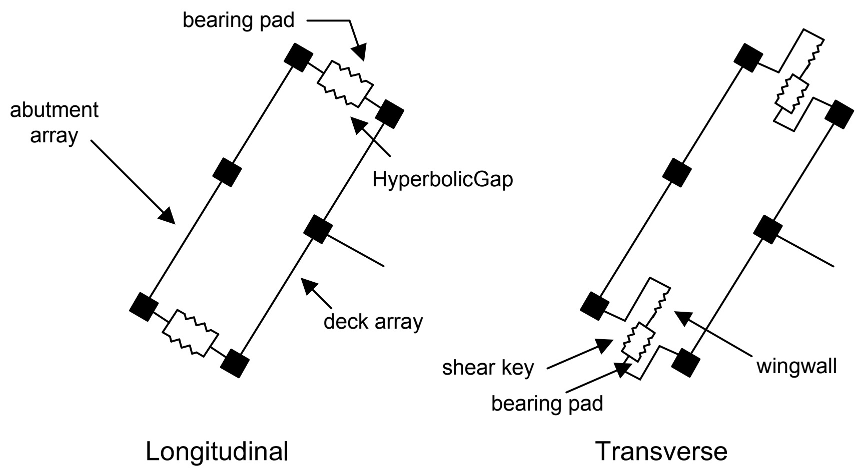

Fig. 4.13 Schematic of abutment model.

the ultimate resistance, K_{max} is the initial tangent stiffness, and R_f is the failure ratio. Wilson and Elgamal (2008) developed calibrated abutment models to match the experimental results. The selected parameters for the abutment model are K_{max} = 3.1 kip/in. per in. of abutment width, F_{ult} = 2.0 kip per in. of abutment width, and R_f = 0.7 assuming that the longitudinal displacement does not exceed 3 in. During unloading and reloading, the stiffness is the same as the initial tangent stiffness.

To calibrate the abutment response in the prototype bridge model to the experimental results described above, a HyperbolicGapMaterial object is added to the uniaxialMaterial class in OpenSees (McKenna et al., 2000). The abutment backwall in the prototype bridge model is 5.5-ft tall and 30-ft wide. Bearing pads with a height of 2 in. and total horizontal area of 20 in. by 30 in. support the bridge deck. The lateral stiffness for the rubber pads is $k_{lat} = GA/h$, where the shear modulus, G, is 150 psi. A Steel01 material model with yield displacement corresponding to 150% shear strain and strain-hardening ratio of 0.001 tracks the hysteretic response of the bearing pads. Figure 4.14 illustrates the hysteretic response of the abutment model for displacement in the longitudinal direction.

The transverse response of the abutment model includes consideration of the passive soil resistance at the wingwalls, and resistance from the bearing pads and shear keys as shown in Figure 4.13. The wingwalls have length equal to one third that of the backwall and lateral stiffness equal to 20 kip/in./ft following Caltrans recommendations for the initial embankment fill stiffness

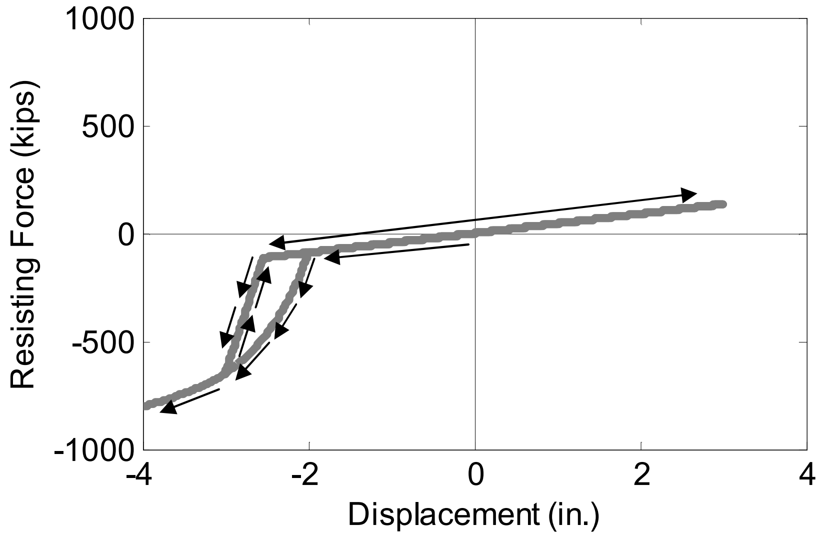

Fig. 4.14 Longitudinal force-deformation response of abutment model.

(Caltrans, 2004). The ultimate resistance of F_{ult} = 2.0 kip per in. of wall width is assumed for the wingwall as with the backwall. A Steel01 material model with strain-hardening ratio of 0.001 captures the hysteretic response associated with the passive soil resistance from the backfill at the wingwalls.

Exterior shear keys constrain the displacement at the bridge ends in the transverse direction. Static cyclic tests performed at the University of California, San Diego, determined the force-displacement response of these sacrificial elements (Bozorgzadeh et al., 2006). For the purposes of this study, the dimensions of the shear keys are selected from test series 5 of the UCSD tests (Bozorgzadeh et al., 2006). The force-displacement response of the shear key model follows the recommendations for nonlinear analysis of bridges developed by Aviram et al. (2008b). This model incorporates an initial stiffness that consists of the shear and flexural response of the shear key in series followed by hardening and softening regions that have a stiffness equal to 2.5% that of the initial stiffness. The ultimate resistance of the shear keys is 30% of the axial dead load reaction at the abutment as recommended by Caltrans (2004). The force-displacement response of the abutment model for motion in the transverse direction is shown in Figure 4.15. Elastic springs with stiffness EA/h, where E is 5.0 ksi, are used to model the vertical response of the bearing pads.

To account for the inertia associated with the abutment-embankment system, a participating

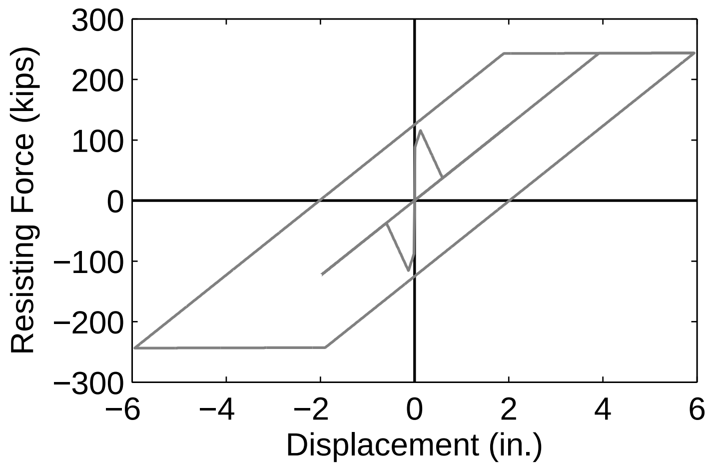

Fig. 4.15 Transverse force-displacement response of abutment model.

mass is incorporated along the abutment array. The participating mass includes the mass of the backwall, wingwalls, and mobilized backfill. Sextos et al. (2008) listed geometries for abutment-embankment systems of six typical California bridges. This study assumes an embankment height of 13.2 ft, a crest width of 30 ft, with slope equal to 0.5. Using the relationship developed by Zhang and Makris (2001) the critical length associated with the mobilized backfill during shaking is:

$$L_c = 0.7\sqrt{SB_cH} \tag{4.5}$$

where L_c is the critical length, S is the slope, B_c is the crest width, and H is the embankment height. Assuming the backwall and wingwalls have widths of 1 ft, the computed total participating mass at each abutment is 962 kips/g.

4.4.5 Soil-Pile Interaction

Cast-in-drilled-hole shafts provide the side friction and tip resistance required to support the prototype bridge columns and superstructure. The embedment lengths for the drilled shafts are 50.8 ft, 38.8 ft, and 46.8 ft beneath bents 1, 2, and 3, respectively. The drilled shafts are modeled using nonlinearBeamColumn elements with four-point Gauss-Lobatto quadrature and lengths of 4 ft. To model soil-pile-structure interaction, several researchers have proposed the method of a beam on a nonlinear Winkler foundation (BNWF) (Boulanger et al., 1999; Hutchinson et al., 2004; Brandenberg et al., 2007). The free-field soil displacement time histories determined from the SHAKE analyses are input to nonlinear p-y elements connected to the pile nodes. The p-y elements are modeled using the PySimple1 material in OpenSees which is discussed in detail by Boulanger et al. (1999). Material properties for the PySimple1 material for sand are selected to correspond to the API guidelines for nonliquefied sand (American Petroleum Institute, 1993). Figure 4.16 illustrates the agreement between the backbone curve of the PySimple1 material with the API relationship.

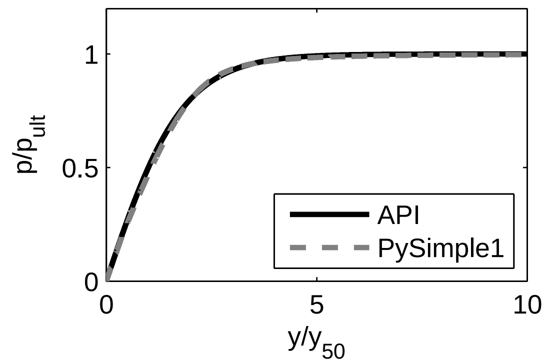

Fig. 4.16 Comparison of PySimple1 material for sand with API relationship.

The soil properties used to compute the ultimate resistance of the p-y curves for sand were described in Section 4.3.2. Since the API guidelines were developed for design against storm wave loading conditions for offshore structures (Lam et al., 1998), several modifications are made to adapt these relationships to the modeling of drilled shaft foundations for bridge columns. Given that the API p-y criteria were based on pile load tests using 24-in.-diameter piles, tests of large diameter shafts have found that these piles have significantly higher resistance due to diameter effects (Applied Technology Council, 1996). The ATC-32 guidelines suggest that the subgrade reaction stiffness be increased in linear proportion to the pile diameter for pile diameters exceeding two feet (Applied Technology Council, 1996). The API guidelines assume that subgrade reaction stiffness increases linearly with depth; however, the elastic modulus of sand approximately increases with the square root of confining stress (Brandenberg et al., 2007). To account for the depth effect, researchers have proposed a correction factor that assumes the API subgrade stiffness corresponds to a reference vertical stress of 50 kPa and is proportional to the square root of vertical effective stress (Brandenberg, 2005). The subgrade reaction stiffness, k, is then given as:

$$k = \frac{D_{pile}}{24}\sqrt{\frac{\sigma'_{ref}}{\sigma'_v}}k_{API} \tag{4.6}$$

where D_{pile} is the diameter of the drilled shaft in in., σ'_{ref} is the reference vertical stress equal to 50 kPa, σ'_v is the effective vertical stress at the soil spring under consideration, and k_{API} is the subgrade reaction stiffness from the API relationships. The parameters for the PySimple1 material used in the sand profile of the prototype bridge model are listed in Table 4.12.

Table 4.12 Parameters for p-y springs for sand profile.

Bent 1			Bent 2			Bent 3		
Depth (ft)	p_{ult} (kips)	y_{50} (in.)	Depth (ft)	p_{ult} (kips)	y_{50} (in.)	Depth (ft)	p_{ult} (kips)	y_{50} (in.)
0.0	4.1	0.012	0.0	2.2	0.005	0.0	4.1	0.012
4.0	53.0	0.039	4.0	28.8	0.016	4.0	53.0	0.039
8.0	160.4	0.083	8.0	87.1	0.033	8.0	160.4	0.083
12.0	322.2	0.136	12.0	174.9	0.054	12.0	273.1	0.085
16.0	476.7	0.129	16.0	292.2	0.079	16.0	415.2	0.112
20.0	660.8	0.159	20.0	439.0	0.106	20.0	586.9	0.142
24.0	874.4	0.192	24.0	615.3	0.135	24.0	788.0	0.173
28.0	1117.5	0.228	28.0	821.1	0.167	28.0	1018.7	0.208
32.0	1390.0	0.265	32.0	1056.4	0.201	32.0	1278.8	0.244
36.0	1692.1	0.304	36.0	1123.1	0.237	36.0	1568.5	0.282
40.0	2023.7	0.345	38.8	533.7	0.264	40.0	1887.7	0.322
44.0	2384.8	0.388				44.0	1900.9	0.364
48.0	2359.1	0.432				46.8	874.6	0.394
50.8	1073.6	0.464						

The side friction along the drilled shaft foundations is represented with the use of t-z springs following the modeling procedure used by Brandenberg et al. (2007). The ultimate capacity, t_{ult}, in units of force/length is:

$$t_{ult} = k_0 \sigma'_v p \tan\delta \tag{4.7}$$

where k_0=0.6 is the lateral earth pressure coefficient, σ'_v is the vertical effective stress at the soil spring under consideration, p is the perimeter of the drilled shaft, and δ is the interface friction angle between the pile and soil and is taken to be equal to ϕ'. At displacements equal to 0.5%

of the pile diameter, the resistance reaches the ultimate capacity, t_{ult}. The parameters for the TzSimple1 material used in the sand profile of the prototype bridge model are listed in Table 4.13.

Table 4.13 Parameters for t-z springs for sand profile.

Bent 1			Bent 2			Bent 3		
Depth (ft)	t_{ult} (kips)	z_{50} (in.)	Depth (ft)	t_{ult} (kips)	z_{50} (in.)	Depth (ft)	t_{ult} (kips)	z_{50} (in.)
0.0	1.4	0.03	0.0	0.7	0.03	0.0	1.4	0.03
4.0	10.8	0.03	4.0	5.9	0.03	4.0	10.8	0.03
8.0	21.6	0.03	8.0	11.7	0.03	8.0	21.6	0.03
12.0	32.5	0.03	12.0	17.6	0.03	12.0	27.5	0.03
16.0	38.3	0.03	16.0	23.5	0.03	16.0	33.4	0.03
20.0	44.2	0.03	20.0	29.4	0.03	20.0	39.3	0.03
24.0	50.1	0.03	24.0	35.2	0.03	24.0	45.1	0.03
28.0	55.9	0.03	28.0	41.1	0.03	28.0	51.0	0.03
32.0	61.8	0.03	32.0	47.0	0.03	32.0	56.9	0.03
36.0	67.7	0.03	36.0	44.9	0.03	36.0	62.7	0.03
40.0	73.6	0.03				40.0	68.6	0.03
44.0	79.4	0.03				44.0	63.3	0.03
48.0	72.5	0.03						

The end bearing resistance at the tip of the drilled shaft foundations is represented with the use of q-z springs following the modeling procedure used by Brandenberg et al. (2007). The ultimate capacity, q_{ult}, is determined using the recommendations by Meyerhof (1976). The unit point resistance, q_p, is:

$$q_p = \sigma'_v N_q \leq q_l \tag{4.8}$$

where N_q is the bearing capacity factor with respect to the effective overburden pressure, σ'_v, and q_l is the limiting unit point resistance determined from the critical depth penetration of the pile. The ultimate capacity, q_{ult}, is then:

$$q_{ult} = q_p \frac{\pi D_{pile}^2}{4} \tag{4.9}$$

At displacements equal to 5% of the pile diameter, the resistance reaches the ultimate capacity, q_{ult}. The parameters for the QzSimple1 material used in the sand profile of the prototype bridge model are listed in Table 4.14.

Table 4.14 Parameters for q-z springs for sand profile.

Bent 1			Bent 2			Bent 3		
Depth (ft)	q_{ult} (kips)	z_{50} (in.)	Depth (ft)	q_{ult} (kips)	z_{50} (in.)	Depth (ft)	q_{ult} (kips)	z_{50} (in.)
50.8	9890.1	0.15	38.8	6301.1	0.15	46.8	8693.7	0.15

The soil properties used to compute the ultimate resistance of the p-y curves for clay follow the API criteria (American Petroleum Institute, 1993) and for clarity, the following details the equations for these parameters using the discussion in the study by Boulanger et al. (1999). The ultimate capacity, p_{ult}, in units of force/length is:

$$p_{ult} = c_u D_{pile} N_p \tag{4.10}$$

where N_p is:

$$N_p = (3 + \frac{\gamma' x}{c_u} + \frac{Jx}{D_{pile}}) \leq 9 \tag{4.11}$$

where x is depth and J is taken as 0.5. The displacement at 50% of the ultimate resistance is:

$$y_{50} = 2.5 D_{pile} \epsilon_{50} \tag{4.12}$$

where ϵ_{50} = 0.005 for a 4-ft diameter shaft according to the recommendations by ATC-32 (Applied Technology Council, 1996). The parameters for the PySimple1 material used in the clay over sand profile of the prototype bridge model are listed in Table 4.15. The side friction along the drilled shaft foundations for the clay profile is represented with the use of t-z springs. The ultimate capacity, t_{ult}, in units of force/length is:

$$t_{ult} = \alpha c_u p \tag{4.13}$$

where c_u is the soil shear strength given by Equation 4.2, and p is the perimeter of the drilled shaft, and using the API criteria (American Petroleum Institute, 1993), α is:

$$\alpha = 0.5\psi^{-0.5}, \psi \leq 1.0 \tag{4.14}$$
$$\alpha = 0.5\psi^{-0.25}, \psi > 1.0$$

where ψ = c_u/σ'_v. The parameters for the TzSimple1 material used in the clay profile of the prototype bridge model are listed in Table 4.16. The end bearing resistance for the clay over sand

Table 4.15 Parameters for p-y springs for clay over sand profile.

Depth	p_{ult} (kips)			y_{50}
(ft)	Bent 1	Bent 2	Bent 3	(in.)
0.0	6.0	2.5	6.0	0.6
4.0	52.6	21.7	52.6	0.6
8.0	118.4	48.9	118.4	0.6
12.0	197.4	81.5	158.8	0.6
16.0	247.2	119.6	204.6	0.6
20.0	302.3	163.2	255.9	0.6
24.0	362.9	212.2	312.7	0.6
28.0	429.0	266.6	374.9	0.6
32.0	500.5	326.5	442.5	0.6
36.0	577.5	333.1	515.6	0.6
40.0	660.0	154.4	594.2	0.6
44.0	747.8		576.5	0.6
48.0	678.5		249.8	0.6
50.8	291.4			0.6

Table 4.16 Parameters for t-z springs for clay over sand profile.

Depth	t_{ult} (kips)			z_{50}
(ft)	Bent 1	Bent 2	Bent 3	(in.)
0.0	2.2	0.9	2.2	0.03
4.0	17.3	7.1	17.3	0.03
8.0	34.6	14.3	34.6	0.03
12.0	51.9	21.4	41.8	0.03
16.0	59.1	28.6	48.9	0.03
20.0	66.2	35.7	56.1	0.03
24.0	73.4	42.9	63.2	0.03
28.0	80.5	50.0	70.3	0.03
32.0	87.7	57.2	77.5	0.03
36.0	94.8	54.7	84.6	0.03
40.0	101.9		91.8	0.03
44.0	109.1		84.1	0.03
48.0	98.8			0.03

profile follows Equation 4.8. Differences between the tip resistance in this profile versus the sand profile occur, since the overburden pressures are not the same. The parameters for the QzSimple1 material used in the clay over sand profile of the prototype bridge model are listed in Table 4.17.

Table 4.17 Parameters for q-z springs for clay over sand profile.

Bent 1			Bent 2			Bent 3		
Depth (ft)	q_{ult} (kips)	z_{50} (in.)	Depth (ft)	q_{ult} (kips)	z_{50} (in.)	Depth (ft)	q_{ult} (kips)	z_{50} (in.)
50.8	5421.5	0.15	38.8	4028.4	0.15	46.8	4957.1	0.15

Figure 4.17 compares the response of the soil springs for both sand and clay. For the purposes of this analysis, no radiation damping effects have been included. Kinematic interaction for large diameter drilled shaft foundations primarily effects the high-frequency response of the bridge which is of minor significance (Fenves and Ellery, 1998). Gapping effects and soil liquefaction are also not considered in this study.

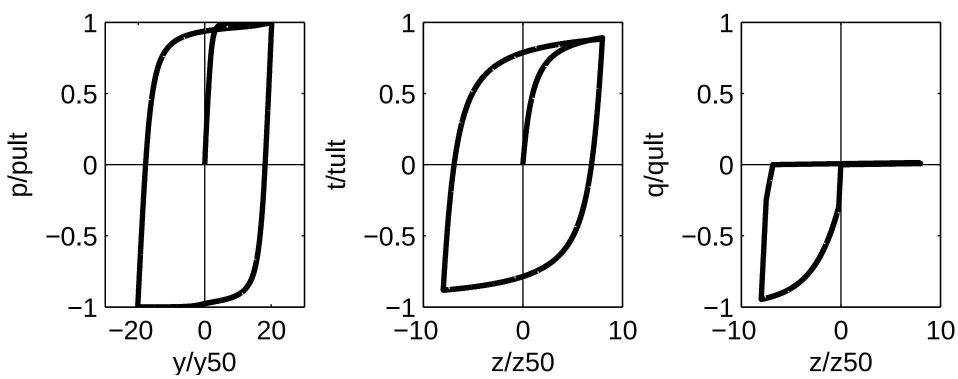

Fig. 4.17 Response of p-y, t-z, and q-z soil springs used in the prototype bridge model.

4.4.6 Solution Strategies

The analysis of the prototype bridge models proceeds in four stages: enforcement of single point constraints to fix the boundary nodes, application of gravity loads, removal of single point constraints, and imposition of free-field displacement time histories at the boundary nodes using the multiple support excitation command. Such a sequence is required, since the boundary nodes must have free degrees of freedom where the multiple support excitation is applied. A Penalty constraints handler with penalty values of 1e12 is used in conjunction with the multiple support excitation command. The Newmark average acceleration method is the time integration scheme used to discretize the system of ordinary differential equations. The Plain numberer orders the degrees of freedom and the ProfileSPD solver is used to obtain the solution. A normDispIncr convergence test with a tolerance of 1.0e-7 and maximum number of iterations equal to 20 is selected, since the penalty constraints handler can potentially lead to large norms of the residual unbalanced force. The Newton algorithm solves for the displacement increment at each time step. In the event that convergence is not achieved, the input script is modified as shown in Appendix B to obtain convergence. Initial analysis time steps equal to 0.005 sec were reduced to as small as 0.001 sec in some cases to achieve a converged solution.

4.5 CONCLUSIONS

This chapter details the development of simulation models for the seismic performance of a prototype bridge system with varying boundary conditions and soil profiles. The prototype bridge design builds upon the assumptions considered for the prototype bridges that served as the basis for the design of the two-span and four-span bridges. Site response analysis performed for a suite of ground motions provides the free-field ground motions when the soil response is modeled explicitly. Soil springs along the length of the drilled shaft foundations model the soil-pile-interaction for both sandy and clayey soils. The abutment model incorporates the results of full-scale experimental tests conducted as part of a companion study. The prototype bridge models provide the means to assess the variation of structural response for a range of soil-foundation-structure interaction through large-scale parameter studies described in the following chapter.

5 Evaluation of SFSI in the Seismic Response of a Reinforced Concrete Bridge System

5.1 INTRODUCTION

This chapter presents an investigation of the sensitivity of the seismic response of a reinforced concrete prototype bridge system to soil-foundation-structure interaction (SFSI). The first section discusses the background on performance-based simulation models for the seismic response of reinforced concrete bridges. The next section presents the simulation models that allow for a study of the effect of SFSI. Finally, the results for the prototype system are given within a performance-based engineering framework and conclusions are drawn regarding the impact of SFSI.

5.2 BACKGROUND

Probabilistic approaches assess the seismic response of reinforced concrete bridges within a performance-based engineering framework. Mackie and Stojadinovic (2003) performed extensive studies within this framework to quantify the relationship between intensity measures and engineering demand parameters for a range of prototype bridges designed for sites in California. This study was later extended to include the repair costs due to typical damage scenarios for bridges (Mackie et al., 2008). Similar research has considered the fragility of new and retrofitted bridges in the central and southeastern United States (Nielson, 2005; Padgett, 2007; Padgett and DesRoches, 2009). In such approaches, it is necessary to define a relationship between the intensity measure, an indicator of the intensity of the ground motion, and the engineering demand parameter, the response quantity of interest. The demand model used by Mackie and Stojadinovic (2003) lends itself to a linear regression of the form:

$$ln(EDP) = Aln(IM) + B \tag{5.1}$$

where EDP is the engineering demand parameter, IM is the intensity measure, and the constants A and B are determined from a linear regression of the data in log-log space. The dispersion, a measure of the randomness of the data, is computed using equation 5.2:

$$\sigma = \sqrt{\frac{\sum_{i=1}^{N}(ln(EDP_{i,fit}) - ln(EDP_i))^2}{n-1}} \tag{5.2}$$

where $EDP_{i,fit}$ and EDP_i are the values of the engineering demand parameter from the linear regression of the data and the simulation model, respectively, for ground motion i, and n is the number of ground motions (Mackie and Stojadinovic, 2003). Mackie classified models with dispersions from 0.20 to 0.30 as superior among the set of optimal models considered (Mackie and Stojadinovic, 2003). In this study, the dispersion is utilized to compare the variability of the data for the engineering demand parameters that are studied.

Since the dispersion is dependent on the scale of the engineering demand parameter, a dimensionless measure of goodness of fit is also considered. The coefficient of determination (Montgomery et al., 2007), R^2, is:

$$R^2 = 1 - \frac{\sum_{i=1}^{N}(ln(EDP_i) - ln(EDP_{i,fit}))^2}{\sum_{i=1}^{N}(ln(EDP_i) - ln(\overline{EDP}))^2} \tag{5.3}$$

where $\overline{EDP}$ is the geometric mean of the engineering demand parameter. The geometric mean of a variable, x, is defined by Shome (1999) as:

$$\hat{x} = exp[\frac{\sum_{i=1}^{N} ln(x_i)}{N}] \tag{5.4}$$

The range of the coefficient of determination is $0 \leq R^2 \leq 1$, where $R^2 = 1.0$ indicates that the model perfectly fits the data.

5.3 SIMULATION MODELS

To investigate the impact of SFSI on the seismic response of a reinforced concrete prototype bridge system, four different simulation models with varying boundary conditions are evaluated. These models are denoted as fixed base, fixed base at 2D, sand, and clay over sand. For the cases including soil, the soil profiles are not taken from a particular site, but rather a range of soil conditions is used to determine the variation of structural response at the global and local levels. All four simulation models orient the pairs of horizontal components for each ground motion such that the component corresponding to a larger outcrop peak ground acceleration is applied along the longitudinal direction of the bridge.

The fixed base model has clear column heights of 12 ft, 24 ft, and 16 ft for bents 1, 2, and 3, respectively. The fixed base at 2D model extends the column lengths by 8 ft, two column diameters, to where the point of fixity is assumed to occur for the prototype bridge. Each of the fixed-base models applies the outcrop ground motions at the base of the columns and at the abutments using the multiple support excitation command with imposed displacements.

The sand model idealizes the case for a site with a medium-dense Nevada sand. The clay over sand model has a soft clay that extends to the tip of the drilled shaft foundations and overlies sand that extends to bedrock. The models that include the soil response have soil springs along the length of the drilled shaft foundations with properties given in Section 4.4.5. Displacement time histories are imposed at the location of the soil springs and at the abutments using the multiple support excitation command. Site response analyses used to compute the input excitation were described in Section 4.3.2.

Modal analyses for each of the four prototype bridge models give the initial periods tabulated in Table 5.1. Figure 5.1 illustrates the first two mode shapes for the clay over sand model. The extension of the column length by two column diameters has a pronounced effect on the fixed-base model with the fundamental period increasing by more than 50%. For the cases where soil is explicitly modeled, the softer clay increases the system flexibility by more than 50% for the period associated with the longitudinal mode. For the purposes of comparison, the design periods for the prototype bridges used to develop similitude relationships for the shaking table tests are listed in Table 5.2. These design periods are much longer than for the fixed-base case, since they were calculated using the uniform load method and did not include transverse and longitudinal restraint at the abutments.

Table 5.1 Comparison of periods for prototype bridge models.

	Period (s)			
	Fixed Base	Fixed Base at 2D	Sand	Clay Over Sand
Longitudinal	0.38	0.58	0.52	0.80
Transverse	0.32	0.49	0.57	0.70

Table 5.2 Design periods for prototype bridges used in 2-span and 4-span tests (Johnson et al., 2006; Nelson et al., 2007).

	Period (s)	
	2-span	4-span
Longitudinal	0.748	1.34
Transverse	0.758	0.79

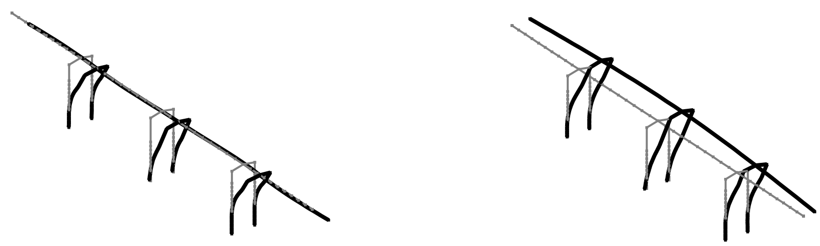

Fig. 5.1 Mode shapes for the prototype bridge model with Clay Over Sand soil profile.

5.4 PARAMETERIZATION OF SIMULATIONS

The scale of this simulation effort is significant and includes 1280 site response analyses computed using SHAKE and 320 nonlinear dynamic analyses performed with OpenSees. For the cases where soil is modeled explicitly, the simulation models have a total of 940 degrees of freedom. Because of the large computational effort required, the parallel capability of OpenSees version 2.0 was employed in this study (McKenna et al., 2000). The parameterization of the model enables execution of multiple parallel OpenSees interpreters with a different input ground motion for each instance of the interpreter. The functionality of OpenSeesMP, the multiple parallel OpenSees interpreter application, is described by McKenna and Fenves (2008). The commands, *getNP* and *getPID*, return the number of processors allocated to the user and the processor ID, respectively. The input script was modified for use on a parallel machine as shown in Table 5.3. In this case, a text file containing the indices from one to twenty was used to parameterize the model for the different ground motions in each of the four bins. Using an allocation granted by NEESit, the simulations were performed on the Intel 64 Cluster Abe at the National Center for Supercomputing Applications at the University of Illinois (National Center for Supercomputing Applications, 2009).

Table 5.3 OpenSees commands for parameter studies on a parallel computer.

```
set count 0
set pid [getPID]
set np [getNP]
set motionFile "/cfs/scratch/users/dryden/bin/iGM.txt"
set recordsFile [open $motionFile r]
foreach line [split [read $recordsFile] \n] {
 if {[expr $count % $np] == $pid} {
 set iGM [lindex $line 0]
 ...
 incr count 1
}
close $recordsFile
```

5.5 SIMULATION RESULTS

The results of the nonlinear dynamic analyses of the prototype bridge simulation models are presented in the following. First, the demand models are given to evaluate the SFSI effect on probabilistic approaches used within a performance-based framework. Then, two specific cases in which the SFSI effect causes either less or more yielding are discussed.

5.5.1 Development of Demand Models

The intensity measure (IM) selected to develop the demand models is the square-root-sum-of-squares (SRSS) of the horizontal components of the peak ground velocity (PGV) for each outcrop ground motion. This intensity measure is independent of the structural period and has been used in previous studies on the seismic response of bridges (Mackie et al., 2008; Aviram et al., 2008b). For reference, the values of the intensity measures for different hazard levels are given in Table 5.4. Peak ground accelerations (PGA) for each hazard level are determined using the USGS ground motion parameter calculator for a site at 33.60 degrees latitude, -117.45 degrees longitude, the site used in the prototype bridge design for the two-span and four-span experimental tests (Johnson et al., 2006; Nelson et al., 2007). This site is situated southeast of Los Angeles and was chosen because it was more than 10 km from a fault and produced a seismic demand that was approximately equivalent to the capacity for the selected column reinforcement of the two-span bridge (Johnson et al., 2006). Peak ground velocities for each hazard level are calculated using the relationship

PGV/PGA = 48 in./sec/g recommended by Newmark and Hall (1982). Typically, the relationship between the hazard level and the intensity measure is modeled using a power law (Mackie et al., 2008). Within a performance-based framework, the hazard levels may be used to establish the probabilities of exceedance for a given intensity measure that is used in the demand models developed subsequently.

Table 5.4 Values of intensity measure for different hazard levels.

Hazard Level	50% in 50 yrs	10% in 50 yrs	2% in 50 yrs
Return Period (yrs)	72	475	2475
PGA (g)	0.17	0.41	0.66
PGV (in./sec)	8.02	19.89	31.56

Linear regressions of the form given in Equation 5.1 are shown in Figures 5.2 through 5.5 for deformation response quantities of interest in design. The drift ratios for each bent are computed using the difference in displacements at the top of the bent and at the ground surface divided by the column length. In the cases where the soil response is incorporated, this drift ratio also includes displacement due to the rigid body rotation of the pile at ground surface. At the element and section levels, the maximum plastic rotations and curvatures, respectively, are determined within the set of all of the elements in a given bent. For drift ratios and curvatures, the maximum of the SRSS of these response quantities is plotted. The parameters for each of the demand models of the form given in Equation 5.1 are listed in Table 5.6.

The extent to which the linear regressions produce acceptable demand models is evaluated using the dispersion and the coefficient of determination. The dispersion values for each response quantity are tabulated in Table 5.7. Since the dispersion is scale dependent, it is useful as a measure of variability when evaluating the same response quantity. Greater variability exists at the global level for the fixed-base case than for the models including soil. Slightly greater scatter is evident for the cases with soil than the fixed-base model when evaluating the maximum curvature. No general trend in the variability of the maximum plastic rotations is apparent. The coefficient of determination provides more insight into the goodness of fit for the demand models. Table 5.8 lists the values of R^2 for each simulation model and engineering demand parameter. The demand models have slightly better fit for the maximum drift ratios than for the maximum curvatures and plastic rotations. At the global level, better fit occurs for the maximum drift ratios at bents 2 and 3, than at bent 1, the stiffest bent. For all engineering demand parameters, the simulation models including soil have demand models that are in greater agreement with the data than compared to the fixed-base case.

Soil-foundation-structure interaction clearly has a significant influence on the predicted maximum response quantities from the demand models for the prototype bridge system. As an illustration of this effect, the maximum response quantities for the largest value of the intensity measure, a PGV equal to 26.9 in./sec, are tabulated in Table 5.5. At the local level, the SFSI effect amplifies the predicted maximum curvatures at bents 1 and 3 by over 67% compared to the fixed-base case. At bent 1, the maximum plastic rotation about the longitudinal axis is 2.9 times greater when including SFSI than for the fixed-base model. These trends display the importance of considering SFSI when using demand models as a decision making tool in the design and assessment of reinforced concrete bridges.

Table 5.5 Response quantities at the maximum PGV from linear regressions.

		Simulation Model			
	Bent	Fixed Base	Fixed Base at 2D	Sand	Clay Over Sand
Max Drift Ratio (%)	1	1.28	2.83	3.24	3.23
	2	4.07	4.26	5.70	5.67
	3	6.15	6.29	8.37	8.60
ϕ_{max} (1/in.)	1	5.00e-4	6.35e-4	1.53e-3	1.53e-3
	2	1.29e-4	2.11e-4	5.87e-4	6.22e-4
	3	3.75e-4	4.94e-4	1.21e-3	1.29e-3
θ_{px} (rad)	1	5.53e-3	9.46e-3	2.18e-2	2.18e-2
	2	1.78e-3	4.13e-3	1.13e-2	1.20e-2
	3	5.83e-3	9.65e-3	2.06e-2	2.12e-2
θ_{py} (rad)	1	1.21e-2	1.64e-2	3.15e-2	3.06e-2
	2	2.99e-3	6.37e-3	1.47e-2	1.47e-2
	3	7.83e-3	1.23e-2	2.53e-2	2.56e-2

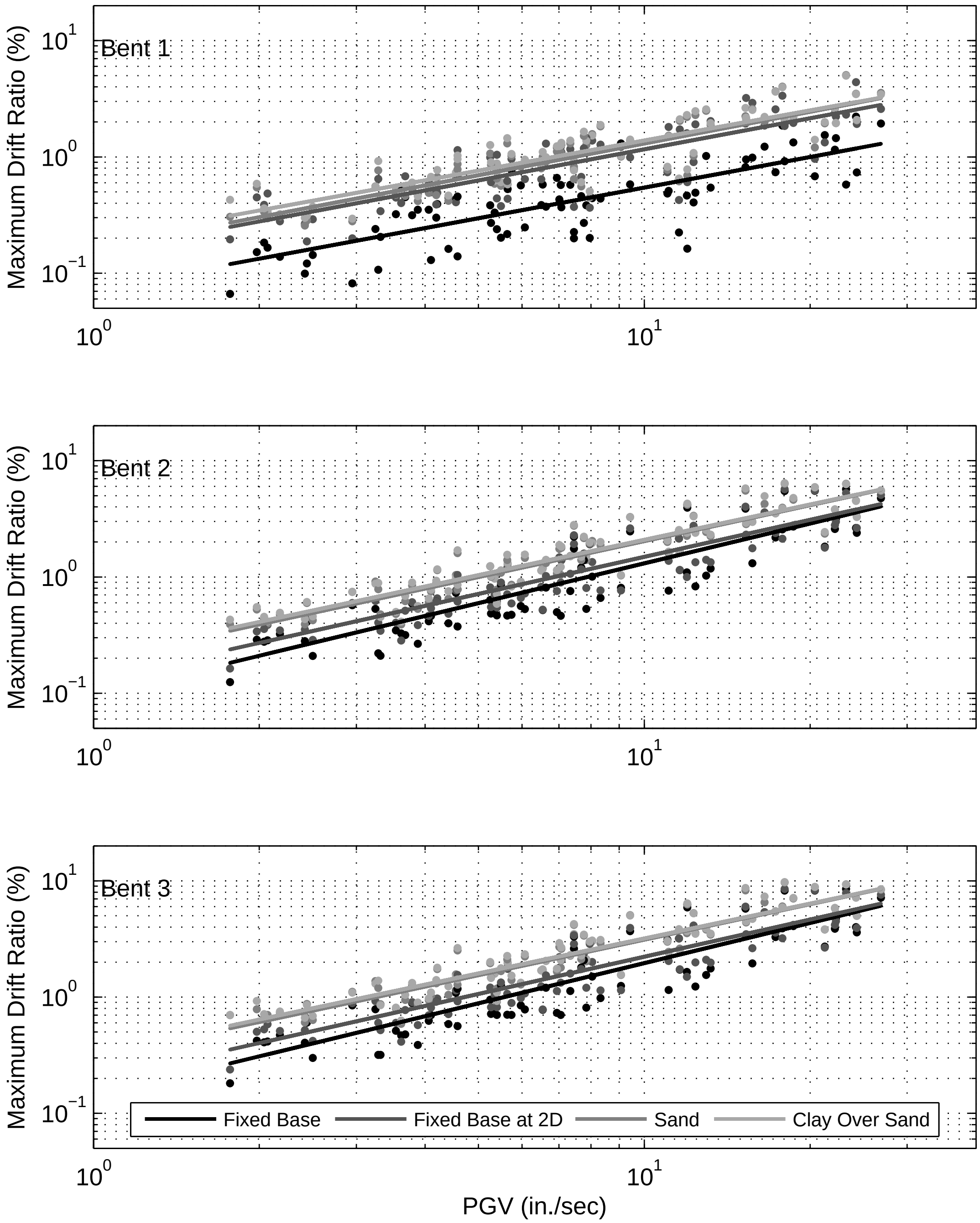

Fig. 5.2 Demand models for maximum drift ratios (%).

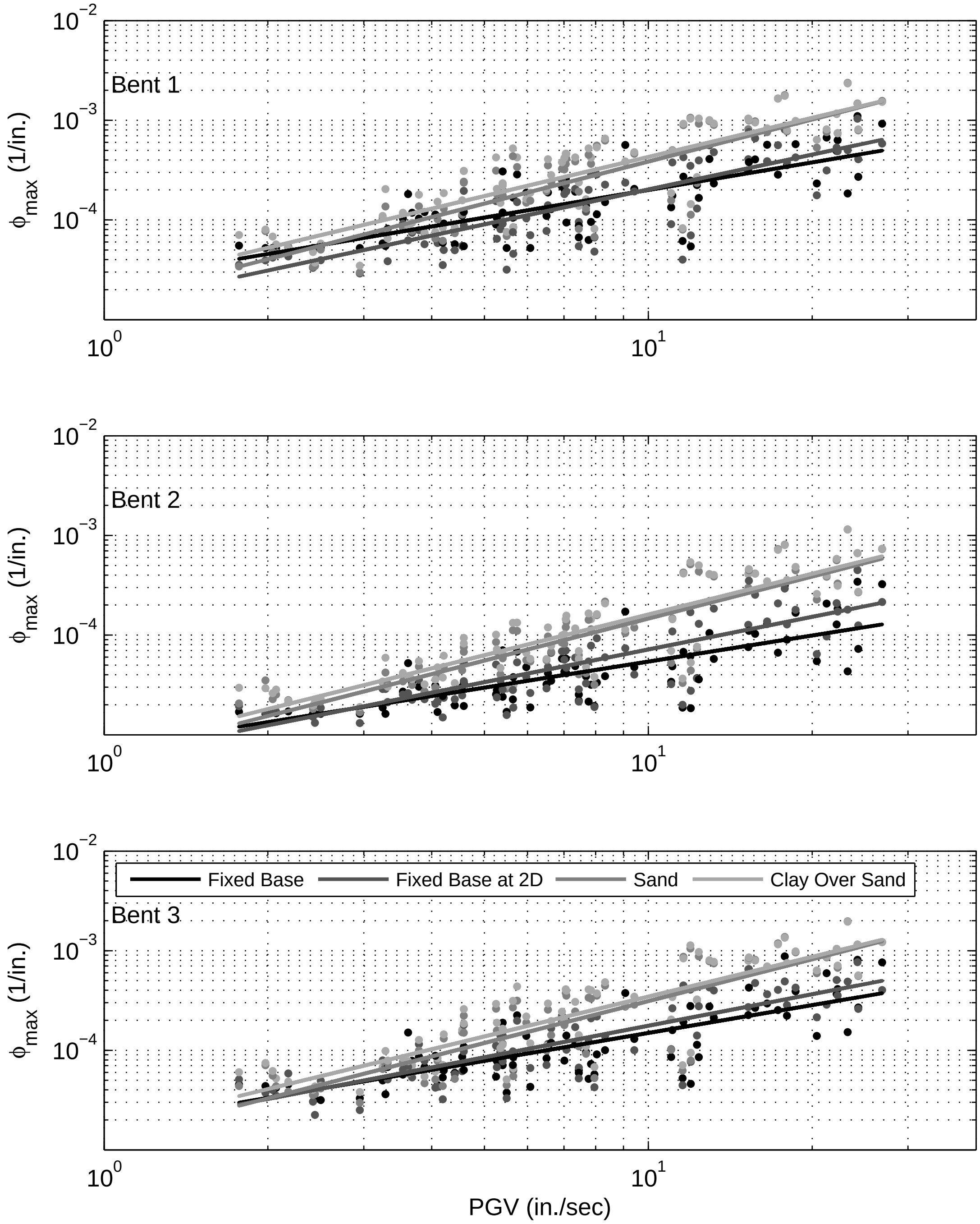

Fig. 5.3 Demand models for maximum curvatures (1/in.).

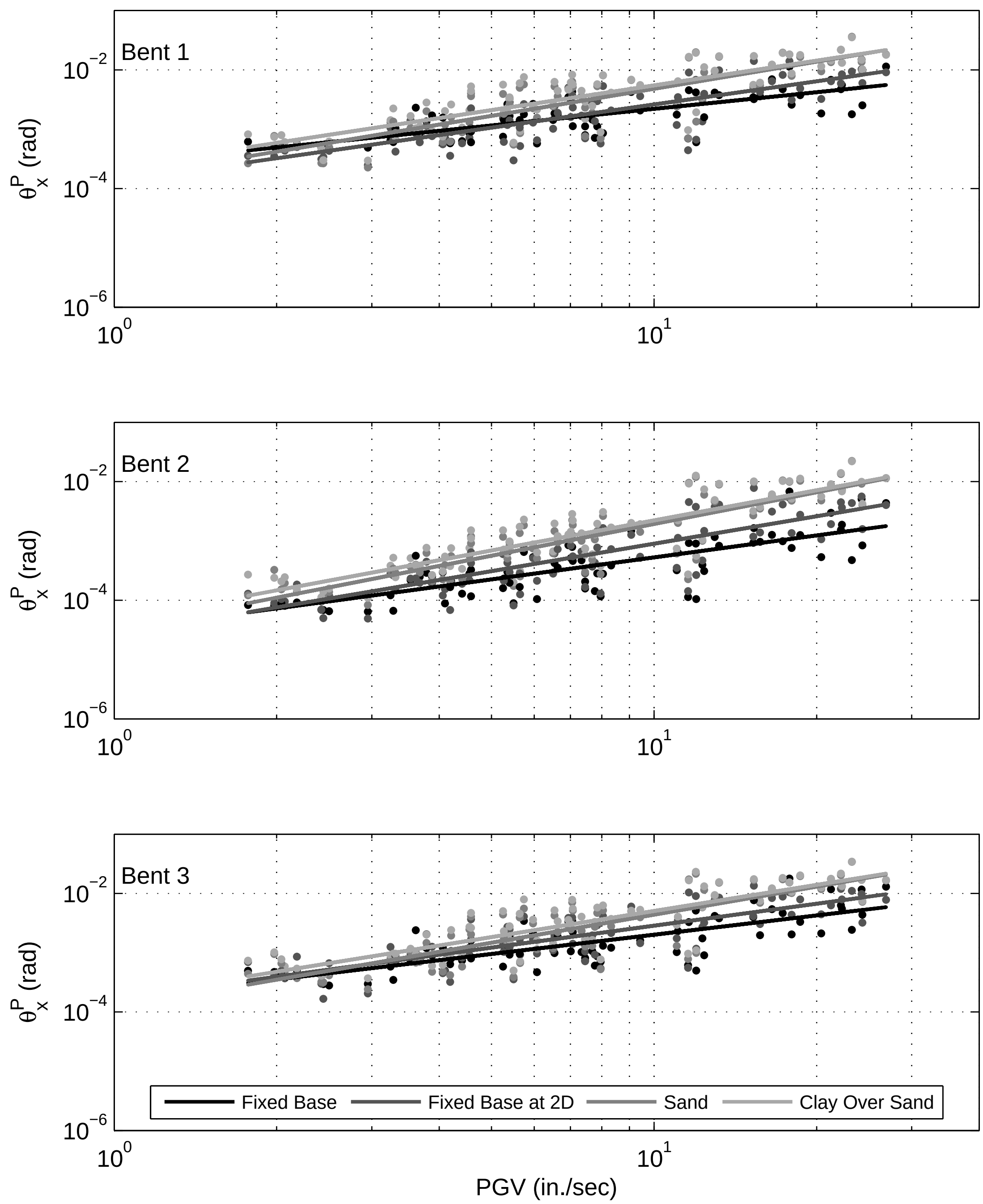

Fig. 5.4 Demand models for maximum plastic rotations (rad) about the longitudinal axis.

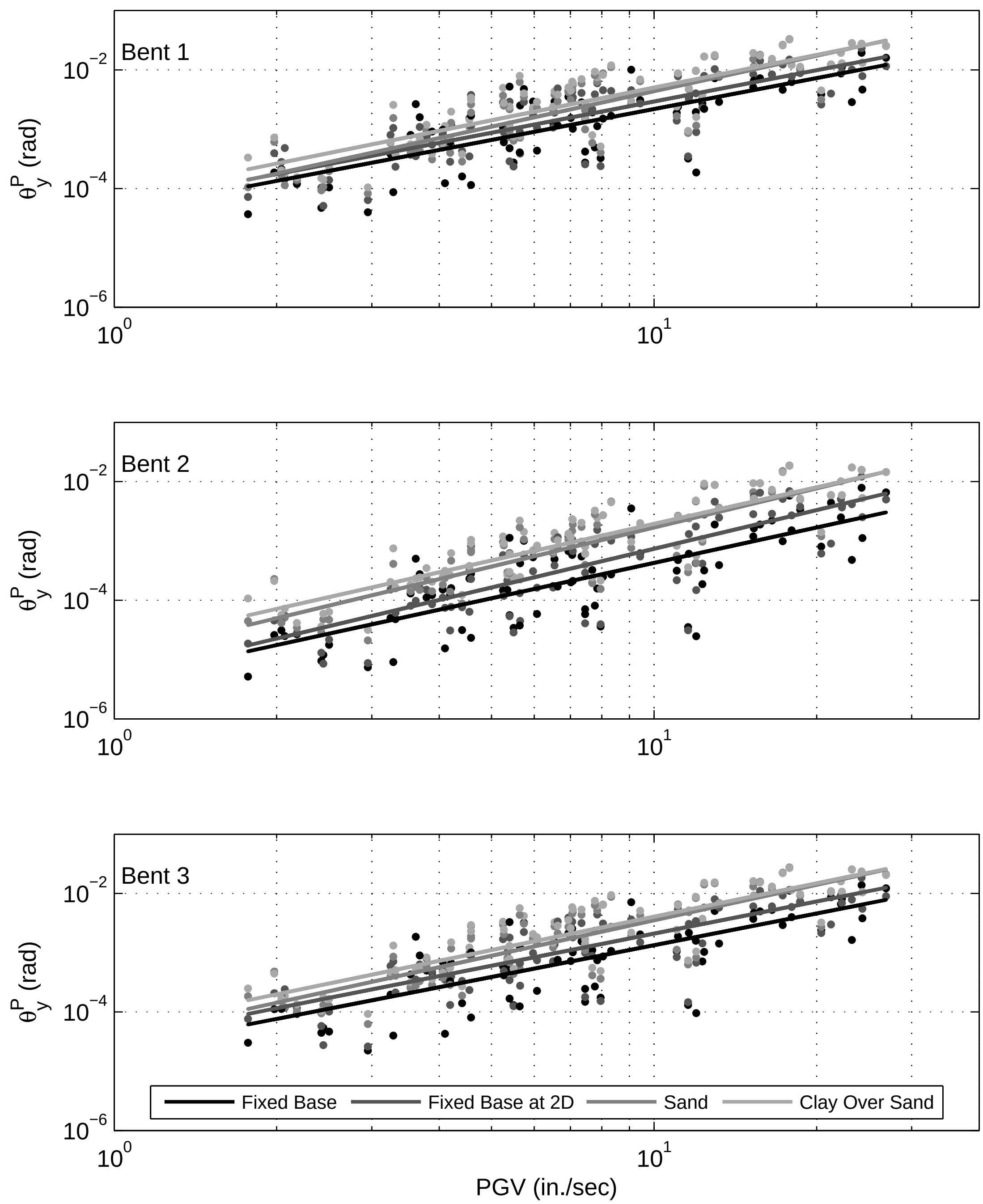

Fig. 5.5 Demand models for maximum plastic rotations (rad) about the transverse axis.

Table 5.6 Comparison of SFSI effect on parameters from demand models.

	Parameter Values for Maximum Drift Ratio Demand Models							
	Fixed Base		Fixed Base at 2D		Sand		Clay Over Sand	
	A	B	A	B	A	B	A	B
Bent 1	0.87	-2.62	0.89	-1.89	0.91	-1.82	0.86	-1.66
Bent 2	1.14	-2.35	1.06	-2.04	1.03	-1.65	1.01	-1.59
Bent 3	1.15	-1.97	1.06	-1.65	1.01	-1.20	1.00	-1.14

	Parameter Values for Maximum Curvature Demand Models							
	Fixed Base		Fixed Base at 2D		Sand		Clay Over Sand	
	A	B	A	B	A	B	A	B
Bent 1	0.92	-10.63	1.16	-11.18	1.40	-11.09	1.30	-10.76
Bent 2	0.87	-11.82	1.09	-12.05	1.40	-12.05	1.36	-11.86
Bent 3	0.93	-10.95	1.05	-11.07	1.39	-11.29	1.33	-11.03

	Parameter Values for θ_{px} Demand Models							
	Fixed Base		Fixed Base at 2D		Sand		Clay Over Sand	
	A	B	A	B	A	B	A	B
Bent 1	0.93	-8.26	1.30	-8.94	1.52	-8.83	1.39	-8.40
Bent 2	1.23	-10.38	1.54	-10.56	1.78	-10.34	1.69	-9.99
Bent 3	1.08	-8.70	1.23	-8.69	1.57	-9.05	1.46	-8.66

	Parameter Values for θ_{py} Demand Models							
	Fixed Base		Fixed Base at 2D		Sand		Clay Over Sand	
	A	B	A	B	A	B	A	B
Bent 1	1.73	-10.11	1.75	-9.87	1.99	-10.01	1.83	-9.51
Bent 2	1.98	-12.33	2.17	-12.20	2.19	-11.43	2.05	-10.97
Bent 3	1.78	-10.71	1.80	-10.32	1.99	-10.23	1.87	-9.82

Table 5.7 Comparison of SFSI effect on dispersion values from demand models.

	Fixed Base	Fixed Base at 2D	Sand	Clay Over Sand
	Dispersion Values for Maximum Drift Ratio Demand Models			
Bent 1	0.47	0.40	0.34	0.33
Bent 2	0.42	0.35	0.29	0.29
Bent 3	0.42	0.35	0.28	0.29
	Dispersion Values for Maximum Curvature Demand Models			
	Fixed Base	Fixed Base at 2D	Sand	Clay Over Sand
Bent 1	0.51	0.54	0.57	0.56
Bent 2	0.49	0.51	0.55	0.53
Bent 3	0.50	0.50	0.58	0.55
	Dispersion Values for θ_{px} Demand Models			
	Fixed Base	Fixed Base at 2D	Sand	Clay Over Sand
Bent 1	0.55	0.64	0.67	0.64
Bent 2	0.67	0.73	0.71	0.68
Bent 3	0.61	0.64	0.70	0.65
	Dispersion Values for θ_{py} Demand Models			
	Fixed Base	Fixed Base at 2D	Sand	Clay Over Sand
Bent 1	0.95	0.86	0.81	0.78
Bent 2	1.09	1.04	0.81	0.79
Bent 3	1.02	0.91	0.80	0.76

Table 5.8 Comparison of SFSI effect on coefficient of determination from demand models.

	R^2 for Maximum Drift Ratio Demand Models			
	Fixed Base	Fixed Base at 2D	Sand	Clay Over Sand
Bent 1	0.63	0.71	0.78	0.77
Bent 2	0.78	0.82	0.86	0.85
Bent 3	0.79	0.82	0.86	0.86
	R^2 for Maximum Curvature Demand Models			
	Fixed Base	Fixed Base at 2D	Sand	Clay Over Sand
Bent 1	0.61	0.70	0.75	0.73
Bent 2	0.61	0.69	0.76	0.77
Bent 3	0.63	0.68	0.74	0.74
	R^2 for θ_{px} Demand Models			
	Fixed Base	Fixed Base at 2D	Sand	Clay Over Sand
Bent 1	0.58	0.67	0.72	0.70
Bent 2	0.63	0.68	0.75	0.75
Bent 3	0.60	0.64	0.71	0.71
	R^2 for θ_{py} Demand Models			
	Fixed Base	Fixed Base at 2D	Sand	Clay Over Sand
Bent 1	0.62	0.67	0.75	0.73
Bent 2	0.62	0.68	0.78	0.77
Bent 3	0.60	0.66	0.75	0.75

5.5.2 Deterministic Comparison of SFSI Effect

The extent to which the SFSI effect produces less or more yielding may best be observed on a case-by-case basis. Two ground motions were considered, one for which the SFSI effect caused less yielding, M-GMR000 (PGV = 3.62 in./sec), and the other for which the SFSI effect gave more yielding, HCH090 (PGV = 23.25 in./sec). Figures 5.6 and 5.7 compare the moment-curvature response at the top of a column in bent 1 for these ground motions, and Figures 5.8 and 5.9 plot the drift ratios at bent 1. The SFSI effect for each case is evident in the tabulated peak response quantities listed in Table 5.9. For the simulation models including soil, the maximum curvature is reduced by as much as 50% compared to the fixed-base model when SFSI effects less yielding. Where SFSI induces greater yielding, the maximum curvature is over 18 times greater than that determined from the fixed-base model.

To gain greater insight into these disparities, the response spectra for both ground motions are plotted in Figure 5.10. The spectral accelerations at the initial periods of each simulation model are plotted on the response spectra from the outcrop and surface motions for the cases including a fixed base and soil, respectively. In the case of greater yielding due to SFSI, the response spectra have much higher spectral acceleration values for periods at or exceeding the initial periods of the simulation models with soil. When SFSI introduces less yielding, the long-period range of the response spectra including soil falls sharply below the spectral acceleration at the initial period for the fixed-base model.

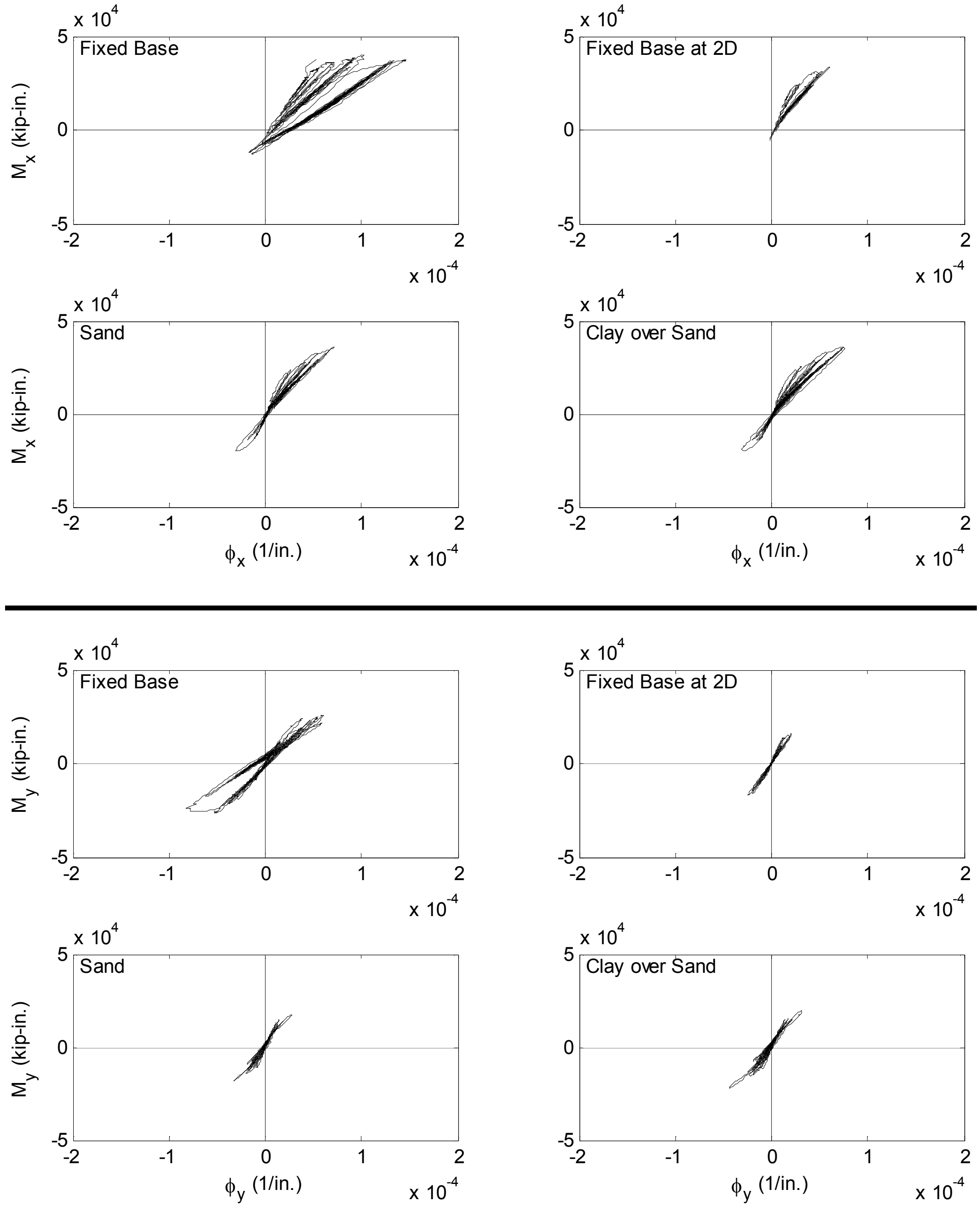

Fig. 5.6 Moment (kip-in.) versus curvature (1/in.) for the section at the top of one column in bent 1 during ground motion M-GMR000.

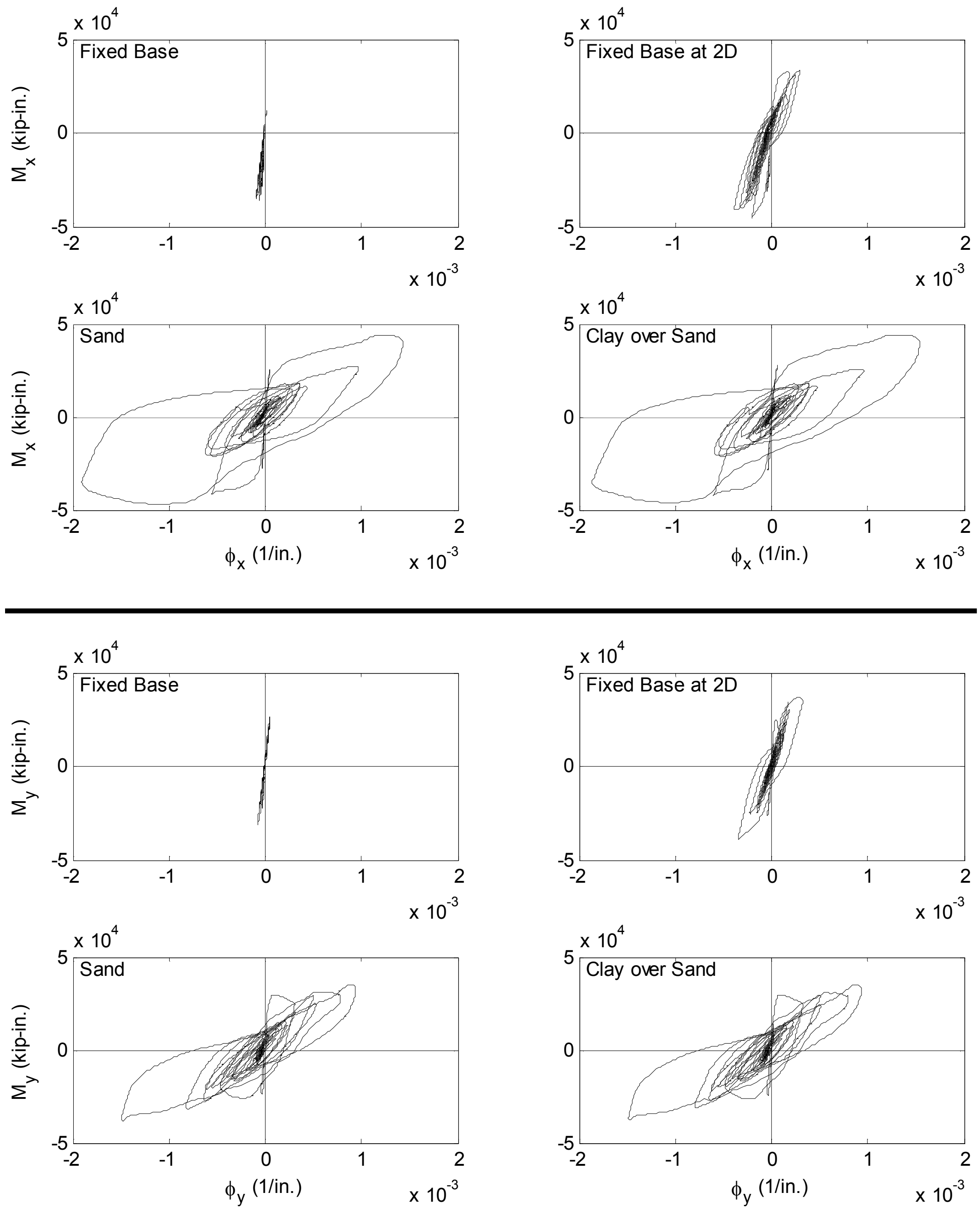

Fig. 5.7 Moment (kip-in.) versus curvature (1/in.) for the section at the top of one column in bent 1 during ground motion HCH090.

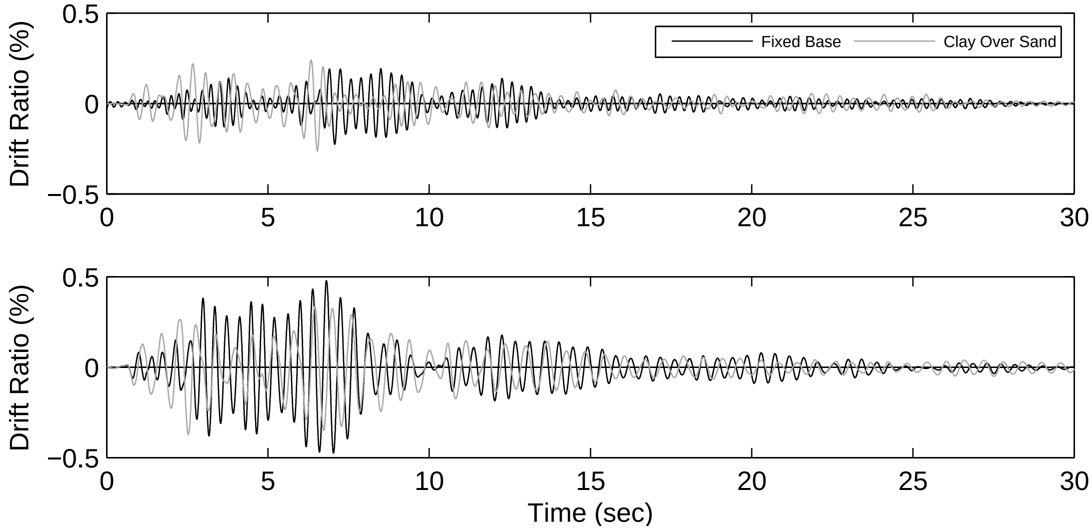

Fig. 5.8 Drift ratio (%) versus time (sec) for bent 1 during ground motion M-GMR000.

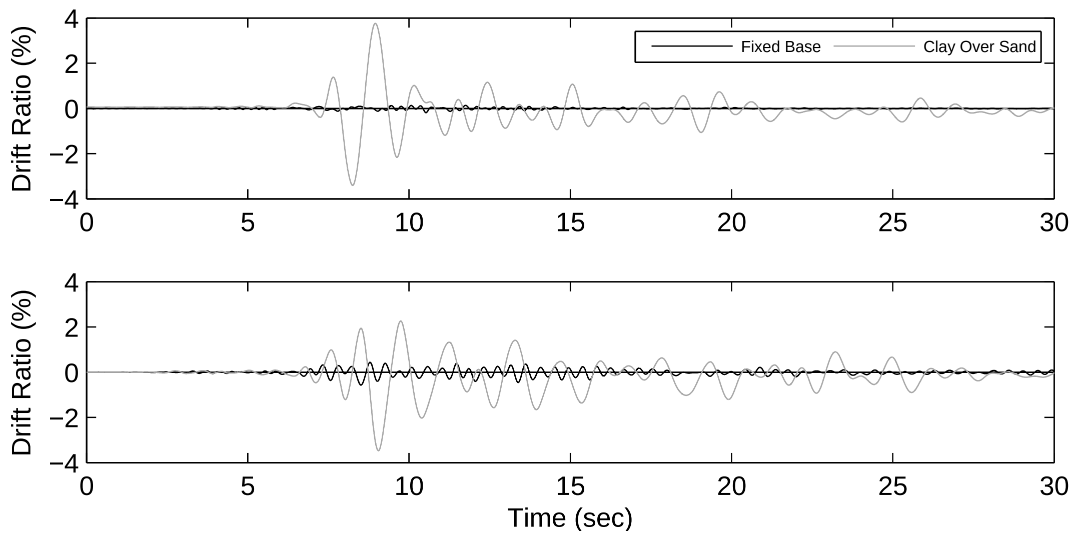

Fig. 5.9 Drift ratio (%) versus time (sec) for bent 1 during ground motion HCH090.

Table 5.9 Comparison of SFSI effect on response quantities for simulation models.

		Bent 1 Maximum Drift Ratio (%)			
Ground Motion	Direction	Fixed Base	Fixed Base at 2D	Sand	Clay Over Sand
M-GMR000	Longitudinal	0.48	0.37	0.34	0.41
	Transverse	0.23	0.26	0.39	0.39
HCH090	Longitudinal	0.57	2.15	3.49	3.47
	Transverse	0.19	1.75	3.85	3.76

		ϕ_{max} (1/in.) at Top of Column in Bent 1			
Ground Motion	Direction	Fixed Base	Fixed Base at 2D	Sand	Clay Over Sand
M-GMR000	Longitudinal	1.46e-4	6.08e-5	7.08e-5	7.65e-5
	Transverse	8.32e-5	2.43e-5	3.25e-5	4.42e-5
HCH090	Longitudinal	9.78e-5	3.84e-4	1.91e-3	1.86e-3
	Transverse	8.30e-5	3.46e-4	1.49e-3	1.49e-3

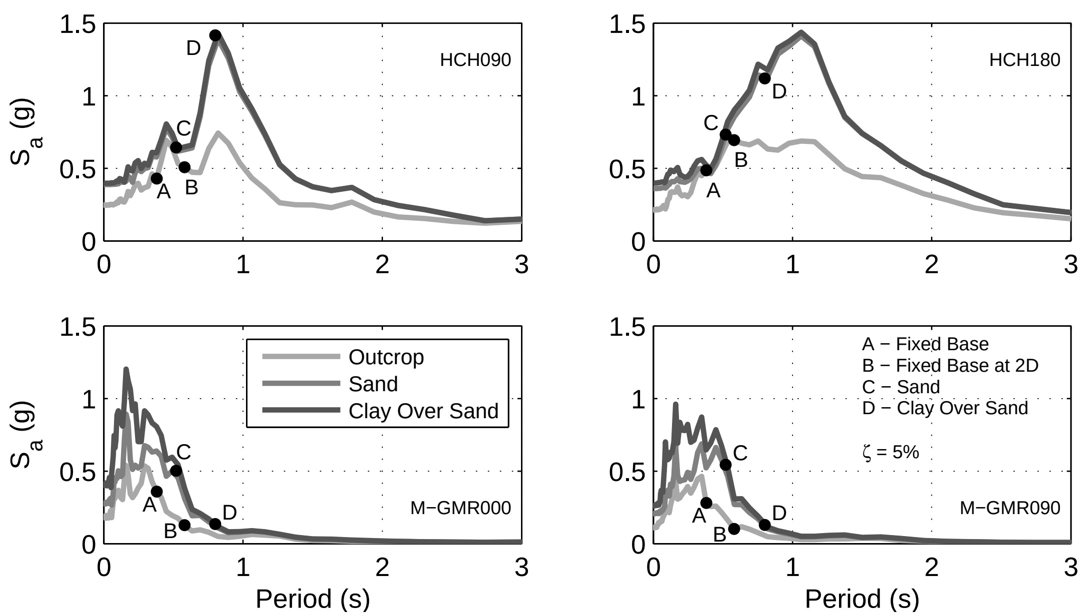

Fig. 5.10 Response spectra for ground motions where the soil-foundation-structure interaction effect is illustrated. For the cases with soil, the response spectra are shown for the ground motions at the ground surface at bent 1. Spectral values are plotted at the initial period of each simulation model.

5.6 CONCLUSIONS

Parameter studies conducted in parallel on a supercomputer have provided insight into the effect of soil-foundation-structure interaction on a reinforced concrete bridge system. Demand models have been developed for use within a performance-based framework and the influence of SFSI on the predicted response has been assessed. The demand models predict deformation response quantities that are significantly higher for rare events when the SFSI effect is included. Better fit exists for linear regressions of response quantities from simulation models including soil than for the fixed-base case. A deterministic comparison of the structural response for two specific cases reveals the extent to which more or less yielding can occur when including the SFSI effect. Where the site effect greatly amplifies the spectral acceleration at the period of interest, significantly more yielding is observed compared to the fixed-base case. While the consideration of additional intensity measures is outside the scope of this study, the response spectra for these deterministic cases suggest that intensity measures dependent on a spectral quantity at a measure of the structural period that incorporates SFSI should be evaluated. Additional intensity measures and regression models should be investigated and the sensitivity of the simulation results to model parameters should be studied to determine their influence on the demand models.

6 Conclusions

This chapter summarizes the report and the conclusions drawn from this research. Important issues for future research are presented.

6.1 SUMMARY

This report addresses the system response of reinforced concrete bridges including soil-foundation-structure interaction (SFSI). Chapter 1 introduces the research topic and provides the motivation for the research. Chapter 2 includes a literature review of previous research on the performance of reinforced concrete bridges. Important research related to the experimental testing of bridge components and computational simulation of the seismic response of bridges is described. Previous work on the assessment of seismic demands within a performance-based engineering framework is highlighted.

The experimental testing and computational simulation of shaking table tests of a two-span and a four-span reinforced concrete bridge are discussed in Chapter 3. The simulation model is developed using OpenSees and is validated with the test results from the two-span bridge. Comparisons are made at both the global and local levels. Further studies evaluate the simulation response when compared to the test results from the four-span bridge.

Chapter 4 develops a simulation model for a prototype bridge system including SFSI. The prototype bridge is taken from prototype designs used for experimental testing of the two-span and four-span bridges. The model incorporates the influence of the abutments, drilled shaft foundations, and site response effects. The input excitation using site response for ground motions of varying magnitude and distance from the fault is detailed.

Chapter 5 provides a comprehensive assessment of the SFSI effect within a performance-based engineering framework. Large-scale parameter studies are conducted on a supercomputer for four different prototype bridge models with and without the SFSI effect. The influence of SFSI is quantified through comparisons of demand models that relate an intensity measure to engineering demand parameters at both the global and local levels.

6.2 CONCLUSIONS OF THE RESEARCH

High-fidelity simulation models that are calibrated against the results of experimental tests must be developed to give accurate predictions of the response of reinforced concrete bridge systems. The response must account for all aspects of the bridge system including soil-foundation-structure interaction at the abutments and foundations.

Simulations of shaking table tests of a two-span and a four-span reinforced concrete bridge are performed with OpenSees. When using the beam with hinges column element with a fixed plastic hinge length defined by Priestley et al. (1996), the simulation model matches well both the global and local response until the onset of failure at a drift ratio approaching 5.5%. Column models employing a zero-length element at the column ends to account for strain penetration may underestimate the local response. The analyst must carefully select the fixed plastic hinge length for the beam with hinges model as a shorter length may significantly impact the predicted local response. The highly nonlinear pounding at the abutments and complicated test protocol of the four-span bridge produces less agreement in the simulation results. Additional rotational flexibility is present at the cap beam interface. The friction at contact points during sustained pounding events restricts the motion of the bridge in the transverse direction causing it to be driven to larger drift ratios upon release. The abutment sliding system does not provide sufficient restraint to prevent rotation of the abutment during pounding events. Given the many challenges in modeling the response of the four-span bridge, the simulation models underestimate the peak drift ratios at bents 1 and 3 by as much as 30% and do not reproduce the residual displacements at these locations. Experimental tests should be designed, instrumented, and tested in such a way that the results may be used to validate the simulation model. More refined models for flexural failure including loss of confinement and buckling of longitudinal reinforcement must be developed to facilitate the accurate prediction of collapse by the simulations.

The parallel capability of OpenSees and access to a supercomputer enable the analyst to perform large-scale parameter studies of bridge systems including SFSI. A prototype bridge model is developed that incorporates the influence of the abutments, drilled shaft foundations, and site response effects. Demand models for use within a performance-based framework predict larger values of deformation quantities for rare events when including SFSI. Better fit exists for linear regressions of response quantities from simulation models including soil than for the fixed-base case. For ground motions where the site effect greatly amplifies the spectral acceleration at the structural period, significantly more yielding can occur when including SFSI compared to the fixed-base case. In such cases, the SFSI effect should be considered to give accurate predictions of the demand within a performance-based engineering framework.

6.3 FUTURE RESEARCH

This research effort provides an improvement in the understanding of soil-foundation-structure interaction in reinforced concrete bridge systems. Further research should focus on the following issues.

1. Appropriate intensity measures must be obtained that provide good fit for the demand models when including SFSI. Intensity measures that are dependent on the site effect should be evaluated.
2. Sensitivity analyses should be performed to consider the influence of modeling assumptions on the response. Among the modeling parameters that should be varied are the abutment mass and site effects. Additional studies of abutment-embankment interaction and liquefaction effects should also be explored.
3. The extent to which response modification devices benefit the structural response when including SFSI must be understood. Demand models for simulations that incorporate isolation bearings at the tops of the bents and at the abutments should be computed.
4. High-performance computing should be made more accessible to the structural analyst. User-friendly portals that enable the analyst to run parameter studies and obtain the results will allow the structural engineering profession to keep pace with developments in computational technology.

REFERENCES

American Association of State Highway and Transportation Officials (2002). *AASHTO Standard Specifications for Highway Bridges*. AASHTO, Washington, D.C., 17 edition.

American Petroleum Institute (API) (1993). *Recommended practice for planning, design, and constructing fixed offshore platforms*. 20 edition.

Applied Technology Council (1996). *Improved Seismic Design Criteria for California Bridges*. 32 edition.

ATC/MCEER (2003). *Recommended LRFD guidelines for the seismic design of highway bridges*. Report no., Multidisciplinary Center for Earthquake Resistant Engineering Research.

Aviram, A., Mackie, K., and Stojadinovic, B. (2008a). Effect of abutment modeling on the seismic response of bridge structures. In *Proceedings of the 14th World Conference on Earthquake Engineering*, Beijing, China, October.

Aviram, A., Mackie, K. R., and Stojadinovic, B. (2008b). *Guidelines for Nonlinear Analysis of Bridge Structures in California*. Report No. 03, Pacific Earthquake Engineering Research Center.

Berry, M. P., Lehman, D. E., and Lowes, L. N. (2008). Lumped-plasticity models for performance simulation of bridge columns. *ACI Structural Jounal* 105(3): 270–279.

Boore, D. M., Stephens, C. D., and Joyner, W. B. (2002). Comments on baseline correction of digital strong-motion data: Examples from the 1999 Hector Mine, California, earthquake. *Bulletin of the Seismological Society of America* 92(4): 1543–1560.

Boulanger, R. W., Curras, C. J., Kutter, B. L., Wilson, D. W., and Abghari, A. (1999). Seismic soil-pile-structure interaction experiments and analyses. *Journal of Geotechnical and Geoenvironmental Engineering* 125(9): 750–759.

Bozorgnia, Y. and Bertero, V. V., *Eds*. (2004). *Earthquake Engineering: From Engineering Seismology to Performance-Based Engineering*. CRC Press.

Bozorgzadeh, A., Megally, S., Restrepo, J. I., and Ashford, S. A. (2006). Capacity evaluation of sacrificial exterior shear keys of bridge abutments. *Journal of Bridge Engineering* 11(5): 555–565.

Brandenberg, S. J. (2005). *Behavior of Pile Foundations in Liquefied and Laterally Spreading Ground*. Ph.D. thesis, University of California, Davis.

Brandenberg, S. J., Boulanger, R. W., Kutter, B. L., and Chang, D. (2007). Static pushover analyses of pile groups in liquefied and laterally spreading ground in centrifuge tests. *Journal of Geotechnical and Geoenvironmental Engineering* 133(9): 1055–1066.

Caltrans (1989). *Bridge Design Aids 14-1*. California Department of Transportation, Sacramento, CA.

Caltrans (2000). *Caltrans Bridge Design Specifications*. California Department of Transportation.

Caltrans (2004). *Caltrans Seismic Design Criteria version 1.3*. California Department of Transportation.

Chang, G. A. and Mander, J. B. (1994). *Seismic Energy Based Fatigue Damage Analysis of Bridge Columns: Part I - Evaluation of Seismic Capacity*. Report No. 94-06, National Center for Earthquake Engineering Research.

EduPro Civil Systems, Inc. (1999). *ProShake Ground Response Analysis Program*. Redmond, WA. http://www.proshake.com/.

Fenves, G. L. and Ellery, M. (1998). *Behavior and Failure Analysis of a Multiple-Frame Highway Bridge in the 1994 Northridge Earthquake*. Report No. 08, Pacific Earthquake Engineering Research Center.

Gazetas, G. and Mylonakis, G. (1998). Seismic soil-structure interaction: New evidence and emerging issues. In *Geotechnical Special Publication*, ASCE, volume 2, pp. 1119–1174.

Goel, R. K. and Chopra, A. K. (1997). Evaluation of bridge abutment capacity and stiffness during earthquakes. *Earthquake Spectra* 13(1): 1–23.

Grant, D. N., Fenves, G. L., and Whittaker, A. S. (2004). Bidirectional modelling of high-damping rubber bearings. *Journal of Earthquake Engineering* 8(Special Issue 1): 161–185.

Hachem, M. M., Mahin, S. A., and Moehle, J. P. (2003). *Performance of Circular Reinforced Concrete Bridge Columns under Bidirectional Earthquake Loading*. Report No. 06, Pacific Earthquake Engineering Research Center.

Hutchinson, T. C., Chai, Y. H., Boulanger, R. W., and Idriss, I. M. (2004). Inelastic seismic response of extended pile-shaft-supported bridge structures. *Earthquake Spectra* 20(4): 1057–1080.

Idriss, I. M. and Sun, J. M. (1992). *User's Manual for SHAKE91*. Center for Geotechnical Modeling, Davis, California, November. http://nisee.berkeley.edu/elibrary/getpkg?id=SHAKE91.

Jeremic, B., Kunnath, S., and Xiong, F. (2004). Influence of soil-foundation-structure interaction on seismic response of the I-880 viaduct. *Engineering Structures* 26(3): 391–402.

Johnson, N. S., Saiidi, M. S., and Sanders, D. H. (2006). *Large-Scale Experimental and Analytical Seismic Studies of a Two-Span Reinforced Concrete Bridge System*. Report No. 06-02, Center for Civil Engineering Earthquake Research, Reno, NV.

Kent, D. C. and Park, R. (1971). Flexural members with confined concrete. *Journal of the Structural Division, ASCE* 97(7): 1969–1990.

Kramer, S. L. (1996). *Geotechnical Earthquake Engineering*. Prentice Hall.

Lam, I. P., Kapuskar, M., and Chaudhuri, D. (1998). *Modeling of Pile Footings and Drilled Shafts for Seismic Design*. Report No. 18, Multidisciplinary Center for Earthquake Engineering Research.

Lehman, D. E. and Moehle, J. P. (1998). *Seismic Performance of Well-Confined Concrete Bridge Columns*. Report No. 01, Pacific Earthquake Engineering Research Center.

Mackie, K. and Stojadinovic, B. (2003). *Seismic Demands for Performance-Based Design of Bridges*. Report No. 16, Pacific Earthquake Engineering Research Center.

Mackie, K. R., Wong, J.-M., and Stojadinovic, B. (2008). *Integrated Probabilistic Performance-Based Evaluation of Benchmark Reinforced Concrete Bridges*. Report No. 2007/09, Pacific Earthquake Engineering Research Center.

Mander, J. B., Priestley, M. J. N., and Park, R. (1988). Theoretical stress-strain model for confined concrete. *Journal of Structural Engineering* 114(8): 1804–1826.

Matlab (2007). *The Language of Technical Computing*. The MathWorks Inc. Version 7.4.0.

Mazzoni, S., Fenves, G. L., and Smith, J. B. (2004). *Effects of Local Deformations on Lateral Response of Bridge Frames*. Report no., University of California, Berkeley. http://www.dot.ca.gov/hq/esc/earthquake_engineering/Research/techreps.html.

McCallen, D. B. and Romstad, K. M. (1994). Dynamic analyses of a skewed, short-span box-girder overpass. *Earthquake Spectra* 10(4): 729–755.

McKenna, F. and Fenves, G. L. (2008). *Using the OpenSees Interpreter on Parallel Computers*. Report No. TN-2007-16, University of California, Berkeley.

http://beta.nees.org/images/doc_library/TN-2007-16_McKenna-OpenSees.pdf.

McKenna, F., Fenves, G. L., Scott, M. H., and Jeremic, B. (2000). Open system for earthquake engineering simulation. http://opensees.berkeley.edu.

McVerry, G. H. (1980). Structural identification in the frequency domain from earthquake records. *Earthquake Engineering and Structural Dynamics* 8: 161–180.

Medina, R. and Krawinkler, H. (2004). *Seismic Demands for Nondeteriorating Frame Structures and Their Dependence on Ground Motions*. Report No. 2003/15, Pacific Earthquake Engineering Research Center.

Meyerhof, G. G. (1976). Bearing capacity and settlement of pile foundations. *Journal of the Geotechnical Engineering Division, ASCE* 102: 197–228.

Montgomery, D. C., Runger, G. C., and Hubele, N. F. (2007). *Engineering Statistics*. John Wiley, Hoboken, NJ, 4 edition.

Muthukumar, S. (2003). *A Contact Element Approach with Hysteresis Damping for the Analysis and Design of Pounding in Bridges*. Ph.D. thesis, Georgia Institute of Technology.

National Center for Supercomputing Applications (2009). NCSA Intel 64 cluster user documentation. http://www.ncsa.uiuc.edu/UserInfo/Resources/.

Nelder, J. A. and Mead, R. (1965). A simplex-method for function minimization. *Computer Journal* 7(4): 308–313.

Nelson, R. B., Saiidi, M. S., and Zadeh, S. (2007). *Experimental Evaluation of Performance of Conventional Bridge Systems*. Report No. 07-04, Center for Civil Engineering Earthquake Research, Reno, NV.

Neuenhofer, A. and Filippou, F. (1997). Evaluation of nonlinear frame finite-element models. *Journal of Structural Engineering* 123(7): 958–966.

Newmark, N. M. and Hall, W. J. (1982). *Earthquake Spectra and Design*. Earthquake Engineering Research Institute, Berkeley, CA.

Nielson, B. G. (2005). *Analytical Fragility Curves for Highway Bridges in Moderate Seismic Zones*. Ph.D. thesis, Georgia Institute of Technology.

Padgett, J. E. (2007). *Seismic Vulnerability Assessment of Retrofitted Bridges Using Probabilistic Methods*. Ph.D. thesis, Georgia Institute of Technology.

Padgett, J. E. and DesRoches, R. (2009). Retrofitted bridge fragility analysis for typical classes of multispan bridges. *Earthquake Spectra* 25(1): 117–141.

Pakzad, S. (2008). *Statistical Approach to Structural Monitoring Using Scalable Wireless Sensor Networks*. Ph.D. thesis, University of California, Berkeley.

Pappa, R. S. and Elliott, K. B. (1993). Consistent-mode indicator for the eigensystem realization algorithm. *Journal of Guidance, Control, and Dynamics* 16(5): 852–858.

Priestley, M. J. N., Seible, F., and Calvi, G. M. (1996). *Seismic Design and Retrofit of Bridges*. John Wiley & Sons, Inc., New York.

Ranf, R. T. (2007). *Model Selection for Performance-Based Earthquake Engineering of Bridges*. Ph.D. thesis, University of Washington.

Scott, B. D., Park, R., and Priestley, M. J. N. (1982). Stress-strain behavior of concrete confined by overlapping hoops at low and high strain rates. *ACI Journal* 79(1): 13–27.

Scott, M. H. and Fenves, G. L. (2006). Plastic hinge integration methods for force-based beam-column elements. *Journal of Structural Engineering* 132(2): 244–252.

Seed, H. B. and Idriss, I. M. (1970). *Soil Moduli and Damping Factors for Dynamic Response Analyses*. Report No. 10, Earthquake Engineering Research Center.

Sextos, A., Mackie, K., Stojadinovic, B., and Taskari, O. (2008). Simplified p-y relationships for modeling embankment-abutment systems of typical California bridges. In *The 14th World Conference on Earthquake Engineering*, 05-02-0032, Beijing, China, October.

Shamsabadi, A., Rollins, K. M., and Kapuskar, M. (2007). Nonlinear soil-abutment-bridge structure interaction for seismic performance-based design. *Journal of Geotechnical and Geoenvironmental Engineering* 133(6): 707–720.

Shin, H. (2007). *Numerical Modeling of a Bridge System & its Application for Performance-Based Earthquake Engineering*. Ph.D. thesis, University of Washington.

Shin, H., Ilankathara, M., Arduino, P., Kutter, B. L., and Kramer, S. L. (2006). Experimental and numerical analysis of seismic soil-pile-structure interaction of a two-span bridge. In *Proceedings of the 8th U.S. National Conference on Earthquake Engineering*, 1649, San Francisco, CA, April.

Shome, N. (1999). *Probabilistic Seismic Demand Analysis of Nonlinear Structures*. Ph.D. thesis, Stanford University.

Spacone, E., Filippou, F. C., and Taucer, F. F. (1996). Fibre beam-column model for non-linear analysis of R/C frames 1. Formulation. *Earthquake Engineering and Structural Dynamics* 25: 711–725.

Veletsos, A. S. (1977). Dynamics of structure-foundation systems. *Structural and Geotechnical Mechanics* .

Vucetic, M. and Dobry, R. (1991). Effect of soil plasticity on cyclic response. *Journal of Geotechnical Engineering* 117(1): 89–107.

Wilson, P. and Elgamal, A. (2008). Full scale bridge abutment passive earth pressure tests and calibrated models. In *The 14th World Conference on Earthquake Engineering*, Beijing, China, October.

Yassin, M. (1994). *Nonlinear Analysis of Prestressed Concrete Structures under Monotonic and Cyclic Loads*. Ph.D. thesis, University of California, Berkeley.

Zadeh, M. S. and Saiidi, M. S. (2007). *Pre-test Analytical Studies of NEESR-SG 4-Span Bridge Model Using OpenSees*. Report No. 07-03, Center for Civil Engineering Earthquake Research, Reno, NV.

Zhang, J. and Makris, N. (2001). *Seismic Response Analysis of Highway Overcrossings Including Soil-Structure Interaction*. Report No. 2001/02, Pacific Earthquake Engineering Research Center.

Zhang, J. and Makris, N. (2002a). Kinematic response functions and dynamic stiffnesses of bridge embankments. *Earthquake Engineering & Structural Dynamics* 31(11): 1933–1966.

Zhang, J. and Makris, N. (2002b). Seismic response analysis of highway overcrossings including soil-structure interaction. *Earthquake Engineering & Structural Dynamics* 31(11): 1967–1991.

Appendix A: Experimental Tests of the Two-Span and Four-Span Bridges

The appendix includes information related to the 1/4-scale two-span and four-span reinforced concrete bridges that were tested at the University of Nevada, Reno (Johnson et al., 2006; Nelson et al., 2007). The geometry of the bridges and instrumentation for the columns are shown in Figures A.1 and A.2, respectively. Peak response quantities for the two-span bridge are listed in Tables A.1 and A.2. The peak response quantities for the four-span bridge are given in Tables A.3 through A.6.

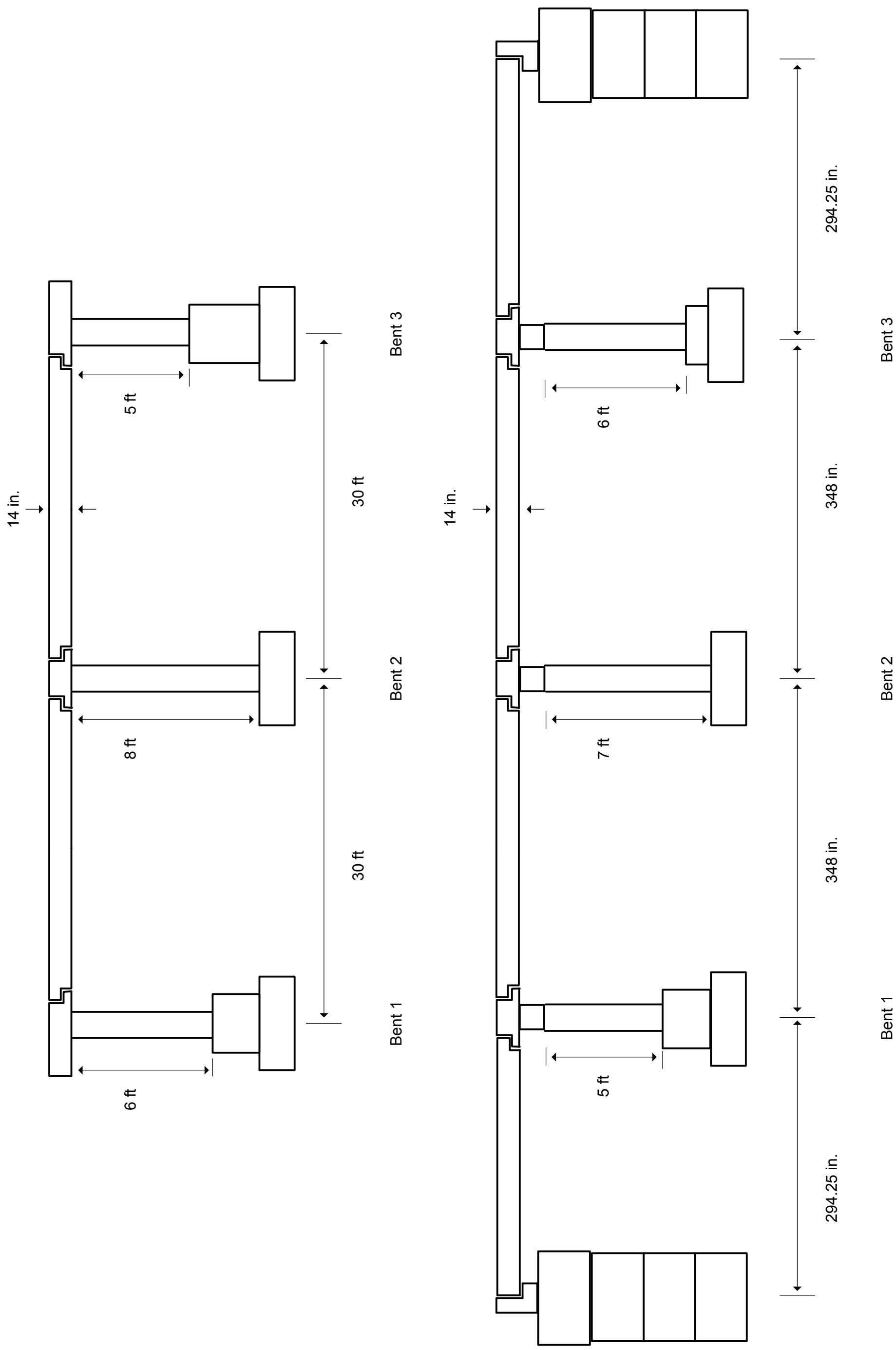

Fig. A.1 Elevations of the 2-span and 4-span bridges.

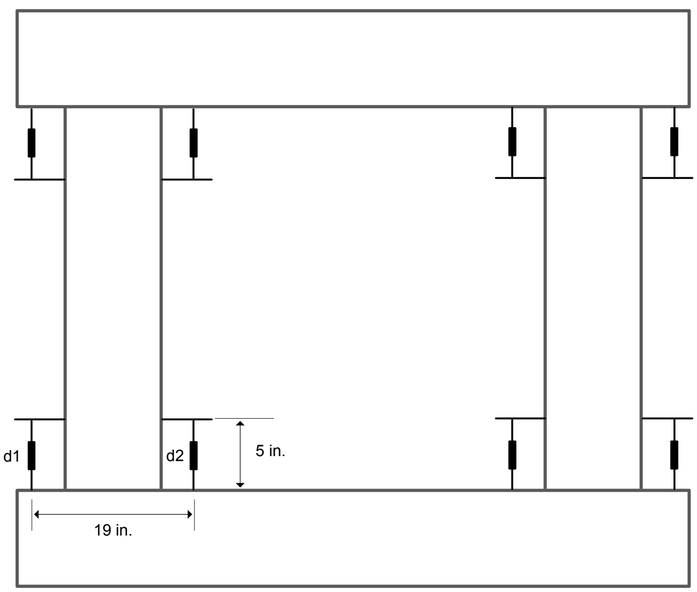

Fig. A.2 Instrumentation for determining column curvature for the 2-span bridge.

Table A.1 Measured peak accelerations during shaking table tests of the 2-span bridge.

Test	Max Table Acceleration (g)			Max Bent Acceleration (g)		
	Table 1	Table 2	Table 3	Bent 1	Bent 2	Bent 3
1a	0.13	0.23	0.13	0.09	0.08	0.08
1b	0.21	0.32	0.25	0.12	0.14	0.13
2a	0.03	0.13	0.07	0.08	0.07	0.11
2b	0.07	0.34	0.16	0.18	0.12	0.23
3a	0.08	0.13	0.05	0.08	0.06	0.04
3b	0.17	0.38	0.08	0.18	0.11	0.08
4b	0.07	0.22	0.23	0.10	0.08	0.15
5b	0.21	0.10	0.25	0.11	0.11	0.13
6b	0.20	0.21	0.09	0.09	0.08	0.07
8	0.16	0.22	0.21	0.10	0.11	0.10
9a	0.09	0.10	0.10	0.05	0.05	0.04
9b	0.17	0.33	0.21	0.11	0.13	0.10
10a	0.08	0.10	0.10	0.15	0.09	0.13
11a	0.07	0.09	0.10	0.13	0.08	0.13
12	0.07	0.10	0.08	0.18	0.14	0.16
13	0.18	0.18	0.17	0.36	0.28	0.30
14	0.35	0.31	0.28	0.42	0.32	0.41
15	0.67	0.65	0.72	0.48	0.52	0.58
16	0.98	0.94	1.25	0.47	0.52	0.56
17	1.20	1.50	1.09	0.43	0.41	0.50
18	1.56	1.81	1.59	0.48	0.54	0.63
19	2.00	2.13	2.20	0.53	0.47	0.59
20	1.26	1.30	1.44	0.42	0.29	0.24

Table A.2 Measured peak drift ratios during shaking table tests of the 2-span bridge.

Test	Max Drift Ratio (%)			Residual Drift Ratio (%)		
	Bent 1	Bent 2	Bent 3	Bent 1	Bent 2	Bent 3
1a	0.13	0.09	0.08	-0.01	0.01	-0.01
1b	0.21	0.14	0.15	-0.01	0.01	-0.01
2a	0.08	0.05	0.12	-0.01	0.01	-0.01
2b	0.18	0.13	0.32	-0.02	0.01	-0.01
3a	0.12	0.06	0.09	-0.02	0.02	-0.02
3b	0.27	0.14	0.10	-0.01	0.02	-0.01
4b	0.14	0.10	0.17	-0.01	0.02	0.00
5b	0.17	0.09	0.17	-0.02	0.03	-0.01
6b	0.17	0.10	0.08	-0.02	0.03	0.01
8	0.18	0.10	0.13	-0.02	0.02	0.01
9a	0.08	0.06	0.15	-0.02	0.03	0.01
9b	0.19	0.14	0.14	-0.02	0.04	-0.01
10a	0.25	0.14	0.15	-0.02	0.05	-0.02
11a	0.20	0.13	0.16	-0.02	0.05	-0.02
12	0.32	0.21	0.22	-0.02	0.06	-0.01
13	0.87	0.44	0.55	-0.02	0.07	-0.03
14	1.07	0.55	0.83	-0.02	0.07	-0.02
15	2.15	1.24	2.43	-0.08	0.04	-0.09
16	3.68	2.45	3.13	0.18	0.16	0.01
17	2.77	2.09	2.37	0.23	0.16	-0.05
18	3.84	3.58	5.53	-0.08	0.11	0.16
19	4.89	4.39	7.84	0.09	0.02	-0.36
20	3.11	3.16	5.81	0.02	0.01	-0.28

Table A.3 Measured peak table accelerations during shaking table tests of the 4-span bridge.

Test	Max Table Acceleration (g)					
	Transverse			Longitudinal		
	Table 1	Table 2	Table 3	Table 1	Table 2	Table 3
1B	0.00	0.00	0.00	0.11	0.14	0.13
1C	0.00	0.00	0.01	0.10	0.13	0.12
1D	0.14	0.12	0.11	0.12	0.14	0.15
2	0.18	0.20	0.18	0.26	0.38	0.36
3	0.29	0.29	0.28	0.41	0.70	0.48
4A	0.01	0.03	0.02	0.88	1.22	1.25
4B	0.01	0.01	0.01	0.81	0.91	0.91
4C	0.01	0.01	0.01	0.78	0.92	0.78
4D	0.66	0.66	0.65	0.69	0.89	0.85
5	0.98	1.01	1.01	0.90	1.08	1.09
6	1.34	1.32	1.43	1.28	1.54	1.43
7	1.20	1.18	1.26	1.23	1.26	1.27

Table A.4 Measured peak deck accelerations during shaking table tests of the 4-span bridge.

Test	Max Deck Acceleration (g)			
	Transverse			Longitudinal
	Bent 1	Bent 2	Bent 3	Deck
1B	0.01	0.01	0.01	0.06
1C	0.01	0.01	0.01	0.14
1D	0.27	0.12	0.21	0.10
2	0.45	0.57	0.50	0.56
3	0.42	0.87	0.60	0.78
4A	0.08	0.07	0.06	0.43
4B	0.05	0.04	0.04	0.38
4C	0.03	0.02	0.01	0.23
4D	0.54	1.07	0.56	0.70
5	0.78	0.88	0.52	0.80
6	0.76	1.26	0.85	0.79
7	0.72	1.18	0.77	0.92

Table A.5 Measured peak drift ratios during shaking table tests of the 4-span bridge.

Test	Peak Drift Ratio (%)					
	Transverse			Longitudinal		
	Bent 1	Bent 2	Bent 3	Bent 1	Bent 2	Bent 3
1B	0.37	0.11	0.14	0.32	0.22	0.25
1C	0.12	0.08	0.08	0.33	0.23	0.25
1D	1.09	0.31	0.88	0.48	0.28	0.61
2	0.76	0.48	0.80	2.55	1.77	2.04
3	1.36	0.87	1.35	3.60	2.38	2.84
4A	0.16	0.07	0.13	3.18	2.09	2.43
4B	0.18	0.10	0.08	3.20	2.27	2.54
4C	0.15	0.08	0.09	4.52	3.31	3.79
4D	2.70	1.50	2.65	4.28	3.09	3.49
5	3.99	1.79	4.34	5.71	4.16	4.68
6	7.71	2.71	6.97	7.07	5.15	5.81
7	8.94	3.11	7.40	7.20	5.27	5.97

Table A.6 Measured residual drift ratios during shaking table tests of the 4-span bridge.

Test	Residual Drift Ratio (%)					
	Transverse			Longitudinal		
	Bent 1	Bent 2	Bent 3	Bent 1	Bent 2	Bent 3
1B	0.02	-0.02	0.00	-0.00	0.00	-0.01
1C	0.00	-0.03	-0.00	0.00	-0.00	-0.00
1D	0.05	-0.00	0.04	-0.01	0.00	0.00
2	0.06	-0.01	0.05	-0.11	-0.07	-0.10
3	-0.03	-0.03	-0.01	-0.07	-0.05	-0.07
4A	-0.08	-0.03	0.00	-0.93	-0.67	-0.77
4B	-0.04	-0.04	0.01	-0.24	-0.17	-0.20
4C	0.03	-0.03	-0.01	0.00	-0.00	0.01
4D	0.20	-0.08	-0.31	-0.12	-0.08	-0.09
5	0.65	0.07	-0.64	0.31	0.12	0.18
6	1.66	0.07	-1.12	-0.06	-0.05	-0.05
7	2.73	0.35	-1.42	-0.08	-0.05	-0.06

Appendix B: Modifications to Achieve Convergence

The appendix describes key modifications that were required to achieve convergence when performing highly nonlinear finite element simulations of the prototype bridge models. First, the algorithm for the force-based beam-column element is revised to revert to a noniterative scheme. Next, the algorithms and analysis time step for the input script are modified to obtain a converged solution.

The current version of ForceBeamColumn3d.cpp in the repository performs iterations at the element level as described by Spacone et al. (1996). By default, maxNumIters = 10 and tolerance = 1.0e-12. The following sequence of iterations are performed at the element level to achieve convergence: (1) maxNumIters using Newton, (2) 10*maxNumIters using Newton with initial tangent, and (3) maxNumIters using Newton with initial tangent on the first iteration followed by Newton for the remaining iterations. The code was modified as shown in Table B.1 to revert to the noniterative scheme proposed by Neuenhofer and Filippou (1997) provided that the convergence criteria is not met at the element level. This element formulation modifies the element resisting forces for the current global iteration and thus element convergence and global convergence are achieved simultaneously. The maximum number of subdivisions for reducing the size of the trial element deformations, dvTrial, in the event of nonconvergence was reduced from 10 to 1 to allow for a more efficient use of the noniterative method.

The input file was modified to reduce the analysis time step and change the solution algorithm to achieve convergence as shown in Table B.2. In the case that the Newton algorithm with the initial analysis time step did not converge, the following sequence of actions were followed until the point of convergence.

Table B.1 Modifications to ForceBeamColumn3d.cpp.

```
Line 499
maxSubdivisions = 1;

Line 920 - within if(converged==false)
// return -1;
```

1. Reduce the analysis time step to as small as 1/100 the initial value.
2. Perform 2500 iterations with the initial tangent stiffness and 1/100 of the initial analysis time step.
3. Invoke the Broyden and NewtonLineSearch algorithms at 1/100 of the initial analysis time step.

Table B.2 Modifying the script in the case of no convergence.

```
# Perform dynamic analysis
while {$tCurrent < $tFinal && $ok == 0} {
 test $testtype $tol $maxNumIter 0;
 set ok [analyze 1 $DtAnalysis]
 if {$ok != 0} {
 set ok [analyze 1 [expr $DtAnalysis/20.0]];
 }
 if {$ok != 0} {
 set ok [analyze 1 [expr $DtAnalysis/50.0]];
 }
 if {$ok != 0} {
 set ok [analyze 1 [expr $DtAnalysis/100.0]];
 }
 if {$ok != 0} {
 test $testtype $tol 2500 0;
 algorithm Newton -initial
 set ok [analyze 1 [expr $DtAnalysis/100.0]]
 test $testtype $tol $maxNumIter 0;
 }
 if {$ok != 0} {
 algorithm Broyden 8
 set ok [analyze 1 [expr $DtAnalysis/100.0]]
 }
 if {$ok != 0} {
 algorithm NewtonLineSearch .8
 set ok [analyze 1 [expr $DtAnalysis/100.0]]
 algorithm Newton
 }
 set tCurrent [getTime]
}
```

PEER REPORTS

PEER reports are available individually or by yearly subscription. PEER reports can be ordered at http://peer.berkeley.edu/publications/peer_reports.html or by contacting the Pacific Earthquake Engineering Research Center, 1301 South 46th Street, Richmond, CA 94804-4698. Tel.: (510) 665-3448; Fax: (510) 665-3456; Email: peer_editor@berkeley.edu

PEER 2009/03 *The Integration of Experimental and Simulation Data in the Study of Reinforced Concrete Bridge Systems Including Soil-Foundation-Structure Interaction.* Matthew Dryden and Gregory L. Fenves. November 2009.

PEER 2009/02 *Improving Earthquake Mitigation through Innovations and Applications in Seismic Science, Engineering, Communication, and Response. Proceedings of a U.S.-Iran Seismic Workshop.* October 2009.

PEER 2009/01 *Evaluation of Ground Motion Selection and Modification Methods: Predicting Median Interstory Drift Response of Buildings.* Curt B. Haselton, Ed. June 2009.

PEER 2008/10 *Technical Manual for Strata.* Albert R. Kottke and Ellen M. Rathje. February 2009.

PEER 2008/09 *NGA Model for Average Horizontal Component of Peak Ground Motion and Response Spectra.* Brian S.-J. Chiou and Robert R. Youngs. November 2008.

PEER 2008/08 *Toward Earthquake-Resistant Design of Concentrically Braced Steel Structures.* Patxi Uriz and Stephen A. Mahin. November 2008.

PEER 2008/07 *Using OpenSees for Performance-Based Evaluation of Bridges on Liquefiable Soils.* Stephen L. Kramer, Pedro Arduino, and HyungSuk Shin. November 2008.

PEER 2008/06 *Shaking Table Tests and Numerical Investigation of Self-Centering Reinforced Concrete Bridge Columns.* Hyung IL Jeong, Junichi Sakai, and Stephen A. Mahin. September 2008.

PEER 2008/05 *Performance-Based Earthquake Engineering Design Evaluation Procedure for Bridge Foundations Undergoing Liquefaction-Induced Lateral Ground Displacement.* Christian A. Ledezma and Jonathan D. Bray. August 2008.

PEER 2008/04 *Benchmarking of Nonlinear Geotechnical Ground Response Analysis Procedures.* Jonathan P. Stewart, Annie On-Lei Kwok, Yousseff M. A. Hashash, Neven Matasovic, Robert Pyke, Zhiliang Wang, and Zhaohui Yang. August 2008.

PEER 2008/03 *Guidelines for Nonlinear Analysis of Bridge Structures in California.* Ady Aviram, Kevin R. Mackie, and Božidar Stojadinović. August 2008.

PEER 2008/02 *Treatment of Uncertainties in Seismic-Risk Analysis of Transportation Systems.* Evangelos Stergiou and Anne S. Kiremidjian. July 2008.

PEER 2008/01 *Seismic Performance Objectives for Tall Buildings.* William T. Holmes, Charles Kircher, William Petak, and Nabih Youssef. August 2008.

PEER 2007/12 *An Assessment to Benchmark the Seismic Performance of a Code-Conforming Reinforced Concrete Moment-Frame Building.* Curt Haselton, Christine A. Goulet, Judith Mitrani-Reiser, James L. Beck, Gregory G. Deierlein, Keith A. Porter, Jonathan P. Stewart, and Ertugrul Taciroglu. August 2008.

PEER 2007/11 *Bar Buckling in Reinforced Concrete Bridge Columns.* Wayne A. Brown, Dawn E. Lehman, and John F. Stanton. February 2008.

PEER 2007/10 *Computational Modeling of Progressive Collapse in Reinforced Concrete Frame Structures.* Mohamed M. Talaat and Khalid M. Mosalam. May 2008.

PEER 2007/09 *Integrated Probabilistic Performance-Based Evaluation of Benchmark Reinforced Concrete Bridges.* Kevin R. Mackie, John-Michael Wong, and Božidar Stojadinović. January 2008.

PEER 2007/08 *Assessing Seismic Collapse Safety of Modern Reinforced Concrete Moment-Frame Buildings.* Curt B. Haselton and Gregory G. Deierlein. February 2008.

PEER 2007/07 *Performance Modeling Strategies for Modern Reinforced Concrete Bridge Columns.* Michael P. Berry and Marc O. Eberhard. April 2008.

PEER 2007/06 *Development of Improved Procedures for Seismic Design of Buried and Partially Buried Structures.* Linda Al Atik and Nicholas Sitar. June 2007.

PEER 2007/05 *Uncertainty and Correlation in Seismic Risk Assessment of Transportation Systems.* Renee G. Lee and Anne S. Kiremidjian. July 2007.

PEER 2007/04 *Numerical Models for Analysis and Performance-Based Design of Shallow Foundations Subjected to Seismic Loading.* Sivapalan Gajan, Tara C. Hutchinson, Bruce L. Kutter, Prishati Raychowdhury, José A. Ugalde, and Jonathan P. Stewart. May 2008.

PEER 2007/03 *Beam-Column Element Model Calibrated for Predicting Flexural Response Leading to Global Collapse of RC Frame Buildings.* Curt B. Haselton, Abbie B. Liel, Sarah Taylor Lange, and Gregory G. Deierlein. May 2008.

PEER 2007/02 *Campbell-Bozorgnia NGA Ground Motion Relations for the Geometric Mean Horizontal Component of Peak and Spectral Ground Motion Parameters.* Kenneth W. Campbell and Yousef Bozorgnia. May 2007.

PEER 2007/01 *Boore-Atkinson NGA Ground Motion Relations for the Geometric Mean Horizontal Component of Peak and Spectral Ground Motion Parameters.* David M. Boore and Gail M. Atkinson. May. May 2007.

PEER 2006/12 *Societal Implications of Performance-Based Earthquake Engineering.* Peter J. May. May 2007.

PEER 2006/11 *Probabilistic Seismic Demand Analysis Using Advanced Ground Motion Intensity Measures, Attenuation Relationships, and Near-Fault Effects.* Polsak Tothong and C. Allin Cornell. March 2007.

PEER 2006/10 *Application of the PEER PBEE Methodology to the I-880 Viaduct.* Sashi Kunnath. February 2007.

PEER 2006/09 *Quantifying Economic Losses from Travel Forgone Following a Large Metropolitan Earthquake.* James Moore, Sungbin Cho, Yue Yue Fan, and Stuart Werner. November 2006.

PEER 2006/08 *Vector-Valued Ground Motion Intensity Measures for Probabilistic Seismic Demand Analysis*. Jack W. Baker and C. Allin Cornell. October 2006.

PEER 2006/07 *Analytical Modeling of Reinforced Concrete Walls for Predicting Flexural and Coupled–Shear-Flexural Responses*. Kutay Orakcal, Leonardo M. Massone, and John W. Wallace. October 2006.

PEER 2006/06 *Nonlinear Analysis of a Soil-Drilled Pier System under Static and Dynamic Axial Loading.* Gang Wang and Nicholas Sitar. November 2006.

PEER 2006/05 *Advanced Seismic Assessment Guidelines.* Paolo Bazzurro, C. Allin Cornell, Charles Menun, Maziar Motahari, and Nicolas Luco. September 2006.

PEER 2006/04 *Probabilistic Seismic Evaluation of Reinforced Concrete Structural Components and Systems.* Tae Hyung Lee and Khalid M. Mosalam. August 2006.

PEER 2006/03 *Performance of Lifelines Subjected to Lateral Spreading.* Scott A. Ashford and Teerawut Juirnarongrit. July 2006.

PEER 2006/02 *Pacific Earthquake Engineering Research Center Highway Demonstration Project.* Anne Kiremidjian, James Moore, Yue Yue Fan, Nesrin Basoz, Ozgur Yazali, and Meredith Williams. April 2006.

PEER 2006/01 *Bracing Berkeley. A Guide to Seismic Safety on the UC Berkeley Campus.* Mary C. Comerio, Stephen Tobriner, and Ariane Fehrenkamp. January 2006.

PEER 2005/16 *Seismic Response and Reliability of Electrical Substation Equipment and Systems.* Junho Song, Armen Der Kiureghian, and Jerome L. Sackman. April 2006.

PEER 2005/15 *CPT-Based Probabilistic Assessment of Seismic Soil Liquefaction Initiation.* R. E. S. Moss, R. B. Seed, R. E. Kayen, J. P. Stewart, and A. Der Kiureghian. April 2006.

PEER 2005/14 *Workshop on Modeling of Nonlinear Cyclic Load-Deformation Behavior of Shallow Foundations.* Bruce L. Kutter, Geoffrey Martin, Tara Hutchinson, Chad Harden, Sivapalan Gajan, and Justin Phalen. March 2006.

PEER 2005/13 *Stochastic Characterization and Decision Bases under Time-Dependent Aftershock Risk in Performance-Based Earthquake Engineering.* Gee Liek Yeo and C. Allin Cornell. July 2005.

PEER 2005/12 *PEER Testbed Study on a Laboratory Building: Exercising Seismic Performance Assessment.* Mary C. Comerio, editor. November 2005.

PEER 2005/11 *Van Nuys Hotel Building Testbed Report: Exercising Seismic Performance Assessment.* Helmut Krawinkler, editor. October 2005.

PEER 2005/10 *First NEES/E-Defense Workshop on Collapse Simulation of Reinforced Concrete Building Structures.* September 2005.

PEER 2005/09 *Test Applications of Advanced Seismic Assessment Guidelines.* Joe Maffei, Karl Telleen, Danya Mohr, William Holmes, and Yuki Nakayama. August 2006.

PEER 2005/08 *Damage Accumulation in Lightly Confined Reinforced Concrete Bridge Columns.* R. Tyler Ranf, Jared M. Nelson, Zach Price, Marc O. Eberhard, and John F. Stanton. April 2006.

PEER 2005/07 *Experimental and Analytical Studies on the Seismic Response of Freestanding and Anchored Laboratory Equipment.* Dimitrios Konstantinidis and Nicos Makris. January 2005.

PEER 2005/06 *Global Collapse of Frame Structures under Seismic Excitations*. Luis F. Ibarra and Helmut Krawinkler. September 2005.

PEER 2005//05 *Performance Characterization of Bench- and Shelf-Mounted Equipment.* Samit Ray Chaudhuri and Tara C. Hutchinson. May 2006.

PEER 2005/04 *Numerical Modeling of the Nonlinear Cyclic Response of Shallow Foundations.* Chad Harden, Tara Hutchinson, Geoffrey R. Martin, and Bruce L. Kutter. August 2005.

PEER 2005/03 *A Taxonomy of Building Components for Performance-Based Earthquake Engineering.* Keith A. Porter. September 2005.

PEER 2005/02 *Fragility Basis for California Highway Overpass Bridge Seismic Decision Making*. Kevin R. Mackie and Božidar Stojadinović. June 2005.

PEER 2005/01 *Empirical Characterization of Site Conditions on Strong Ground Motion.* Jonathan P. Stewart, Yoojoong Choi, and Robert W. Graves. June 2005.

PEER 2004/09 *Electrical Substation Equipment Interaction: Experimental Rigid Conductor Studies.* Christopher Stearns and André Filiatrault. February 2005.

PEER 2004/08 *Seismic Qualification and Fragility Testing of Line Break 550-kV Disconnect Switches.* Shakhzod M. Takhirov, Gregory L. Fenves, and Eric Fujisaki. January 2005.

PEER 2004/07 *Ground Motions for Earthquake Simulator Qualification of Electrical Substation Equipment.* Shakhzod M. Takhirov, Gregory L. Fenves, Eric Fujisaki, and Don Clyde. January 2005.

PEER 2004/06 *Performance-Based Regulation and Regulatory Regimes.* Peter J. May and Chris Koski. September 2004.

PEER 2004/05 *Performance-Based Seismic Design Concepts and Implementation: Proceedings of an International Workshop.* Peter Fajfar and Helmut Krawinkler, editors. September 2004.

PEER 2004/04 *Seismic Performance of an Instrumented Tilt-up Wall Building.* James C. Anderson and Vitelmo V. Bertero. July 2004.

PEER 2004/03 *Evaluation and Application of Concrete Tilt-up Assessment Methodologies.* Timothy Graf and James O. Malley. October 2004.

PEER 2004/02 *Analytical Investigations of New Methods for Reducing Residual Displacements of Reinforced Concrete Bridge Columns.* Junichi Sakai and Stephen A. Mahin. August 2004.

PEER 2004/01 *Seismic Performance of Masonry Buildings and Design Implications.* Kerri Anne Taeko Tokoro, James C. Anderson, and Vitelmo V. Bertero. February 2004.

PEER 2003/18 *Performance Models for Flexural Damage in Reinforced Concrete Columns.* Michael Berry and Marc Eberhard. August 2003.

PEER 2003/17 *Predicting Earthquake Damage in Older Reinforced Concrete Beam-Column Joints.* Catherine Pagni and Laura Lowes. October 2004.

PEER 2003/16 *Seismic Demands for Performance-Based Design of Bridges.* Kevin Mackie and Božidar Stojadinović. August 2003.

PEER 2003/15 *Seismic Demands for Nondeteriorating Frame Structures and Their Dependence on Ground Motions.* Ricardo Antonio Medina and Helmut Krawinkler. May 2004.

PEER 2003/14 *Finite Element Reliability and Sensitivity Methods for Performance-Based Earthquake Engineering.* Terje Haukaas and Armen Der Kiureghian. April 2004.

PEER 2003/13 *Effects of Connection Hysteretic Degradation on the Seismic Behavior of Steel Moment-Resisting Frames.* Janise E. Rodgers and Stephen A. Mahin. March 2004.

PEER 2003/12 *Implementation Manual for the Seismic Protection of Laboratory Contents: Format and Case Studies.* William T. Holmes and Mary C. Comerio. October 2003.

PEER 2003/11 *Fifth U.S.-Japan Workshop on Performance-Based Earthquake Engineering Methodology for Reinforced Concrete Building Structures.* February 2004.

PEER 2003/10 *A Beam-Column Joint Model for Simulating the Earthquake Response of Reinforced Concrete Frames.* Laura N. Lowes, Nilanjan Mitra, and Arash Altoontash. February 2004.

PEER 2003/09 *Sequencing Repairs after an Earthquake: An Economic Approach.* Marco Casari and Simon J. Wilkie. April 2004.

PEER 2003/08 *A Technical Framework for Probability-Based Demand and Capacity Factor Design (DCFD) Seismic Formats.* Fatemeh Jalayer and C. Allin Cornell. November 2003.

PEER 2003/07 *Uncertainty Specification and Propagation for Loss Estimation Using FOSM Methods.* Jack W. Baker and C. Allin Cornell. September 2003.

PEER 2003/06 *Performance of Circular Reinforced Concrete Bridge Columns under Bidirectional Earthquake Loading*. Mahmoud M. Hachem, Stephen A. Mahin, and Jack P. Moehle. February 2003.

PEER 2003/05 *Response Assessment for Building-Specific Loss Estimation.* Eduardo Miranda and Shahram Taghavi. September 2003.

PEER 2003/04 *Experimental Assessment of Columns with Short Lap Splices Subjected to Cyclic Loads*. Murat Melek, John W. Wallace, and Joel Conte. April 2003.

PEER 2003/03 *Probabilistic Response Assessment for Building-Specific Loss Estimation.* Eduardo Miranda and Hesameddin Aslani. September 2003.

PEER 2003/02 *Software Framework for Collaborative Development of Nonlinear Dynamic Analysis Program.* Jun Peng and Kincho H. Law. September 2003.

PEER 2003/01 *Shake Table Tests and Analytical Studies on the Gravity Load Collapse of Reinforced Concrete Frames.* Kenneth John Elwood and Jack P. Moehle. November 2003.

PEER 2002/24 *Performance of Beam to Column Bridge Joints Subjected to a Large Velocity Pulse.* Natalie Gibson, André Filiatrault, and Scott A. Ashford. April 2002.

PEER 2002/23 *Effects of Large Velocity Pulses on Reinforced Concrete Bridge Columns.* Greg L. Orozco and Scott A. Ashford. April 2002.

PEER 2002/22 *Characterization of Large Velocity Pulses for Laboratory Testing.* Kenneth E. Cox and Scott A. Ashford. April 2002.

PEER 2002/21 *Fourth U.S.-Japan Workshop on Performance-Based Earthquake Engineering Methodology for Reinforced Concrete Building Structures*. December 2002.

PEER 2002/20 *Barriers to Adoption and Implementation of PBEE Innovations.* Peter J. May. August 2002.

PEER 2002/19 *Economic-Engineered Integrated Models for Earthquakes: Socioeconomic Impacts.* Peter Gordon, James E. Moore II, and Harry W. Richardson. July 2002.

PEER 2002/18 *Assessment of Reinforced Concrete Building Exterior Joints with Substandard Details.* Chris P. Pantelides, Jon Hansen, Justin Nadauld, and Lawrence D. Reaveley. May 2002.

PEER 2002/17 *Structural Characterization and Seismic Response Analysis of a Highway Overcrossing Equipped with Elastomeric Bearings and Fluid Dampers: A Case Study.* Nicos Makris and Jian Zhang. November 2002.

PEER 2002/16 *Estimation of Uncertainty in Geotechnical Properties for Performance-Based Earthquake Engineering.* Allen L. Jones, Steven L. Kramer, and Pedro Arduino. December 2002.

PEER 2002/15 *Seismic Behavior of Bridge Columns Subjected to Various Loading Patterns.* Asadollah Esmaeily-Gh. and Yan Xiao. December 2002.

PEER 2002/14 *Inelastic Seismic Response of Extended Pile Shaft Supported Bridge Structures.* T.C. Hutchinson, R.W. Boulanger, Y.H. Chai, and I.M. Idriss. December 2002.

PEER 2002/13 *Probabilistic Models and Fragility Estimates for Bridge Components and Systems.* Paolo Gardoni, Armen Der Kiureghian, and Khalid M. Mosalam. June 2002.

PEER 2002/12 *Effects of Fault Dip and Slip Rake on Near-Source Ground Motions: Why Chi-Chi Was a Relatively Mild M7.6 Earthquake.* Brad T. Aagaard, John F. Hall, and Thomas H. Heaton. December 2002.

PEER 2002/11 *Analytical and Experimental Study of Fiber-Reinforced Strip Isolators*. James M. Kelly and Shakhzod M. Takhirov. September 2002.

PEER 2002/10 *Centrifuge Modeling of Settlement and Lateral Spreading with Comparisons to Numerical Analyses***.** Sivapalan Gajan and Bruce L. Kutter. January 2003.

PEER 2002/09 *Documentation and Analysis of Field Case Histories of Seismic Compression during the 1994 Northridge, California, Earthquake.* Jonathan P. Stewart, Patrick M. Smith, Daniel H. Whang, and Jonathan D. Bray. October 2002.

PEER 2002/08 *Component Testing, Stability Analysis and Characterization of Buckling-Restrained Unbonded Braces™.* Cameron Black, Nicos Makris, and Ian Aiken. September 2002.

PEER 2002/07 *Seismic Performance of Pile-Wharf Connections.* Charles W. Roeder, Robert Graff, Jennifer Soderstrom, and Jun Han Yoo. December 2001.

PEER 2002/06 *The Use of Benefit-Cost Analysis for Evaluation of Performance-Based Earthquake Engineering Decisions.* Richard O. Zerbe and Anthony Falit-Baiamonte. September 2001.

PEER 2002/05 *Guidelines, Specifications, and Seismic Performance Characterization of Nonstructural Building Components and Equipment*. André Filiatrault, Constantin Christopoulos, and Christopher Stearns. September 2001.

PEER 2002/04 *Consortium of Organizations for Strong-Motion Observation Systems and the Pacific Earthquake Engineering Research Center Lifelines Program: Invited Workshop on Archiving and Web Dissemination of Geotechnical Data, 4–5 October 2001*. September 2002.

PEER 2002/03 *Investigation of Sensitivity of Building Loss Estimates to Major Uncertain Variables for the Van Nuys Testbed.* Keith A. Porter, James L. Beck, and Rustem V. Shaikhutdinov. August 2002.

PEER 2002/02 *The Third U.S.-Japan Workshop on Performance-Based Earthquake Engineering Methodology for Reinforced Concrete Building Structures*. July 2002.

PEER 2002/01 *Nonstructural Loss Estimation: The UC Berkeley Case Study.* Mary C. Comerio and John C. Stallmeyer. December 2001.

PEER 2001/16 *Statistics of SDF-System Estimate of Roof Displacement for Pushover Analysis of Buildings.* Anil K. Chopra, Rakesh K. Goel, and Chatpan Chintanapakdee. December 2001.

PEER 2001/15 *Damage to Bridges during the 2001 Nisqually Earthquake.* R. Tyler Ranf, Marc O. Eberhard, and Michael P. Berry. November 2001.

PEER 2001/14 *Rocking Response of Equipment Anchored to a Base Foundation.* Nicos Makris and Cameron J. Black. September 2001.

PEER 2001/13 *Modeling Soil Liquefaction Hazards for Performance-Based Earthquake Engineering.* Steven L. Kramer and Ahmed-W. Elgamal. February 2001.

PEER 2001/12 *Development of Geotechnical Capabilities in OpenSees.* Boris Jeremi . September 2001.

PEER 2001/11 *Analytical and Experimental Study of Fiber-Reinforced Elastomeric Isolators*. James M. Kelly and Shakhzod M. Takhirov. September 2001.

PEER 2001/10 *Amplification Factors for Spectral Acceleration in Active Regions.* Jonathan P. Stewart, Andrew H. Liu, Yoojoong Choi, and Mehmet B. Baturay. December 2001.

PEER 2001/09 *Ground Motion Evaluation Procedures for Performance-Based Design.* Jonathan P. Stewart, Shyh-Jeng Chiou, Jonathan D. Bray, Robert W. Graves, Paul G. Somerville, and Norman A. Abrahamson. September 2001.

PEER 2001/08 *Experimental and Computational Evaluation of Reinforced Concrete Bridge Beam-Column Connections for Seismic Performance*. Clay J. Naito, Jack P. Moehle, and Khalid M. Mosalam. November 2001.

PEER 2001/07 *The Rocking Spectrum and the Shortcomings of Design Guidelines.* Nicos Makris and Dimitrios Konstantinidis. August 2001.

PEER 2001/06 *Development of an Electrical Substation Equipment Performance Database for Evaluation of Equipment Fragilities*. Thalia Agnanos. April 1999.

PEER 2001/05 *Stiffness Analysis of Fiber-Reinforced Elastomeric Isolators.* Hsiang-Chuan Tsai and James M. Kelly. May 2001.

PEER 2001/04 *Organizational and Societal Considerations for Performance-Based Earthquake Engineering.* Peter J. May. April 2001.

PEER 2001/03 *A Modal Pushover Analysis Procedure to Estimate Seismic Demands for Buildings: Theory and Preliminary Evaluation.* Anil K. Chopra and Rakesh K. Goel. January 2001.

PEER 2001/02 *Seismic Response Analysis of Highway Overcrossings Including Soil-Structure Interaction.* Jian Zhang and Nicos Makris. March 2001.

PEER 2001/01 *Experimental Study of Large Seismic Steel Beam-to-Column Connections.* Egor P. Popov and Shakhzod M. Takhirov. November 2000.

PEER 2000/10 *The Second U.S.-Japan Workshop on Performance-Based Earthquake Engineering Methodology for Reinforced Concrete Building Structures.* March 2000.

PEER 2000/09 *Structural Engineering Reconnaissance of the August 17, 1999 Earthquake: Kocaeli (Izmit), Turkey.* Halil Sezen, Kenneth J. Elwood, Andrew S. Whittaker, Khalid Mosalam, John J. Wallace, and John F. Stanton. December 2000.

PEER 2000/08 *Behavior of Reinforced Concrete Bridge Columns Having Varying Aspect Ratios and Varying Lengths of Confinement.* Anthony J. Calderone, Dawn E. Lehman, and Jack P. Moehle. January 2001.

PEER 2000/07 *Cover-Plate and Flange-Plate Reinforced Steel Moment-Resisting Connections.* Taejin Kim, Andrew S. Whittaker, Amir S. Gilani, Vitelmo V. Bertero, and Shakhzod M. Takhirov. September 2000.

PEER 2000/06 *Seismic Evaluation and Analysis of 230-kV Disconnect Switches.* Amir S. J. Gilani, Andrew S. Whittaker, Gregory L. Fenves, Chun-Hao Chen, Henry Ho, and Eric Fujisaki. July 2000.

PEER 2000/05 *Performance-Based Evaluation of Exterior Reinforced Concrete Building Joints for Seismic Excitation.* Chandra Clyde, Chris P. Pantelides, and Lawrence D. Reaveley. July 2000.

PEER 2000/04 *An Evaluation of Seismic Energy Demand: An Attenuation Approach.* Chung-Che Chou and Chia-Ming Uang. July 1999.

PEER 2000/03 *Framing Earthquake Retrofitting Decisions: The Case of Hillside Homes in Los Angeles.* Detlof von Winterfeldt, Nels Roselund, and Alicia Kitsuse. March 2000.

PEER 2000/02 *U.S.-Japan Workshop on the Effects of Near-Field Earthquake Shaking.* Andrew Whittaker, ed. July 2000.

PEER 2000/01 *Further Studies on Seismic Interaction in Interconnected Electrical Substation Equipment.* Armen Der Kiureghian, Kee-Jeung Hong, and Jerome L. Sackman. November 1999.

PEER 1999/14 *Seismic Evaluation and Retrofit of 230-kV Porcelain Transformer Bushings*. Amir S. Gilani, Andrew S. Whittaker, Gregory L. Fenves, and Eric Fujisaki. December 1999.

PEER 1999/13 *Building Vulnerability Studies: Modeling and Evaluation of Tilt-up and Steel Reinforced Concrete Buildings.* John W. Wallace, Jonathan P. Stewart, and Andrew S. Whittaker, editors. December 1999.

PEER 1999/12 *Rehabilitation of Nonductile RC Frame Building Using Encasement Plates and Energy-Dissipating Devices.* Mehrdad Sasani, Vitelmo V. Bertero, James C. Anderson. December 1999.

PEER 1999/11 *Performance Evaluation Database for Concrete Bridge Components and Systems under Simulated Seismic Loads.* Yael D. Hose and Frieder Seible. November 1999.

PEER 1999/10 *U.S.-Japan Workshop on Performance-Based Earthquake Engineering Methodology for Reinforced Concrete Building Structures.* December 1999.

PEER 1999/09 *Performance Improvement of Long Period Building Structures Subjected to Severe Pulse-Type Ground Motions*. James C. Anderson, Vitelmo V. Bertero, and Raul Bertero. October 1999.

PEER 1999/08 *Envelopes for Seismic Response Vectors.* Charles Menun and Armen Der Kiureghian. July 1999.

PEER 1999/07 *Documentation of Strengths and Weaknesses of Current Computer Analysis Methods for Seismic Performance of Reinforced Concrete Members.* William F. Cofer. November 1999.

PEER 1999/06 *Rocking Response and Overturning of Anchored Equipment under Seismic Excitations.* Nicos Makris and Jian Zhang. November 1999.

PEER 1999/05 *Seismic Evaluation of 550 kV Porcelain Transformer Bushings.* Amir S. Gilani, Andrew S. Whittaker, Gregory L. Fenves, and Eric Fujisaki. October 1999.

PEER 1999/04 *Adoption and Enforcement of Earthquake Risk-Reduction Measures.* Peter J. May, Raymond J. Burby, T. Jens Feeley, and Robert Wood.

PEER 1999/03 *Task 3 Characterization of Site Response General Site Categories*. Adrian Rodriguez-Marek, Jonathan D. Bray, and Norman Abrahamson. February 1999.

PEER 1999/02 *Capacity-Demand-Diagram Methods for Estimating Seismic Deformation of Inelastic Structures: SDF Systems*. Anil K. Chopra and Rakesh Goel. April 1999.

PEER 1999/01 *Interaction in Interconnected Electrical Substation Equipment Subjected to Earthquake Ground Motions.* Armen Der Kiureghian, Jerome L. Sackman, and Kee-Jeung Hong. February 1999.

PEER 1998/08 *Behavior and Failure Analysis of a Multiple-Frame Highway Bridge in the 1994 Northridge Earthquake.* Gregory L. Fenves and Michael Ellery. December 1998.

PEER 1998/07 *Empirical Evaluation of Inertial Soil-Structure Interaction Effects.* Jonathan P. Stewart, Raymond B. Seed, and Gregory L. Fenves. November 1998.

PEER 1998/06 *Effect of Damping Mechanisms on the Response of Seismic Isolated Structures.* Nicos Makris and Shih-Po Chang. November 1998.

PEER 1998/05 *Rocking Response and Overturning of Equipment under Horizontal Pulse-Type Motions.* Nicos Makris and Yiannis Roussos. October 1998.

PEER 1998/04 *Pacific Earthquake Engineering Research Invitational Workshop Proceedings, May 14–15, 1998: Defining the Links between Planning, Policy Analysis, Economics and Earthquake Engineering.* Mary Comerio and Peter Gordon. September 1998.

PEER 1998/03 *Repair/Upgrade Procedures for Welded Beam to Column Connections.* James C. Anderson and Xiaojing Duan. May 1998.

PEER 1998/02 *Seismic Evaluation of 196 kV Porcelain Transformer Bushings.* Amir S. Gilani, Juan W. Chavez, Gregory L. Fenves, and Andrew S. Whittaker. May 1998.

PEER 1998/01 *Seismic Performance of Well-Confined Concrete Bridge Columns.* Dawn E. Lehman and Jack P. Moehle. December 2000.

ONLINE REPORTS

The following PEER reports are available by Internet only at http://peer.berkeley.edu/publications/peer_reports.html

PEER 2009/106 *Shear Strength Models of Exterior Beam-Column Joints without Transverse Reinforcement.* Sangjoon Park and Khalid M. Mosalam. November 2009.

PEER 2009/105 *Reduced Uncertainty of Ground Motion Prediction Equations through Bayesian Variance Analysis.* Robb Eric S. Moss. November 2009.

PEER 2009/104 *Advanced Implementation of Hybrid Simulation.* Andreas H. Schellenberg, Stephen A. Mahin, Gregory L. Fenves. November 2009.

PEER 2009/103 *Performance Evaluation of Innovative Steel Braced Frames.* T. Y. Yang, Jack P. Moehle, and Božidar Stojadinović. August 2009.

PEER 2009/102 *Reinvestigation of Liquefaction and Nonliquefaction Case Histories from the 1976 Tangshan Earthquake.* Robb Eric Moss, Robert E. Kayen, Liyuan Tong, Songyu Liu, Guojun Cai, and Jiaer Wu. August 2009.

PEER 2009/101 *Report of the First Joint Planning Meeting for the Second Phase of NEES/E-Defense Collaborative Research on Earthquake Engineering.* Stephen A. Mahin et al. July 2009.

PEER 2008/104 *Experimental and Analytical Study of the Seismic Performance of Retaining Structures.* Linda Al Atik and Nicholas Sitar. January 2009.

PEER 2008/103 *Experimental and Computational Evaluation of Current and Innovative In-Span Hinge Details in Reinforced Concrete Box-Girder Bridges. Part 1: Experimental Findings and Pre-Test Analysis.* Matias A. Hube and Khalid M. Mosalam. January 2009.

PEER 2008/102 *Modeling of Unreinforced Masonry Infill Walls Considering In-Plane and Out-of-Plane Interaction.* Stephen Kadysiewski and Khalid M. Mosalam. January 2009.

PEER 2008/101 *Seismic Performance Objectives for Tall Buildings.* William T. Holmes, Charles Kircher, William Petak, and Nabih Youssef. August 2008.

PEER 2007/101 *Generalized Hybrid Simulation Framework for Structural Systems Subjected to Seismic Loading.* Tarek Elkhoraibi and Khalid M. Mosalam. July 2007.

PEER 2007/100 *Seismic Evaluation of Reinforced Concrete Buildings Including Effects of Masonry Infill Walls.* Alidad Hashemi and Khalid M. Mosalam. July 2007.